Republic of Iraq
Ministry of Higher Education
and Scientific Research
University of Babylon
College of Science
Department of Physics

Study the Effect of RF Magnetized Plasma on the Structural and Magnetic Properties of Spinel Ferrite

A Thesis
Submitted to the Council of the College of Science University of Babylon in Partial Fulfilment of the Requirements for the Degree of Doctorate of Philosophy in Science Physics

By

Alyaa Hefdhi Abbas Aziz

B.Sc. University of Babylon /2004
M.Sc. University of Babylon / 2017

Supervised by

Prof.Dr.	**Prof.Dr.**
Mohammed Abdul Ammer AL-Shareefi	**Abdulhussain Abbas Khadyair**

2023 A.D. **1445 A.H.**

جمهورية العراق

وزارة التعليم العالي والبحث العلمي

جامعة بابل

كلية العلوم- قسم الفيزياء

دراسة تأثير بلازما الترددات الراديوية الممغنطة على الخصائص التركيبية والمغناطيسية لسبينل فرايت

أطروحة

مقدمة الى مجلس كلية العلوم- جامعة بابل

وهي جزء من متطلبات نيل درجة الدكتوراه فلسفة في العلوم الفيزياء

من قبل

علياء حفظي عباس عزيز

بكالوريوس جامعة بابل/ ٢٠٠٤

ماجستير جامعة بابل/ ٢٠١٧

بإشراف

أ.د. محمد عبد الامير الشريفي　　　　أ.د. عبد الحسين عباس خضير

٢٠٢٣م　　　　١٤٤٥هـ

بسم الله الرحمن الرحيم

(قَالوا سُبحانَك لا عِلْمَ لَنا إِلاَّ ما عَلَّمْتَنا إِنَّكَ أَنتَ
العَلِيمُ الْحَكِيمِ)

صدق الله العظيم

سورة البقرة الآية (٣٢)

Dedication

To my reason for being . . . . . . my parents

To those whom I most cherish and who comfort

my soul ...... my brothers

To my companion and my support ......my husband

To the candles that illuminated my life .....my children

To those who have been of great help to me......my
colleagues at work

To those who wish me well, I dedicate the fruit of ....my
humble effort

Alyaa

Acknowledgement

Praise be to God. Who gives me ((Faith, Patience and courage)) along to complete this work. I would like to express my deep appreciation to Respected supervisors, Dr. Muhammad Abd al-Amir al-Shareefi and Dr. Abd al-Hussein Abbas for proposing of this Work, valuable guidance, and constant encouragement in development of this work.

I would like to express my gratitude and thanks to the Deanship of the College of Science and the Department of Physics, especially Prof. Dr. Abdelaziz Al-Ogaili*, Prof. Dr. Raheem G. Kadhim Al-Morshdy and Dr. Samira A. Mahdi, Head of the Physics Department, for their care and great support for me in order to accomplish this research. I cannot fail to express my gratitude to Dr. Faris Al-Kufi, a professor at the University of Kufa, for his assistance to me, wishing him continued success.*

Finally, I would like to express my deepest thanks and appreciation to those who helped me and did not mention it.

Alyaa

Summary

In this study, two compounds of ferrite spinel (magnesium ferrite) are synthesized by the sol-gel spontaneous combustion technique, then we vaccination them with divalent elements (cadmium and copper), and for ratios x = (0, 0.2, 0.4, 0.6, 0.8, and 1) to form the formulas $\mathbf{Cd_{1-X}Mg_X\,Fe_2O_4}$, $\mathbf{Cu_{1-X}Mg_X\,Fe_2O_4}$.

The structural properties of the prepared compounds are investigated using X-ray diffraction technique, where the synthetic tests showed that the pure spinel phase for all samples is achieved by the X-ray diffraction. The patterns of the samples confirmed the formation of the spinel structure without any secondary phases or impurities. It is found that both the crystal size and lattice constant of magnesium-cadmium ferrite (27-32) nm, ((0.873-0.863) nm, respectively and magnesium ferrite and copper (30-32) nm, (0.822- 0.875) nm. Field emission scanning electron microscope (FESEM) is used to investigate the surface morphology and there are some clusters in the electron microscopy images, almost as dense and with less pores.

The Fourier transform infrared spectroscopy(FTIR) measurements show two main bands for the positions of the atoms in the tetrahedral sites (A) and the octahedral sites (B) in the crystal structure, and of the appearance of the peaks of the prepared compound , the range from (432-575) cm^{-1}, which is evidence of the formation of bands between the mineral present in the crystalline structure and the oxygen ion. The magnetic properties of all prepared samples by the magnetic vibration device (VSM) were also studied, and it was confirmed through magnetic hysteresis ring drawings to obtain a soft ferrous material with a narrow hysteresis ring and magnetic coefficients that were found for all compounds.

After that, the two prepare compounds are exposed to the same concentrations to plasma using a radio frequency (RF) magnetron spray, and the temperature and energy parameters were considered constant for all samples. X-ray measurements showed that the samples exposed to plasma had the cubic spinel structure as they had before exposure and that the crystal size decreases after exposure to plasma with increasing concentrations of magnesium used with a decrease in the intensity of the peak formed. As for the results of FESEM analysis after exposure, of the compound $Cd_{1-X}Mg_X Fe_2O_4$ to plasma and with an increase in the amount of Mg concentrations, we notice a change in the surface topography and roughness in the surface, also for ferrite $Cu_{1-X}MgxFe_2O_4$ after exposure to plasma, we notice change in the shape and size of the grain . Measurements VSM of $Cd_{1-X}MgxFe_2O_4$ show an increase in saturation magnetization after plasma exposure. It is clear to the compound $Cu_{1-X}Mg_xFe_2O_4$ that exposure to plasma led to an increase of M_s, H_c and M_r for the exposed samples.

The prepared materials can be good magnets, gas sensors, or used in the core of electrical transformers to reduce eddy currents. Exposing the prepared samples to plasma results in the deposition of a layer of plasma on the surface of the samples. This plasma is similar to that used in plasma engraving, deposition, and surface treatment of materials that protect them from corrosion.

الخلاصة

في هذه الدراسة، تم تحضير مركبين من الإسبينل الفرايت (المغنيسيوم فرايت) بواسطة تقنية الاحتراق التلقائي (سول- جل)، ثم قمنا بتطعيمهما بعناصر ثنائية التكافؤ (الكادميوم والنحاس)، وللنسب x =(0 ، 0.2، 0.4، 0.6، 0.8و 1) للحصول على الصيغ التالية ($Cd_{1-X}Mg_X Fe_2O_4$) ، ($Cu_{1-X}Mg_X Fe_2O_4$).

تم دراسة الخصائص التركيبية للمركبات المحضرة باستخدام تقنية حيود الأشعة السينية، حيث أظهرت اختبارات البنية التركيبية أن طور الإسبينل هو نقي لجميع العينات تم تحقيقه عن طريق حيود XRD وإيجاد الحجم البلوري وثابت الشبكية لكل مركب باستخدام معادلة شيرر .وجد أن كلا من الحجم البلوري والثابت الشبكي للمغنيسيوم والكادميوم فرايت nm(27-32)، (0.873-0.863)nmوحديدي المغنيسيوم والنحاس, nm (32-30) ,(0.875-0.822)nm على التوالي. تم استخدام المجهر الإلكتروني لمسح الانبعاث الميداني (FESEM) لدراسة مورفولوجيا السطح وتجانس عينات المسحوق، وكانت هناك بعض المجموعات في صور المجهر الإلكتروني تقريبًا كثيفة وذات مسام أقل.

تظهر قياسات التحليل الطيفي للأشعة تحت الحمراء لتحويل فورييه FTIR طيفي امتصاص رئيسيين لمواقع الذرات في مواقع التتراهدرا(A) ومواقع الاوكتاهدرا (B) في التركيب البلوري، وهذا ما أكدته رسومات FTIR لظهور قمم المركبات المحضرة يتراوح مداها بين (432-575) cm^{-1}، وهو دليل على تكوين اواصر بين المعدن الموجود في التركيب البلوري وأيون الأوكسجين ، وعلى هذا الأساس يحدد نوع الفرايت.

كما تمت دراسة الخواص المغناطيسية لجميع العينات التي تم تحضيرها بواسطة جهاز الاهتزاز المغناطيسي (VSM)، والحصول على مادة حديدية لينة ذات حلقة هسترة ضيقة ودراسة معاملات المغناطيسية لجميع المركبات.

بعد ذلك، تم تعريض المركبين المحضرين لنفس التركيز الى بلازما الترددات الراديوية (RF)، واعتبرت معاملات درجة الحرارة والطاقة ثابتة لجميع العينات. تشبه هذه البلازما تلك المستخدمة في الترسيب والمعالجة. أظهرت قياسات الأشعة السينية أن العينات المعرضة للبلازما لها هيكل السبينل المكعب كما كانت قبل التعرض وأن حجم البلورة يتناقص بعد التعرض

للبلازما بتراكيز متزايدة من المغنيسيوم حسب النسب المستخدمة مع انخفاض شدة الذروة المتكونة. بالنسبة لنتائج تحليل FESEM بعد التعرض، المركب $Cd_{1-X}Mg_X Fe_2O_4$ ومع زيادة تركيز Mg ، نلاحظ تغيرًا في تضاريس السطح وخشونة في السطح ، كذلك في حالة الفرايت $Cu_{1-X}Mg_X$ Fe_2O_4، بعد التعرض للبلازما، نلاحظ تغيرًا في شكل وحجم البلورة وأصبحت غير متجانسة لأنها لم تعد كروية كما كانت قبل التعرض.

تُظهر قياسات VSM لـ $Cd_{1-X}Mg_xFe_2O_4$ زيادة في مغنطة التشبع بعد التعرض للبلازما, من الواضح للمركب $Cu_{1-X}MgxFe_2O_4$ أن التعرض للبلازما أدى إلى زيادة M_s و H_c و M_r للعينات المفحوصة.

أن المواد المحضرة يمكن أن تكون مغناطيسات جيدة ، أو حساسات غاز ، أو تستخدم في قلب المحولات الكهربائية للتقليل من التيارات الدوامة. ينتج عن تعريض العينات المحضرة للبلازما ترسب طبقة من البلازما على سطح العينات, هذه البلازما تشبه تلك المستخدمة في نقش البلازما والترسيب ومعالجة السطحية للمواد التي تحميها من التآكل.

CONTENTS

Chapter One: Introduction

Chapter Two: Theoretical Background

Chapter Three: Methodology and Instruments

Chapter Five :Conclusions and Suggestions

List of Figures

List of Tables

List of Important Symbols

Symbol	Description	Unit
$\overrightarrow{B}$	Magnetic flux density	Wb/m^2 or Tesla
$\overrightarrow{H}$	Magnetic field intensity	A/m or Oe
μ	Permeability	H/m
μ_0	Vacuum permeability	----
μ_r	Relative permeability	----
μ_r'	Real part of relative permeability	----
μ_r''	Imaginary part of relative permeability	----
M	Magnetism distribution	emu / g
χ	Magnetic susceptibility	---
T	Temperature	K
T_c	Curie temperature	C^O
T_e	Temperature of electron	K
T_i	Temperature of ion	K
T_g	Temperature of gas	K
C	Curie constant	----
we	Frequency of the electron	Rad/s
w_p	Frequency of the plasma	Rad/s
δ	Angle of loss in the material	---
M_s	Saturation Magnetization	emu/g
M_r	Remaining magnetization	emu/g

Symbol	Description	Unit
B_s	Saturation magnetic flux	----
Br	Remaining magnetic flux	----
$\overrightarrow{H}_c$	Coercive force	O_e
m	Positive integer that represents the diffraction order	----
λ	Wavelength	Å, nm
d_{hkl}	Interlayer distance for crystalline surfaces	nm
θ	Bragg diffraction angle	Degree
hkl	Miller indices	---
a	Lattice constant	Å
D	Crystallite size	nm, µm
β	The FWHM (full width at half maxima) of the peak at angle θ	radian
θ_β	Bragg diffraction angle of the XRD peak.	degree
S	Erosions	nm^{-2}
n_i	The density of ionized atoms	number per m^3
n_n	The density of neutral atoms	number per m^3
K	Boltzmann's constant =	Ev/k
Ui	Ionization energy	eV
g_i	The degeneracy of states for the *i*-ions	-----

Symbol	**Description**	**Unit**
ϵ_i	The energy required to remove *i* electrons	eV
m_e	The mass of an electron	g
h	The Planck's constant	Joule. s
n	Number of moles	----
W	Weight to be calculated	g
W_m	Molecular weight	g/mol

List of Abbreviations

Definition	**Attribute**
Face Center Cubic	FCC
Contact Non-Equilibrium Plasma	CNP
Radio Frequency	RF
The Divalent Metal	M
Body Center Cubic	BCC
Full Width at Half Maximum	FWHM
Fourier Transform Infrared Spectroscopy	FTIR
Scanning Electron Microscope	SEM
Field Emission Scanning Electron Microscopy	FE-SEM
X-Ray Diffraction	XRD
Hydrogen Number	pH
Vibrating Sample Magnetometer	VSM
Direct Current	D.C
Alternate Current	A.C
Inductively Coupled Discharge	ICD
Capacitive Coupled Discharge	CCD
Low Radioactivity Techniques	LRT
Count Per Second	CPS
Magnetic Resonance Imaging	MRI
International Centre for Diffraction Data	ICDD

Chapter One

Introduction

Chapter Two

Theoretical Part

Chapter Three

Methodology and Instruments

Chapter Four

Results and Discussion

Chapter Five

Conclusions and Suggestions

References

Chapter One
Introduction

1.1 Introduction

Due to high coercively, high mechanical properties, moderate saturation magnetization, high electrical resistance and chemical stability ferrite has been applied in many fields, such as high-frequency transformers, magnetic storage equipment, electromagnetic shielding the polycrystalline ferrite has received special attention due to its have magnetic properties. There are two main types of magnetic materials, the first one is metal and the second is metal oxides. Mineral oxide materials are called ferrite [1]. A ferrite is a type of ceramic compound of iron oxide (Fe_2O_3) combined chemically with one or more additional metallic elements. Spinel-type ferrite is commonly used in many electronic and magnetic devices consequent to its high magnetic permeability and low magnetic loss, meaning they can be magnetized or attracted to a magnet, and are electrically nonconductive [2].

Ferrite is chemical compounds (ferromagnetic materials) that are not conducive to electrically and that contain oxygen and at least two magnetic ions that contain the chemical formula (AB_2O_4) which is designated as a cubic closed-packing of O^{-2} ions [2]. A great variety in the chemical composition of spinel ferrites is possible. The diversity in composition results into a large range of physical properties that permits the tuning of the properties for specific applications and makes spinel ferrites of particular interest. The ferrite spinel has a face-centered cubic (FCC) structure ,which consists of a cubic close-packed oxygen lattice [3].

Over the past several years, ferrites spinels AFe_2O_4, where A is a divalent transition metal (Ni, Zn, Fe, Cr, Mn, Co) have attracted great interest due to their good biocompatibility, low toxicity and their magnetism. The structure of spinel, the magnetic ions are distributed among different two lattice site, tetrahedral(A) and octahedral(B) sites. The substitution can be divided into the following types: direct replacement of Fe^{+3} on tetrahedral (A) or octahedral (B) sub lattice by the substituent ion, and consequential redistribution of Fe^{+3} ions between A- and B- sub lattices which lead to the change of ferromagnetic spin structure[4].

The iron redistribution of extent depends on the specific nature of the substituting ion. The properties of ferrite electromagnetic depend on the proportional distribution of cations at the different sites and the preparation condition. Ferrites are highly sensitive to preparation method, amount of constituent metal oxides sintering condition and the dopants or substituted elements. The magnetic properties and structural of ferrites will be found to be sensitive to their composition and microstructure, which depends upon the processing conditions. Several types of synthesis methods have been developed to prepare pure and doped ferrite materials, such as, sol–gel, auto-combustion , hydrothermal, etc methods [5].

To obtain beneficial products spinel ferrites of different compositions have been studied and used, each ferrite has advantage and disadvantages, for improving their electrical and magnetic properties many researchers have worked on different types of ferrites. Among the different synthesis methods, sol-gel technique will been widely used to prepare ferrite materials and exposing them to plasma rays and showing the effect of the rays on the prepared models. The plasma exists in many forms in nature and has a widespread use in science and technology. It is a special kind of ionized gas and in general consists of:

– positively charged ions (‘positive ions’)

– electrons

– neutrals (atoms, molecules).

Under special conditions, plasma may also contain negative ions. ‘plasma’ if it is quasi-neutral and its properties are dominated by electric and or magnetic forces. Owing to the presence of free ions, using plasma for ion sources is quite natural [6]. Plasma is produced by a suitable form of low-pressure gas discharge. The resulting plasma is usually characterized as ‘cold plasma’, though the electrons may have temperatures of several tens of thousands of Kelvins (i.e. much hotter than the surface of the sun), while ions and the neutral gas are more or less warm [7].

However, owing to their extremely low mass, electrons cannot transfer much of their thermal energy as heat to the heavier plasma components or to the enclosing walls. Thus this type of cold plasma does not transfer much heat to its environment and it may be more exactly characterized as ‘low-enthalpy plasma [7].

1.2 Previous Studies

Spinel ferrites are extremely important for technological application, the physical properties such as structural and magnetic properties are governed by the type of magnetic ions residing on the tetrahedral A-site and octahedral

B-site of the spinel lattice and the relative strength of the intra- sub lattice interactions.

In (2010) Pengzhao Gao ***et al.,*** [8] Nanocrystal $Ni_{0.5}Zn_{0.5}Fe_2O_4$ thin films was synthesized with various grain sizes by a sol-gel method on polycrystalline silicon substrates. The morphology, magnetic, and microwave absorption properties of the films calcined were studied with x-ray diffraction, vibrating sample magnetometry. Increasing the calcination temperature from(873) to (1073) K^o and time from (1) to (3) h resulted in an increase of the grain size. The saturation and remnant magnetization increased with increasing the grain size, while the coercivity demonstrated a maximum near a grain size. The highest microwave heating rate in the temperature was observed in the film close to the grain size.

In (2010) Dangwei Guo ***et al***., [9] Ni Zn ferrite films with well-defined spinel crystal structure was in situ fabricated by radio frequency magnetron sputtering at room temperature. The microstructures and static magnetic properties of the films' dependence on the partial pressure ratio of argon to oxygen gas. Scanning electron microscope images indicated that all the films consisted of particles monocrystalline and the sizes increase as the ratio increases in the range of (10–25) nm. A large saturation magnetization (237.2)emu/cm^3 and a minimum of coercivity (68) Oe.

In (2011) Ashok Nawale ***et al***., [10] Studying have been for magnetic nanoparticles of nickel ferrite involving thermal plasma assisted vapor phase condensation process. The as-synthesized samples were characterized by X-ray diffraction. The effects of reactor parameters on the magnetic and structural properties have been evaluated, to find the optimized parameters so as to achieve the highest values of saturation magnetization and coercivity. Reasonably high saturation magnetization (48) emu/g has been assigned to the high degree of crystallinity, achieved on account of high temperature during the growth and the cation redistribution. The high value of coercivity (115) Oe is explained on the basis of possible lattice defects arising from the cation redistribution. Detailed analysis of cation distribution using the XRD line intensity data leads to the conclusion that these samples are iron deficit and nickel rich.

In (2011) Yingli Liua ***et al***.,[11] Polycrystalline NiZn–ferrite thin films were deposited on Si substrate by Rf magnetron sputtering, using targets with a nominal composition of $Ni_{0.5}Zn_{0.5}Fe_2O_4$. The effects of substrate condition, sputtering pressure and post annealing on the structure and magnetic properties of thin films have been investigated. Our results show that the preferred orientation of the NiZn spinel film changed from (311) to (400) with increasing the Ar pressure from (0.8) to (1.6) Pa, meanwhile, the grain size also increased. A thin film with a typical thickness of (1) μm, a saturation magnetization of (150) emu/cm^3 and a coercivity of (8.8) kA/m has been obtained after annealing at (800) °C, which has the potential application in magnetic integrated circuits.

In (2012) Ilmars Zalite ***et al*.,** [12] The $NiFe_2O_4$ and $CoFe_2O_4$ ferrites were synthesized using two methods chemical sol-gel self-combustion and high frequency plasma chemical synthesis. Magnetic properties, crystallite size and specific surface area of the synthesized ferrites were measured. The average particle size of powders obtained by the sol-gel self combustion method is (25 -40)nm, whereas ferrites synthesized in plasma have in the range (10-100) nm, with some particles as large as (200) nm. These samples' magnetic saturation values are very close to those of the standard bulk material (80) emu/g for $CoFe_2O_4$ and (50) emu/g for $NiFe_2O_4$. However, the magnetic properties of the sol-gel self-combustion samples differ from those of the plasma products; this is most likely due to crystallite size.

In (2012) Noppakun Sanpo ***et al.,*** [13] Zinc-substituted cobalt ferrite nanopowders were prepared via a sol-gel route using citric acid as a chelating agent. The influence of zinc concentration on the microstructure, surface wettability, crystal structure, surface roughness, cobalt ferrite nanopowders was formed a cubic spinel structure and exhibited irregular morphology with a crystallite size in the range of (40–50) nm. Increasing the concentration of zinc substitution has no significant effect on the surface roughness. The substitution of zinc influences slightly the microstructure, surface wettability, surface roughness.

In (2013) Alin C. Druc ***et al.,*** [14] Substituted magnesium ferrite ultrafine powders were prepared for the first time with copper, with the general formula $Mg_{1-x}Cu_xFe_2O_4$ (x = 0.00, 0.17, 0.34, 0.50, 0.67, 0.84 and 1.00) by sol-gel method with spontaneous combustion using glycine as a combustion agent. The chemical reaction in the solid phase and the appearance of the spinel type structure were monitored by infrared absorption spectroscopy. This is confirmed by X-ray diffraction .The formation of the unique cubic spinel phase. The microstructure of the samples was analyzed by electron microscopy.

In (2013) S. Kanagesan ***et al.,*** [15] Nano crystalline magnesium ferrites ($MgFe_2O_4$) were produced with an average grain size of about (20) nm. Their structural and magnetic characterizations were studied $MgFe_2O_4$ nanoparticles were successfully synthesized by the micro emulsion technique. XRD analysis reveals that the synthesized samples have a single cubic spinel phase without trace of any impurity. The size of the $MgFe_2O_4$ powder. The FTIR pattern confirms the characteristic peaks of ferrite system. The hysteresis loop was exhibits ferromagnetic behavior.

In (2014) Najmeh Najmoddina, ***et al.,*** [16] This study dealt with the effect of doping with zinc ion on the magnetic properties of $CuFe_2O_4$ with ratios(x=0.0, 0.25, 0.5 and 0.75). The distribution of cations between tetrahedral (A) was calculated and octahedral (B) lattice positions analytically by X-ray diffraction (XRD). Samples that crystallized were found to have a lattice constant a where they range from (6.5) to (8.3) nm. The magnetization curves of $Cu_{0.75}Zn_{0.25}Fe_2O_4$ revealed the existence of a super magnetic phase at room temperature. The value of saturation magnetism was recorded between (15) and (300) kOe.

In (2015) Praveena ***et al.,*** [17] Researched the composition and magnetic properties of Mn-Zn ferrite using the microwave a hydrothermal method for high-frequency applications with the ratio of (x= 0, 0.2, 0.4, 0.6, 0.8 and 1.0). They succeeded in preparing the nanostructures using the microwave at (900) ºC for a total time of (30) minutes. From XRD analysis it is found that all the samples possess single phase without any impurity phase. From SEM investigation, it is observed that the grain size varies in between (54)nm to(75)nm. The saturation magnetization (MS) increases with an addition of Zn(x) content to Mn-Zn ferrites up to (x=0.4).

In(2015) H. Le Trong ***et al.***, [18] Iron cobaltite thin films $Co_{1.75}Fe_{1.25}O_4$ with spinel structure have been elaborated by radio-frequency (RF) magnetron sputtering from. Influence of argon pressure on structure, microstructure and physical properties of films has been examined. XRD revealed the formation of spinel structure with space Iron–cobalt oxide thin films essentially consist of one spinel phase. The increase in argon pressure also leads to the lowering of both saturation magnetization, coercive field when the magnetic hysteresis curve of the sample is measured after field cooling from room temperature to (150) K or below.

In(2016) Hassen Harzalia ***et al***., [19] Assisted co-precipitation method was used to prepare the Ni Cu Zn ferrites. The structure and magnetic properties have been investigated results obtained a single-phase Ni-Cu-Zn ferrite with cubic spinel structure. The crystallite size of synthesized nanocrystals was calculated using Debye-Scherer. The range of crystallite size lied between (10) and (25)nm. The saturation of magnetization (Ms) increases with increasing the crystallite size. The optimal value of (Ms) was obtained for the sample synthesized power (46)Watt.

In (2016) M.Penchal Reddy ***et al***., [20] Spark plasma sintering (SPS) technique has been employed to obtain phase pure. It was undertaken the effect of sintering temperature on the densification, microstructures and magnetic properties of magnesium ferrite ($MgFe_2O_4$) crystalline and Mg ferrites at (900) ^{0}C. Analysis of XRD spectra reveals the formation of single phase spinel cubic structure. The crystallinity, particle size and the magnetic saturation(Ms) increase with an increase in sintering temperature. The improvement in magnetic properties can be attributed to increases in density. Owing to its lower sintering temperature and significantly shorter heating time which lead to more regular size and stronger magnetization.

In (2017) K. Kombaiah ***et al***., [21] Studied the structural and magnetic properties of $ZnFe_2O_4$ nanoparticles prepared with $Cd^{+\ 2}$ doping. They succeeded in preparing the nanoparticles by microwave combustion. Their study showed that the crystallinity and size change of the nanoparticles decreased from (42) nm to (12) nm with increasing dopant concentration. The lattice parameter of the spinel structure increases when the nanoparticle size decreases. FTIR spectra confirmed the presence of metal oxides absorption bands in the low and high frequency regimes. SEM images showed the presence of spherical particles in the nanoscale system. Magnetic scans revealed an increase in saturation magnetization and an increase in coercivity with increasing concentration of $Cd^{+\ 2}$ ions.

In (2017) Frolova and Derhachov [22] Nano-sized manganese ferrites $MnxFe_{3-x}O_4$ (x=0-1.3) were prepared using contact non-equilibrium plasma (CNP). Magnetic properties were investigated employing X-ray (XRD), Fourier transform infrared (FTIR), scanning electron microscopy (SEM) and magnetic measurement techniques. The formation of monodispersed faceted ferrite particles and the FTIR spectra revealed reflection in region (1200–1700) cm^{-1} caused by the presence of water adsorbed on the surface of $Fe_{3-x}Mn_xO_4$ micro-granules. The XRD results showed that the nanocrystal line $MnxFe_{3-x}O_4$ $(0 < x < 1.0)$ had cubic spinel crystal structure with average crystallite size (48–49) nm.

In (2018) Thorata ***et al*.,**[23] We report the synthesis of Co^{+2} substituted Mg–Cu–Zn ferrite via citrate gel combustion process and thereby its structural and magnetic properties for the use in electromagnetic energy absorption application. The polycrystalline ferrite system was investigated by interplay of stoichiometric composition with $Mg_{0.25-x}Co_xCu_{0.25}Zn_{0.5}Fe_2O_4$ ($0 \leq x \leq 0.25$). Structural investigations using X-ray diffraction(XRD). The average grain size was determined enhancement in the grain size is observed with the addition of Co^{+2} to Mg^{+2} ions in $Mg_{0.25-x}Co_xCu_{0.25}Zn_{0.5}Fe_2O_4$ samples. The micrographs of Co^{+2} doped ferrite samples show the formation of distinct grains.

In (2018) Jinpei Lin ***et al.,*** [24] The present study is the preparation of chromium substituted nickel ferrite $N_iCr_xFe_{2-x}O_4$ (x = 0-1.0) powders by a sol-gel auto-combustion method. X-ray diffraction analysis (XRD) showed that the specimens with x > 0.2 exhibited a single-phase spinel structure and that more content of Cr within a specimen is favorable for the synthesis of pure Ni-Cr ferrites. Scanning Electron Microscopy (SEM) showed the formation of ferrite powders nano-particles and that the substitution of Cr weakened the agglomeration between the particles. The saturation magnetization decreased by the Cr^{+3} ions and reached a minimum value Ms =(4.46)emu/g. With an increase in the annealing temperature, the coercivity increased initially, which later decreased.

In (2019) Mallesh and Srinivas [25] Investigated have been the thermal stability and magnetic properties of Mn-Zn-ferrite nanoparticles by sol-gel process and for different concentrations ($0\leq x\leq1.0$). The samples were prepared at (1200) °C. The results showed that it is in the cubic spinel and the stability of the spin ferrite phase in the concentration of manganese and annealing temperature in air, oxygen and air argon and superior magnetic properties Ms=(38-90)emu/g, Hc=(1-7)Oe were observed in samples that are annealed and rapidly cooled.

In (2019) Atiya Farheen and Rajender Singh [26] The $Mn_{0.9}Zn_{0.1}Fe_2O_4$ films were deposited by RF-magnetron sputtering on quartz substrates in argon atmosphere at (12) m Torr of partial gas pressure using RF power of (100)W. X-ray diffraction patterns confirm the presence of single-phase cubic spinel structure in all the as-grown films. The magnetization at (300) K is found to decrease with increasing film thickness. Whereas, the magnetization at (80) K is found to increase with increasing film thickness. The magnetic hysteresis, B-H curve for the hydrothermally heated film show more isotropic behavior with improved magnetic properties as compared to the as-grown film.

In (2020) Faten Haithum Mulud ***et al.,***[27] Studying the copper ferrite $CuFe_2O_4$ nanoparticles were synthesized by sol-gel method with different annealing temperatures (200, 450, 650 and 850)°C. The XRD patterns showed the system structure in Cu-ferrite had deformed at (650) °C from a cubic to a tetragonal system with apparent a secondary phase CuO. Lattice constant decreases with increasing annealing temperatures, while crystalline volume increases. The FTIR spectrum of sample formation of a single-phase cubic spinel. Magnetization revealed a soft ferromagnetic behavior for the composition sintered at (850) °C, coercivity were (32) emu/g, (11.64) emu/g and (517.16) emu/g.

In (2020) Talaat M. Hammad ***et al.,*** [28] $Cu_{1-x}Mg_xFe_2O_4$ ($x = 0.2$, 0.4, 0.6, 0.8, and 1.0) nanoferrites were synthesized by using a method of a co-precipitation method to study the impact of magnesium substitution in altering the structural, optical and magnetic properties of copper ferrites. Also the size of the crystallite determined from XRD results and lattice constant decreases from (8.465)Å to (8.334)Å. With increasing Mg concentration, the nanoparticle size decreased from (17.4) to (10.2) nm. With the increase of Mg^{+2} ion, saturation magnetization and remanent magnetization decreases when Mg^{+2} substitutes Cu^{+2}.

In (2021) J Gil-Monsalve ***et al*.,** [29] In this study nickel ferrite thin films have been grown on strontium titanate-100 single crystal substrate by using RF magnetron sputtering. X-ray photoelectron spectroscopy and reflection electron energy loss spectroscopy were employed. In the X-ray photoelectron spectra of Fe 3p, the presence of the valence states Fe^{+2} and Fe^{+3} was evidenced. The magnetic properties were analyzed by vibrating sample magnetometry indicating easy magnetization.

In (2022) Muhammad Adnan Munir ***et al*.,** [30] This work focused on enhancing the magnetic and dielectric properties of ferrite $Ni_{0.25}Cu_{0.25}Zn_{0.50}$ by exposure to non-thermal microwave plasma under reduced pressure. A series of $Ni_{0.25}Cu_{0.25}Zn_{0.50}$ was prepared by using the sol-gel method, then oxygen plasma treatment was given with a microwave source. The models were examined with X-ray diffraction analysis, which confirmed the formation the FCC cubic structure of all samples. Plasma treatment did not affect the crystallization size. The average crystal size was calculated to be (49.13) nm. Studies confirmed then surface shape changes and particle size reduction upon exposure to plasma. Saturation the magnetization of ferrite exposed to the plasma was approximately (65)% higher. The saturation magnetization, residual magnetization and coercivity of the ferrite exposed to the plasma were calculated as (74.46) emu/g, (26.35) emu/g and (1040) Oe, respectively.

In (2022) A.Safari ***et al.,*** [31] The thin films of $CoFe_2O_4$ were deposited on glass substrates by radio-frequency (RF) sputtering. The effect of RF power variation was studied from (60–120)W on the structure, magnetic of the as-deposited films and films annealed at (500) °C. The magnetic parameters of the film, coercivity (H_c), saturation magnetization (M_s) and remanence (M_r) increase as RF power is increased (60) to (80) W. Annealing of the film significantly improves the magnetic properties. The largest grain size and the best crystallinity of the film are obtained for the film deposited at (80) W of RF power.

In (2023) Ravibabu Kancharla and Ashok Vudayagiri [32] In this work cobalt ferrite films were prepared using magnetized RF sputtering on glass at room temperature and then annealed at (500) °C for a period of (3) hours. The effect was studied of the variation in Ar gas pressure between (8) and (12) mTorr on the crystal structure and magnetic. The XRD shows a single-phase spinel nanostructure. The FESEM images confirm the nano-crystalline nature of the films as well as the granular formation, which indicated an increase in the grain size (30-40-63) nm with the increase of Ar pressure. Magnetic studies have shown that annealing can significantly improve the magnetic properties of exposed cobalt ferrite films.

1.3 Aim of Work

1-Preparation of two types of iron spinel MFe_2O_4 with different proportions as nanoparticles and forming them in different shapes using sol-gel technology.

2- Studying the composition, surface shape and magnetic properties of these materials to obtain ferrous materials used as a basis in electrical transformers and many other uses.

3- Investigate the effect of plasma, produced by RF magnetron system on the microstructure and magnetic properties of prepared samples, to obtain ferritic materials used as a core in electrical transformers and as a good magnet.

Chapter Two

Theoretical Part

2.1 Ferrites

A ferrite is a ceramic material made by mixing and firing large proportions of iron oxide (Fe_2O_3) blended with small proportions of one or more additional metallic elements, such as Sr , B, Mn, Ni and Zn [30]. Ferrite of main property is that, in the magnetized case, all the spin magnetic moments are not polarized in the same direction. Few of them in the inverse direction, because spin magnetic moments are two types have various values, net magnetic torque will have some limited value. Ferrites have the molecular formula isMFe_2O_4, where (M) refer to the divalent metal such as Co, Mn, Fe, Ni, Cu, Mg, Cd or Zn. There are eight molecules per unit cell in a spinel structure [33].

This crystal structure has based on a face-centered cubic structure (FCC) of oxygen anions (O^{-2}), whose tetrahedral sites (denoted A) and octahedrons sites (denoted B) are partially occupied by the metal cations M^{+2} and Fe^{+3}. Only half of the octahedral sites and one-eighth of the tetrahedral sites are occupied [33].

Since the middle of the last century ferrite has been studied as it has effects on magnetic applications. The ferrite resistance of at room temperature can vary depending on their chemical composition, to other magnetic materials ferrite is excellent because it has low eddy current losses and high electrical resistance, another important factor, which is of considerable importance in ferrites [34]. The properties of ferrites have been improved because of the increasing way in ferrites technology.

2.2 Types of Ferrites

According to its magnetization ferrites can be divided into two types hard and soft. This classification depends on the ability of ferrite to magnetize or demagnetize, our research work is on spinel ferrite; therefore we shall discuss in detail the spinel ferrite only.

2.2.1 Soft Ferrites

Soft ferrites are those with the ability to easily attract or remove their magnets. That soft magnetic this indicates materials have a high magnetization and a low coercive field is wanted in many applications. The hysteresis loop for a soft ferrite have to be thin and long, therefore the energy loss is very low in the soft magnetic material. Examples are manganese, nickel, iron, cobalt, etc., they are utilized in microwave devices, inductors, cores and transformer recording heads. Where efficient applications of magnetic cores in sensing and power electronics require low-loss and versatile soft magnetic materials, with excellent response on a wide range of frequencies [35].

2.2.2 Hard Ferrites

Hard ferrites are known as permanent magnetic materials because they would can hold their magnetism after being magnetized, also have large hysteresis loop and large energy losses during magnetization, which have a high coercivity. Iron oxide and barium or strontium carbonate are used in manufacturing of hard ferrite magnets [35]. The high coercivity means the materials are very resistant to becoming demagnetized, an essential characteristic for a permanent magnet. They also have high magnetic permeability. These so-called ceramic magnets are cheap and are widely used in household products such as refrigerator magnets [36].

2.3 Types of Ferrites According to Structures

Ferrites are ferrimagnetic ceramic compound materials has populations of atoms with opposing magnetic moments having high resistivity and consisting of various mixtures of iron oxides and the oxides of other metals. Depending upon the crystal structure, ferrites are of following types [37]:

(1) Spinel ferrites (Cubic ferrites).

(2) Garnets.

(3) Hexagonal ferrites.

2.3.1 Spinel Ferrites

The spinel is by far the most widely used ferrite. The spinel structure is derived from the mineral, spinel whose structure was elucidated by Bragg (1915). Analogous to the mineral spinel, magnetic spinels have the general formula $MOFe_2O_3$ or MFe_2O_4 where M is the divalent metal ion like Mg, Ni, Fe, Cu, Mn, Zn, Co , etc, or a mixture of more than one of these elements. The spinel ferrite because their crystal structure is very similar to that of the mineral spinel $MgO\text{-}Al_2O_3$.

All cubic ferrites except for cobalt ferrite $CoFe_2O_3$ are magnetically soft or easily magnetized in a small field [38]. The unit cell of spinel ferrites is face center cubic (FCC) with eight formula units per unit cell. The formula can be written as $M_8Fe_{16}O_{32}$, anions are the largest and form the FCC lattice, within these lattices, two types of interstitial positions occur and are occupied by mineral cations, as shown in Figure (2.1) [39].

It has remains to note that the case is in the formation of the spinel phase the diameter of the Me^{+2} ion should not exceed about 1 Å, because Coulomb's forces have insufficient to ensure the stability of the crystal structure when it is larger, the Table (2.1) represents the radii of some positive ions [40].

2.3.1.1 Tetrahedral Sites

In the tetrahedral site the interstitial has in the center of a tetrahedra forms by four lattice atoms. Three atoms, touching each other, are in plane; the fourth atom sits in the symmetrical position on top. The cation occupies the void created at the center of the cube.

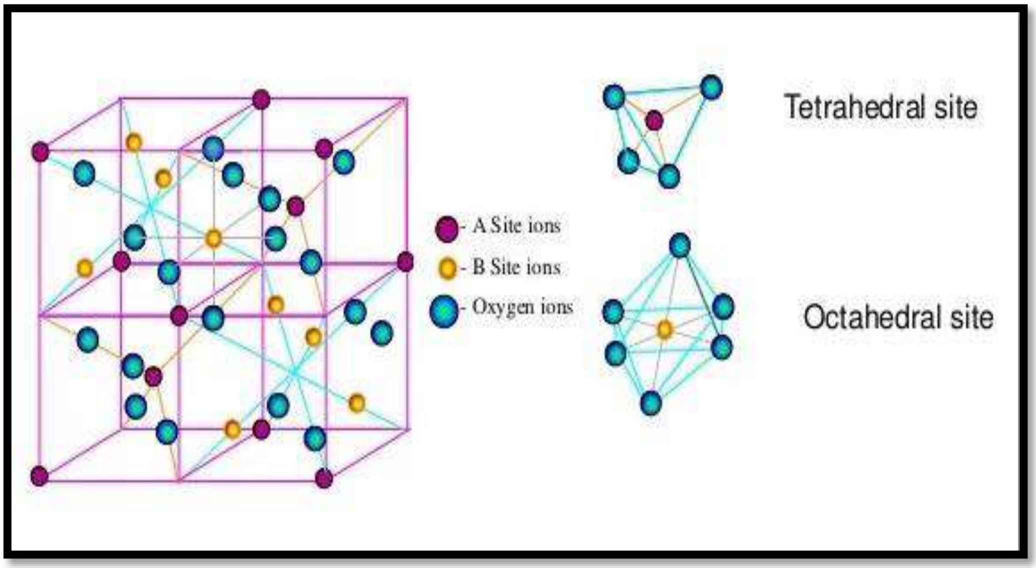

Figure (2.1): The crystal structure of spinel ferrite from tetrahedral and octahedral sites [39].

For charge neutrality of the system, only 8 tetrahedral (A) sites are occupied by cations out of 64 sites per unit cell in FCC crystal structure. Figure (2.1) shows the tetrahedral position in the FCC lattice and the tetrahedral site has a defined geometry and offers space for an interstitial atom [41].

Table (2.1): The radii for some ions in units of Å[40].

Valence +		Valence ++		Valence +++		Valence ++++	
Element	**Radii**	**Element**	**Radii**	**Element**	**Radii**	**Element**	**Radii**
Li	0.7	Mg	0.75	Al	0.53	Ti	0.68
Na	1.00	Ca	1.05	Cr	0.70	V	0.57
Tl	1.50	Mn	0.82	Mn	0.67	Mn	0.52
		Fe	0.77	Fe	0.63	Sn	0.65
		Co	0.78	Y	0.95	Zr	0.80
		Cu	0.70	In	0.95	Pb	0.70
		Zn	0.74	Sr	0.83	Ru	0.60
		Cd	0.92	V	0.75	Rh	0.65
		Sr	1.18	Ga	0.65	Os	0.65
		Ba	1.38	Ti	0.70	Ir	0.65
		Ti	0.76	Co	0.65	Pt	0.55
		Sn	1.02	Ln	1.15		
		Pb	1.18	Ti	0.95		
		Pt	0.52	Pr	1.09		
				Nd	1.07		
				Rh	0.75		

2.3.1.2 Octahedral Sites

An octahedral position for an (interstitial) atom has the space in the interstices between 6 regular atoms that form an octahedra. Four regular atoms are positioned in a plane, the other two are in a symmetrical position just above or below. All spheres can be considered to be hard and touching each other. The six spheres define a regular octahedra, in its interior there is a defined space for an interstitial atom, bordered by six spheres. Octahedral sites exists in FCC and BCC crystals. The other prominent geometric environment for interstitials is the tetrahedral site. For charge neutrality, 16 octahedral (B) sites are occupied by cations out of 32 sites in a spinel structure. In FCC there are (4) octahedral sites per unit cell, Figure (2.1) shows the octahedral position in the FCC lattice [41].

2.3.2 Garnets Ferrite.

The chemical formula for ferrimagnetic garnet is $Me_3Fe_5O_{12}$ where, Me is a trivalent ion such as rare earth or yttrium. The unit cell is cubic and contains eight molecules of $Me_3Fe_5O_{12}$ (160 atoms). The Me ions occupy the dodecahedral sites (called c sites), where they are surrounded by eight oxygen ions, the Fe^{+3} ions distributed over the tetrahedral and octahedral sites in the ratio 3:2, as in the case of spinels the magnetic alignment results from super exchange interaction via the intervening oxygen ions and the interaction is expected to be greater for the shorter the Me-O distance and closer the Me-O-Me angle is to 180^0[42].

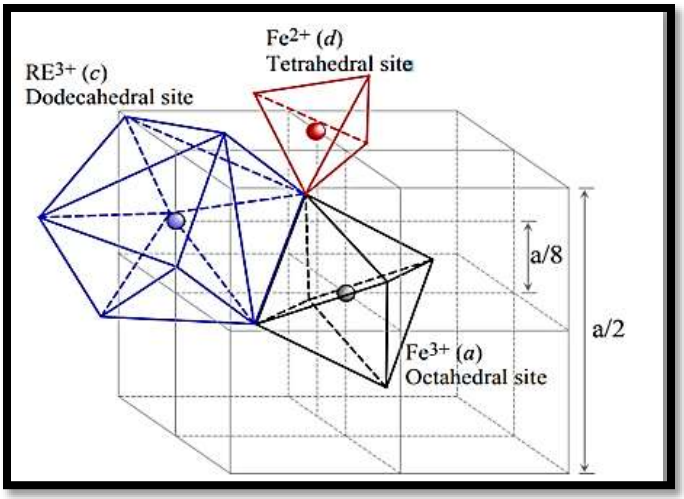

Figure(2.2): The structure crystal to Garnet [42].

2.3.3 Hexagonal Ferrites

The hexagonal ferrites are a group of ferromagnetic oxides in which the principal component is $MeFe_{12}O_{19}$ where Me is a divalent ion of a large ionic radius, such as Ba^{+2}, Sr^{+2} or Pb^{+2}. The most important in this group is barium ferrite which is magnetically hard and referred to as permanent magnets [43]. Hexa ferrites all of hexagonal ferrites are synthetic; barium hexa ferrite ($BaFe_{12}O_{19}$) possesses the same structure as the natural mineral magnetoplumbite, these materials feature hexagonal close-packed framework of oxides, where some of the oxygen centers are replaced by Ba^{+2} ions. Formulas for these species include shown in Figure(2.3), it has very good magnetic properties that make it suitable are wide as permanent and have high coercivity [44].

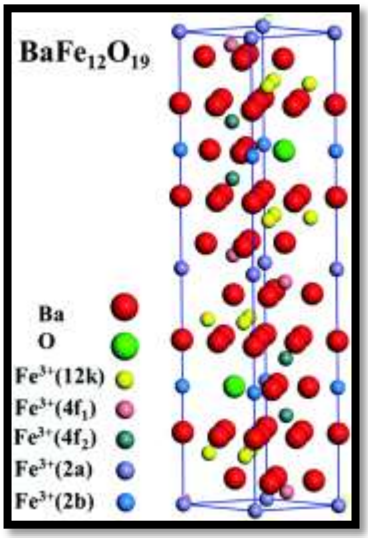

Figure(2.3): The schematic structure of the hexagonal ferrites $BaFe_{12}O_{19}$[45].

2.4 Types of Spinel Ferrites

The spinel ferrites have been classified into three categories due to the distribution of cations on tetrahedral (A) and octahedral (B) sites.

(1)Normal spinel ferrites.

(2) Inverse spinel ferrites.

(3) Mixed spinel ferrites.

2.4.1 Normal Spinel Ferrites

In the spinel lattice of a unit cell, eight tetrahedral and sixteen octahedral sites are occupied by metal ions or by 1 tetrahedral and 2 octahedral for each formula unit. In these ferrites, the divalent cations occupy tetrahedral (A) sites while the trivalent cations are on octahedral (B) sites. Square brackets are used to indicate the ionic distribution of the octahedral (B) sites. Normal spinel has been explaining by the formula $(M^{+2})_A[Me^{+3}]_B O^{-2}{}_4$ where (M) represents divalent ions and (Me) for trivalent ions shown in Figure(2.4). A typical example of normal spinel ferrite is $ZnFe_2O_4$, $CdFe_2O_4$ [38].

2.4.2 Inverse Spinel Ferrites

When all Me^{+2} are in B-positions and Fe^{+3} ions are equally distributed between A and B-sites, the structure is referred as inversed spinel. The structural formula of these ferrites are Fe^{+3} $[Me^{+2}Fe^{+3}]O_4{}^{-2}$. Magnetite Fe_3O_4, ferrites $NiFe_2O_4$ and $CoFe_2O_4$ have inversed spinel structure [18].In the inversed ferrites, one half of Fe^{+3} is placed in A-sites and another half in B-sites [46]. This type of spinel ferrite is schematically illustrated in Figure(2.5).

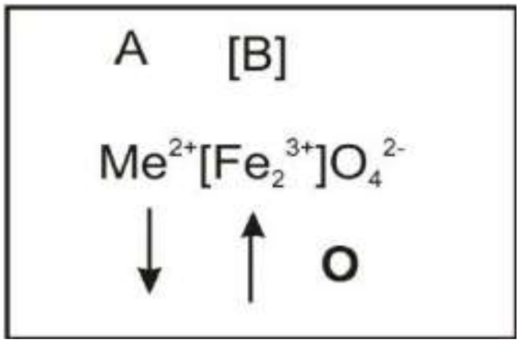

Figure (2.4) :Cation distribution in normal spinel ferrites[46].

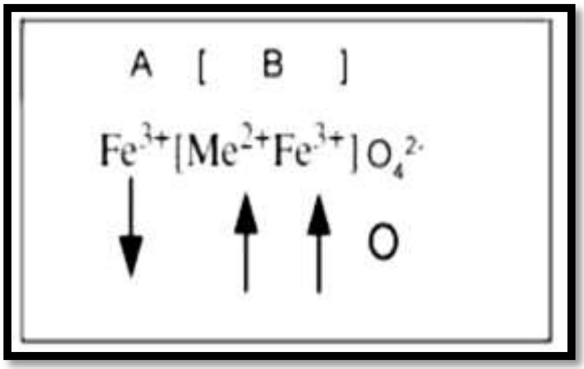

Figure (2.5):Cation distribution in inversed spinel ferrites[46].

2.4.3 Mixed Spinel Ferrites:

If cations Me^{+2} and Fe^{+3}occupy both A and B-positions, the ferrite is called mixed spinel. It is the structural formula of this ferrite is $Me_{1-\delta}^{+2}Fe_{\delta}^{+3}$ $[Me_{\delta}^{+2}Fe_{2-\delta}^{+3}]O_4^{-2}$, where δ is the degree of inversion. These are schematically illustrated in Figure (2.6). $MnFe_2O_4$ represent this type of structure and has an inversion degree of δ=0.2 and its structural formula, therefore, is $Mn_{0.8}^{+2}Fe_{0.2}^{+3}$ $[Mn_{0.2}^{+2}Fe_{1.8}^{+3}]$ O_4^{-2} [47].

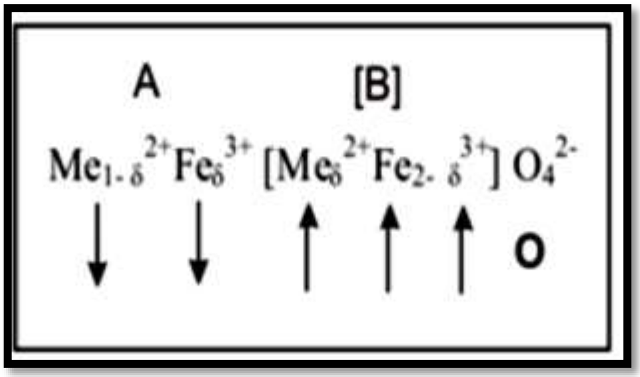

Figure (2.6): The spinel ferrites in mixed of Cation distribution[46].

L. Neel proposed that magnetic moments in ferrites are the total of magnetic moments of individual sub lattices. In spinel structure, interchange interaction between electrons of ions in A- and B-sites have different values.

Usually, the interaction between magnetic ions of A and B-sites (A-B interaction) is strong. The interaction between A-A is most more times weaker than that of A-B interaction while the B-B interaction is the weakest [48].

2.5 Magnetic Domain

A magnetic field is an area within a magnetic material in which the magnetization is in a uniform direction. This means that the individual magnetic moments of the atoms are aligned with each other and point in the same direction. An essential property of any charged particle is that when it is in motion, it generates a magnetic field around its travel path. Electrons are negatively charged particles and they create electromagnetic fields around themselves as they move [49]. Electrons are known to orbit around atomic nuclei, and they create magnetic fields while doing so, if one or more atoms or groups of atoms were taken and aligned , the total magnetic field would be present in this region of matter, as shown in Figure (2.7). In regular iron, these magnetic domains are randomly arranged [50].

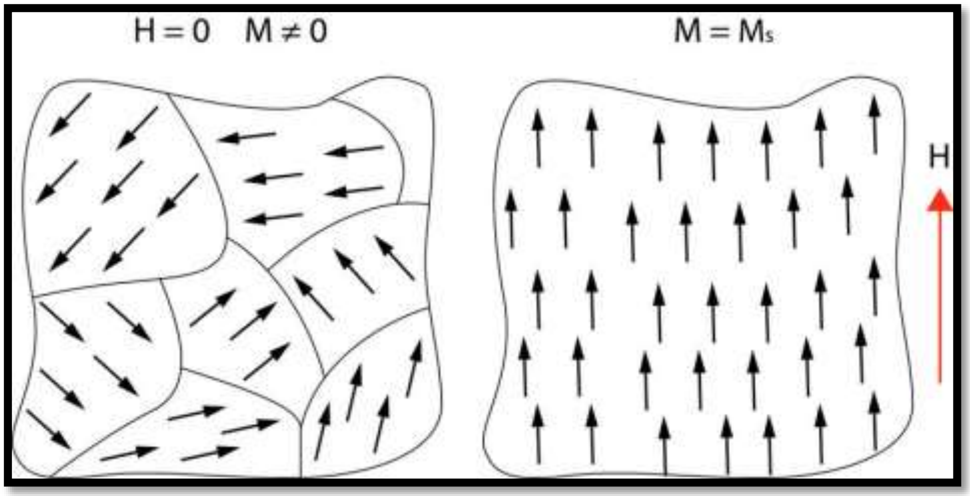

Figure (2.7): Magnetic domain[49].

In a ferrite domain, the net moments of the antiferromagnetic interactions are spontaneously oriented parallel to each other. Domains typically contain atoms and are separated by domain boundaries. The magnetic field is represented by its field quantities which is the magnetic flux density (B) which is measured in (Tesla) units and the magnetic field strength (H) calculated from the electric current that generates the magnetic field is measured in units (A/m) in the magnetic material and the relationship between B and H [50]:

$B= \mu H = \mu_0\mu_r H$ …………(2- 1)

$B= \mu_0 H+\mu_0 M$ …………… (2- 2)

where

(μ_0) : Vacuum permeability ($4\pi *10^{-7}$ H/m).

(μ_r) : Relative permeability.

(M): Magnetization(is the sum of magnetic moments mj of a unit of volume of magnetic matter)[50].

$\mu_r = \boldsymbol{\mu} / \mu_0$ …………….(2-3)

The magnetic properties of magnetic materials are also described in the way that the value of M differs with value H. The ratio of these two quantities is called the magnetic susceptibility χ [50].

$\chi = \frac{M}{H}$ ………..……(2-4)

from equation (2-1), (2-2), (2-3) and (2-4) we get [51]:

$\mu= \mu_0(1+ \chi)$ ………(2-5)

2.6 Classification of Magnetic Materials

The best way to introduce different types of magnetism is to describe how materials respond to magnetic fields. The main difference is that in some materials there is no group interaction of atomic magnetic moments, while in other materials there is a very strong interaction between atomic moments.

2.6.1 Diamagnetism

Diamagnetism materials consist of atoms or molecules that these materials will saturate their orbits with electrons and so their magnetic moment must be zero. When a material is placed in a magnetic field, the electrons atomic orbitals tend to reverse the external magnetic field by motion the induced magnetic moment is in an opposite direction outward. This is known as diamagnetism. Magnetic diamagnetism it can be understood from Figures (2.8) (a) and (b). Diamagnetic materials have very small negative susceptibility(10^{-6}) and the transmittance coefficient is less than one. When the field is removed, its magnetization becomes zero, examples of some diamagnetic materials are gold, silver, mercury, copper and zinc [52].

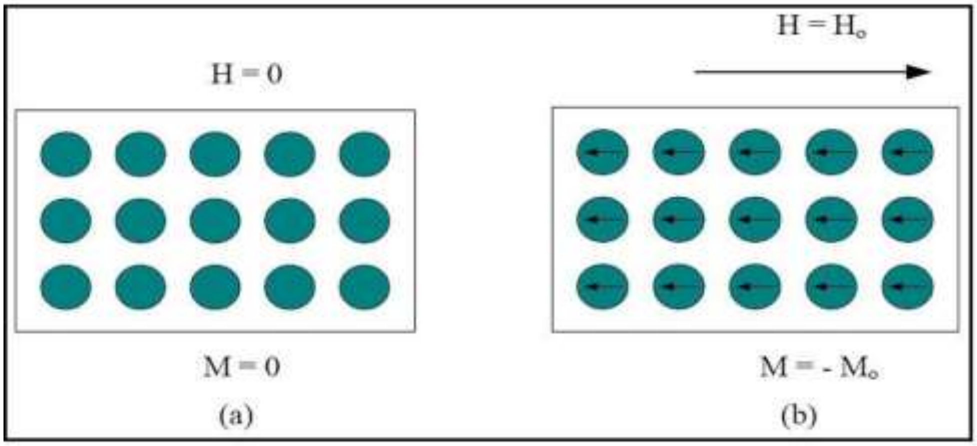

Figure (2.8): Schematic of the induced dipole moment in diamagnetic material [53].

2.6.2 Paramagnetism

Each atom or molecule in some materials, possesses a permanent magnetic moment individually due to its orbital and rotational magnetic moments. In the absence of an external magnetic field, the individual atomic magnetic moments are randomly oriented, but when an external magnetic field is applied, the individual atomic magnetic moments tend to align themselves in the direction of the externally applied magnetic field and lead to a weak non-zero magnetization as shown in the Figure (2.9) (a) and (b)[53].

Paramagnetism occurs in materials with permanent magnetic dipole moment. Paramagnetic materials also exhibit ferromagnetism and these materials follow the law (Curie Weiss) and that the permeability of these materials has a positive value and less than one the range between(10^{-3}-10^{-5}), for examples of these materials(aluminum, calcium, titanium, potassium, magnesium, sodium) [54].

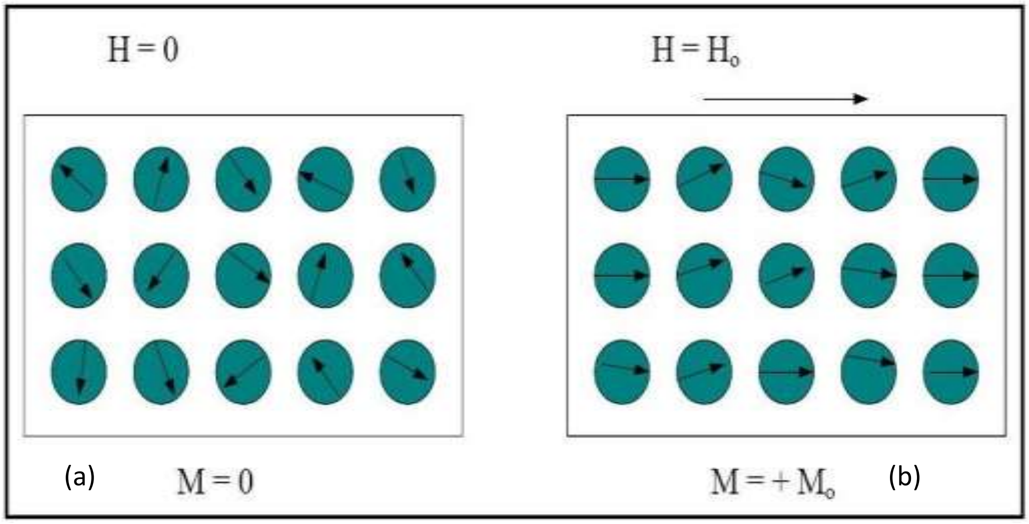

Figure (2.9): Schematic of behavior of dipole moment in a paramagnetic solid[53].

2.6.3 Ferromagnetism

Ferromagnetism is a phenomenon of spontaneous magnetization. They only appear below a certain temperature, known as the Curie temperature. Above the Curie temperature, the moments are randomly oriented resulting in a net magnetization of zero. Ferromagnetism is only possible when atoms are arranged in a lattice and the atomic magnetic moment can interact to parallel each other, Figure (2.10). The ferromagnetic material has spontaneous magnetization due to the alignment of its atomic magnetic moments even in the absence of an external magnetic field [53].These exhibit strong attraction to magnetic fields and are able to retain their magnetic properties after removal of the external field [12].Its magnetic susceptibility varies according to the Curie-Weiss law, $\chi = C / T - T_C$ [53].

These materials have a large and positive magnetic susceptibility to an external magnetic field in the range (10^5) and have a permeability coefficient greater than(1). Examples of ferromagnetic materials are the transition metals Fe, Co and Ni [55].

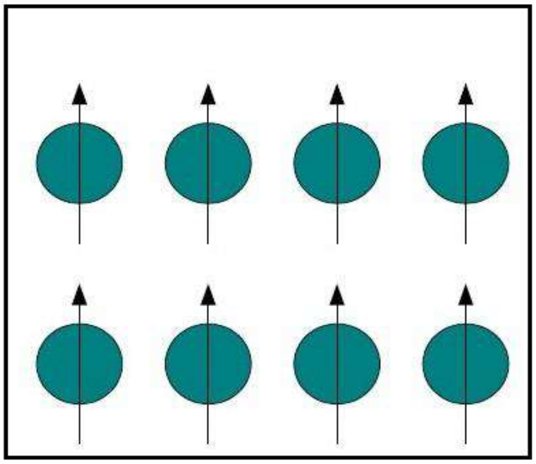

Figure (2.10): Schematic of spontaneous alignment of dipole moments in the applied field [53].

2.6.4 Antiferromagnetism

Antiferromagnetic materials that have a dipole that has equal moments, but the adjacent dipole points are in opposite directions. The magnetic moments are distributed in equal numbers on two secondary networks so that the direction of the moments in one of the secondary networks is parallel to each other and opposite to the other network Figure (2.11), so the sum of the external moments of the primary network is zero [53]. These materials have weak positive magnetic sensitivity (10^{-3}). The antiferromagnetic ordering in antiferromagnetic materials is the reason for the small magnetic susceptibility of antiferromagnetic materials, examples of which are MnO, FeO and NiO [56].

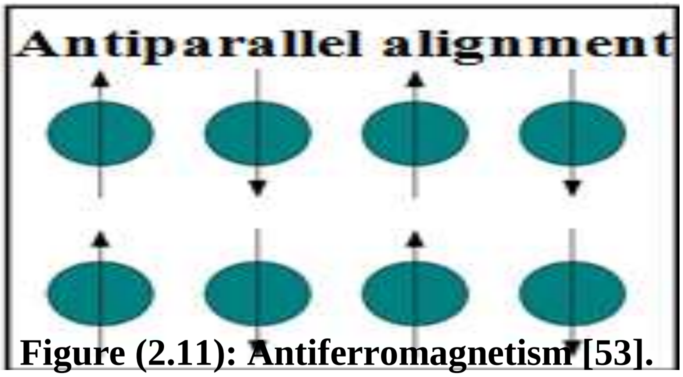

Figure (2.11): Antiferromagnetism [53].

2.6.5 Ferrimagnetism

They are magnetic materials that have a spin structure for both the spin and up components but have a non-zero net magnetic moment in one of these directions. The magnetic moments of atoms on different adjacent sublattices are opposite to each other as is the antiferromagnetism, however, in ferromagnetic materials the opposing moments are unequal Figure (2.12) [53]. Ferrimagnetism is only observed in compounds, which have more complex crystal structures than the pure elements. These materials, like magnetic materials, have spontaneous magnetization below a critical temperature called the Curie temperature (Tc). The best example of this material is an iron oxide where ferrite material belongs to it [57].

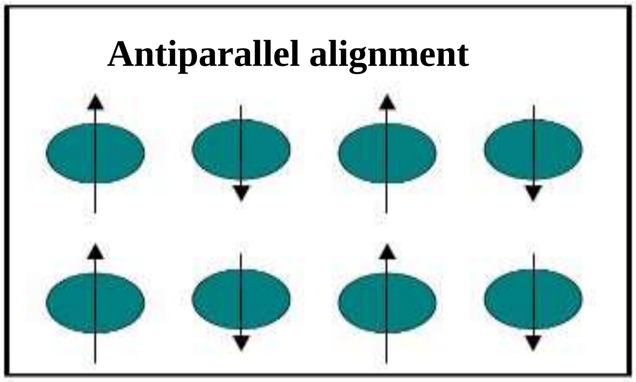

Figure (2.12): Ferrimagnetism [53].

2.7 Magnetic Properties

2.7.1 Permeability

It is a measure of the ease with which magnetic flux through matter and ferromagnetic materials that are a function of intensity the magnetic field. Complex permeability is used to describe magnetic materials on a large range from frequency. The Permeability at high frequencies, the permeability is complicated value [57].

$$\mu_r = \mu_r^{\prime} - i\mu_r^{\prime\prime} \quad \ldots\ldots\ldots(2\text{-}6)$$

where:

($\mu_r^{\prime}$): Real part of Permeability.

($i\mu_r^{\prime\prime}$) : Imaginary part of permeability, (i) is a constant whose value is equal $\sqrt{-1}$

The real part of permeability is the magnetic energy stored in the material and the imaginary part represents energy lost in the material, from the Figure (2.13) the loss angle (δ) calculate from [57].

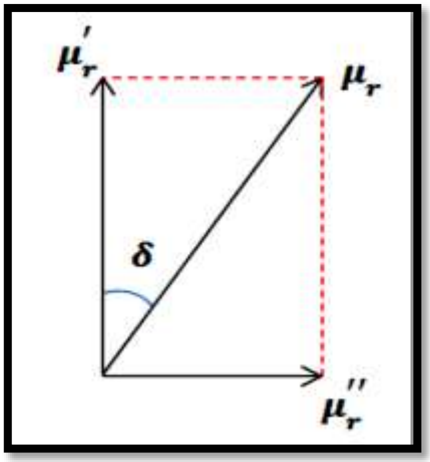

Figure (2.13): Angle of loss in the material [57].

$$\tan \delta = \frac{i\mu r''}{\mu r'} \ldots\ldots\ldots\ldots\ldots (2\text{-}7)$$

Ferritic materials have a high magnetic permeability that is 10,000 times greater than vacuum permeability but the magnetic properties of ferritic materials have lower values than those of metals magnetism [57].

2.7.2 Magnetization

Ferromagnetic and ferrimagnetic materials are most important because they are attracted to the magnet strongly sensitive because it contains electrons that are not bound in their atomic structure and also, the magnetic moments of electrons tend to be parallel to the applied outer field [58].

2.7.3 Hysteresis Loop and Curve Magnetization

Dipoles are affected by a group of forces, which are the(inner forces) that attract and repulse each other and(external forces), a random force that the substance obtained from thermal energy external. Where dipoles are arranged in directions that may differ with each other so that their effect becomes outer is zero. When an external magnetic field is applied to that material, the field directs the dipoles to it, so if the field succeeds in directing these diodes, these materials are called magnetic materials, but if the field does not succeed in directing it towards it, because there are substances that have forces external and internal are much larger than the applied field, as the field obtained remains equal to zero and these materials are called non-magnetic materials (paramagnetic) [59].

In Figure (2.14) this graph of H versus B is called B−H graph or hysteresis loop. A piece of ferromagnetic substance can be magnetized by placing it in a solenoid and passing a current through it. If the value of current increases gradually, the magnetic field intensity H also increases. As a result, the magnetic induction B produced in the specimen also increases [60].

At point "a" almost all of the magnetic domains are aligned and an additional increase in the magnetic field intensity will produce very little increase in magnetic induction. The material has reached the point of magnetic saturation (B_s and M_S). When continuing to increase the field strength, the magnetization (M) takes constant values, while (B) continues to increase due to the increase in (H) that forms part of its formation according to equation (2-8) [60] .

$$B=H + 4\pi M \quad …….. (2\text{-}8)$$

When H is reduced to zero, the curve will move from point "a" to point "b", it can be seen that some magnetic induction remains in the material (Br) even though the magnetic field intensity H is zero.

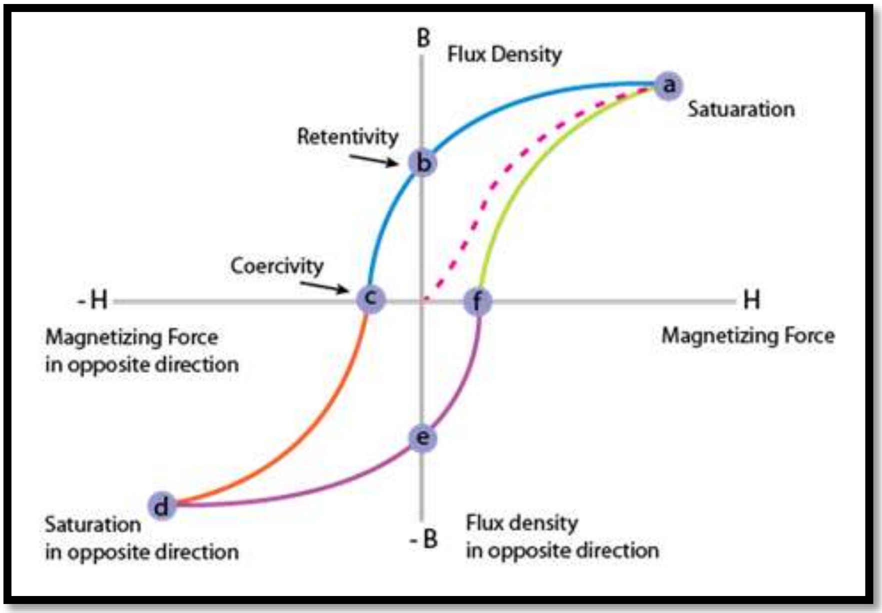

Figure (2.14): Hysteresis loop[60].

This is referred to as the point of retentivity on the graph and indicates the remanence or level of residual magnetism in the material. As the magnetic field intensity is reversed, the curve moves to point "c", where the flux has been reduced to zero. This is called the point of coercivity ($-H_c$) on the curve. The force required to remove the residual magnetism from the material is called the coercive force or coercivity of the material [59]. As the magnetic field intensity H is increased in the negative direction, the material will again become magnetically saturated ($-H_s$,$-B_s$) but in the opposite direction point "d". Reducing H to zero brings the curve to point "e". It will have a level of residual magnetism equal to that achieved in the other direction. Increasing H back in the positive direction will return B to zero [58].

The loss of magnetic energy in a unit volume of the sample depends on the area of the hysteresis ring and that the loss of energy manifests itself in the form of heat leading to a rise in the temperature of the sample. Thus, materials that have a small and narrow area of the hysterical loop are called soft ferrite materials shown in Figure (2.15a). These requires materials with a wide and wide-area hysterical loop called hard ferrite Figure (2.15b), these materials are made of permanent magnets such as, disks and magnetic tapes and the computer industry [61].

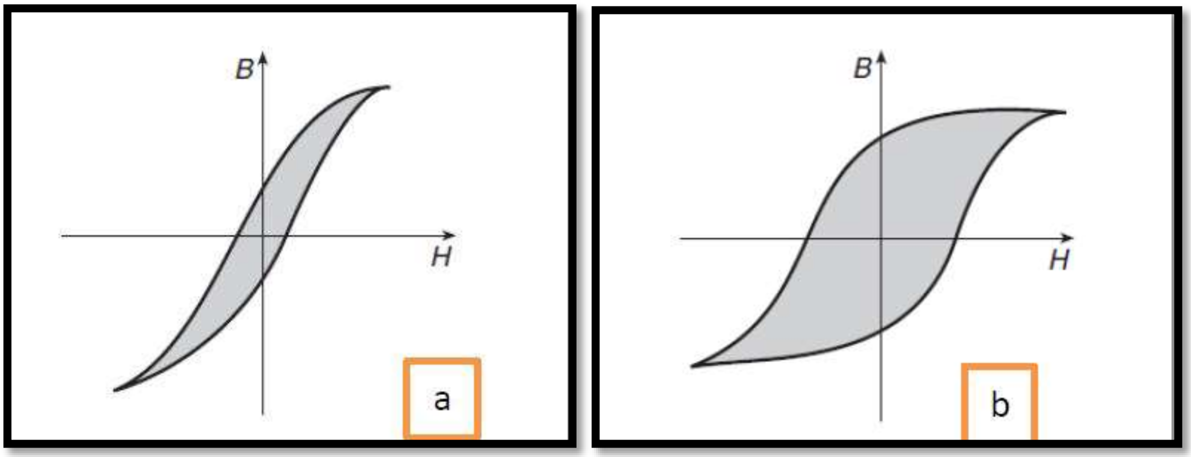

Figure (2.15) : Hysteresis loop for the material. (a) Hysteresis loop for the soft material.(b) Hysteresis loop for hard materials [61].

2.8 Application of Ferrites

Ferrites are very important magnetic materials because of their high electric resistivity. Ferrite has a vast application from microwave to radio frequencies. It is used for antenna cores in radio receivers, broad band transformer, ultrasonic generator, moderators, isolators. Now a day ferrite is used in telephone exchange, computers, and control equipment. Ferrite is a magnetic material of two types one is soft ferrite and second is the hard ferrite. Soft ferrite is class of magnetic material used as transformer core mainly for television, telecommunication computer, medical and other industrial electronic system [62]. Hard ferrites are used for permanent magnets mainly in loud speakers, micro motors. Ferrite is a ferromagnetic material also ferrite is an inverse spinel taken to be collinear ferrimagnet. The low loss polycrystalline ferrites should be used in a high frequency range, can to a large extent control most parameters for any particular applications [62].

2.9 Preparation Techniques

Methods for preparing ferrites have an important role in the properties of the resulting ferrite in terms of structural properties, particle size, phase purity, impurities, porosity, surface defects and magnetic electrical properties. etc. These parameters can be largely controlled by choosing the appropriate tuning technique with the appropriate preparation conditions.

As ferrite can be prepared in several different ways and the materials are used in their solid-state in each of these ways to produce ferrite in different forms (multiple crystals, single crystals, thin or thick films). There are two different ways to collect materials [63].:

1. Conventional ceramic method.
2. Wet chemical methods.

2.9.1 Conventional Ceramic Method

The most common way to prepare ferrite materials is solid-state reactions or so-called conventional ceramic method. The process of selecting the raw materials in the reaction is the key to reaching the final product with desirable specifications, as the raw material contains impurities that have a significant impact on the magnetic properties of production ferrite. As well as, the appearance of undesirable stages and phases and the selected raw materials are in the form of oxides or salts of elements such as chlorides, nitrates, carbonates, a mixture of raw materials according to the type of ferrite required [64]. One of the advantages of this method is that it is inexpensive and can produce large amounts of ferrite and its disadvantages are insufficient ability to control equivalences because it requires long heating at very high temperatures [65].

2.9.2 Wet Chemical Method

The wet chemical analysis involves identifying and quantifying the desired elements present in a liquid sample using several methods[66]:

1. Co-precipitation method
2. Hydrothermal method.
3. Gas/ Aerosol - Phase Methods
4. Sol-gel method.

2.9.2.1 Co-precipitation method.

In co-precipitation reactions, solutions of the salts are prepared for the desired final compound and water-soluble salts are usually used but the insoluble salts in water are dissolved in strong acids such as (NaOH, KOH, NH_4OH, etc.) [67]. The grain begins to grow and begins to aggregate into more thermodynamically stable molecules. The number of nuclei sites, their growth and agglomeration depends upon pH, temperature, stirred speed, and dissolution time[68].

2.9.2.2 Hydrothermal method.

Hydrothermal synthesis a unique method for crystallizing substances from high-temperature aqueous solutions at high vapor pressures [69]. Hydrothermal methods were used in the synthesis of Fe_3O_4 and ultrafine powders, of its features the size of the Fe_3O_4 particles increases when the reaction duration is prolonged and higher water content in precipitating the bigger magnetic iron oxide particles [70].

2.9.2.3 Gas/ Aerosol - Phase Methods

In spray pyrolysis, a solution of ferric salts and a reducing agent in organic solvent is sprayed into a series of reactors. Maghemite particles with size ranging from 5 to 60 nm with different shapes have been obtained using different iron salts in alcoholic solution [71].

2.9.2.4 Sol-gel Method.

The sol-gel process is a more chemical method for the synthesis of various nanostructures, especially metal oxide nanoparticles. This method is based on the hydroxylation and condensation of molecular precursors in solution, originating a “sol” of nanometric particles. The “sol” is then dried or ‘‘gelled’’ by solvent removal or by chemical reaction to get three-dimensional metal oxide network. Gel properties are very much dependent upon the structure created during the sol stage of the sol-gel process [72].

The solvent used is generally water, but the precursors can also be hydrolyzed by an acid or base. Basic catalysis induces the formation of a colloidal gel, whereas acid catalysis yields a polymeric form of the gel. These reactions are performed at room temperature; further heat treatments are needed to acquire the final crystalline state [73].

Utilizing the sol-gel process, it is possible to fabricate advanced materials in a wide variety of forms: ultrafine or spherically shaped powders, thin-film coatings, fibers. The sol-gel process involves hydrolysis and condensation reactions of metal precursors as well as the pH leading to the formation of a three-dimensional inorganic network. Metal hydroxyl groups (M-OH) are formed during the hydrolysis [74].

Drying by evaporation under normal conditions results in a dried gel called a xerogel. Most gels are amorphous, but many crystallize when heated. The final heat treatment pyrolysis the remaining organic or inorganic components and forms the crystalline powder. The xerogel is be a dry solid containing the ferrite in an amorphous form. Therefore on heating ions will migrate to the most favourable sites, forming close-packed structure [75].

Sol-gel synthesis provides an extremely easy method of creating a large variety of metal oxides from their metal salts at ambient conditions and at low temperatures. The drawback of the method is that it generates 3D oxide networks, and hence, it is limited in its efficiency regarding the formation of independent, disconnected nano sized particles [76].

2.10 Structural and Morphological Characterization

2.10.1 X-ray Diffraction (XRD)

It is a method to find out the arrangement of atoms inside crystals, where X-rays strike the crystal and deviate towards several specific directions. Based on the angles and intensity of those deflected rays, the crystallizer produces a three-dimensional picture of the electron density inside the crystal. Based on this electron density, the locations are known as an arithmetic mean of the atoms within the crystal, as well as their chemical bonds and other information [77]. When an X-ray beam falls on a crystalline material at a certain angle, diffraction at the intersecting planes occurs due to the coherent scattering of atoms, because the wavelength of X-rays is similar to the distance between atoms, therefore, the diffraction produced by different levels gives a specific diffraction pattern. The singular waves of different atoms interfere with each other and the resulting intensity distribution is modified by this interaction, measuring the diffraction model allows us to infer the distribution of atoms in a substance [78]. Bragg‟s law below provides the required condition for the diffractions coming from different planes. The Bragg‟s law for the diffraction can be written as [77]:

$$m \lambda = 2 d_{hkl} \sin\theta \ \ldots\ldots\ldots (2\text{-}9)$$

where:

(m): is a positive integer that represents the diffraction order.

(λ): is the wavelength of the incident X-ray beam.

(θ): Bragg's diffraction angle of the XRD peak and the interplanar.

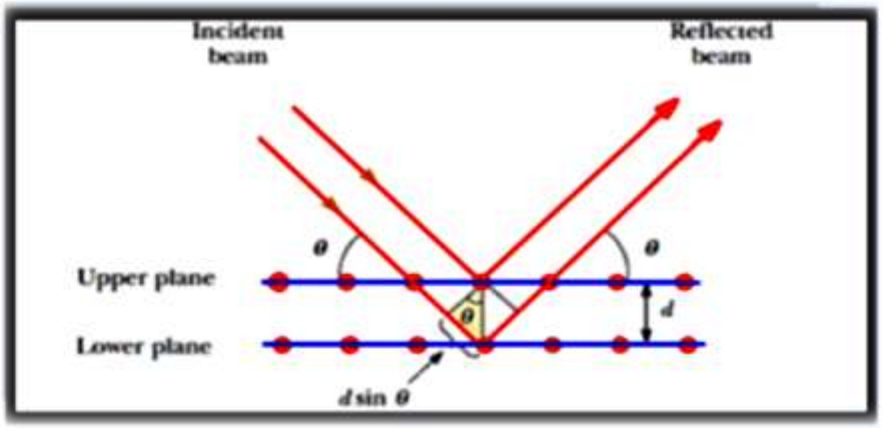

Figure (2.16): Bragg‟s diffraction[77].

(d_{hkl}): the distance can be determined. Figure (2.16) shows the (XRD) that satisfies Bragg‟s condition.

2.10.1.1 Interplanner Spacing (d_{hkl})

Inter planar spacing can be calculated from the X-ray diffraction profiles using the Bragg's formula equation (2-9).

2.10.1.2 Lattice Constant (*a*)

Lattice constant (*a*) can be calculated of a particular cubic and hexagonal structures for various sets of planes are given by [79]:

$$d_{hkl} = \frac{a}{\sqrt{h^2+k^2+l^2}} \quad \ldots\ldots\ldots\ldots.\ldots. \quad (2\text{-}10)$$

$$\frac{1}{d_{hkl}} = \frac{4}{3}\left(\frac{h^2+k^2+hk}{a^2}\right) + \frac{l^2}{c^2} \quad \ldots\ldots \quad (2\ \text{-}11)$$

where:

(a) and (c): Lattice constant.

(hkl): Miller indices.

(c): Lattice constant for hexagonal.

Bragg‟s condition given by equation (2-9) demands that a proper combination of θ and λ is found for efficient reflection. Lattice in three dimensions generally has three lattice constants, referred as a, b, c. However, in cubic crystal structures all of the constants are equal and it is only referred to "a".

2.10.1.3 Crystallite Size (D)

The crystallite size (D) can be estimated using Scherrer's method to calculate the nanocrystallite size by XRD radiation of wavelength λ (nm) from measuring full width at half maximum of peaks (β) in radian located at any 2θ in the pattern. X-ray line broadening method was used to determine the particle size of ferrite by using Deby Scherrer's equation [80].

$$D = \frac{k\,\lambda}{\beta \cos \theta_{\beta}} \quad \ldots\ldots\ldots(2\text{-}12)$$

where**:**

(D): The crystallite size.

(k): 0.9 is (shape constant).

(λ): Wavelength of incident X-ray radiation = (1.54056Å).

(β): Full width at half maximum of the peak(radian) FWHM.

(θ_{β}) : Bragg diffraction angle of the XRD peak (degree).

The erosions can also be calculated using X-ray diffraction, using the formula [80]:

$$S = \frac{1}{D^2} \dots . \dots \dots \quad (2 - 13).$$

2.10.2 Field Emission Scanning Electron Microscope (FESEM)

Field emission scanning electron microscopy (FESEM) is the best known and most widely-used of the surface analytical techniques. High resolution images of surface topography, with excellent depth of field, are produced using a highly-focused, scanning (primary) electron beam. The primary electrons enter a surface with an energy of (0.5 – 30) kV and generate many low energy secondary electrons.

The intensity of these secondary electrons is largely governed by the surface topography of the sample, an image of the sample surface can thus be constructed by measuring secondary electron intensity as a function of the position of the scanning primary electron beam. High spatial resolution is possible because the primary electron beam can be focused to a very small spot (<10 nm) [81].

2.10.3 Fourier Transmission Infrared Ray Technology (FTIR)

Fourier transform infrared spectroscopy (FTIR) is a powerful technique that detects the vibrational characteristics of chemical functional groups in analyzed sample, when infrared radiation (IR) radiation is passed through a sample, some of the IR is absorbed by the sample and some of them are transmitted through the sample [82].

FTIR is also used for identification of the structure of samples as well as identification of unknown materials using the frequencies of the vibrational modes. The field of frequencies used between(400-4000)cm^{-1} corresponds to the field of vibration energy of the particles of matter and that most of the molecular vibrations occur in this region can find enough information in that to determine the molecular [83].

2.10.4 Vibrating Sample Magnetometer (VSM)

A vibrating-sample magnetometer (VSM) is a scientific instrument that measures magnetic properties based on Faraday’s Law of Induction. A sample is first placed in a constant magnetic field and if the sample is magnetic it will align its magnetization with the external field. The magnetic dipole moment of the sample creates a magnetic field that changes as a function of time as the sample is moved up and down. The alternating magnetic field induces an electric field in the pickup coils of the VSM. The current is proportional to the magnetization of the sample - the greater the induced current, the greater the magnetization. As a result, typically a hysteresis curve will be recorded and from there the magnetic properties of the sample can be deduced [84].

2.11 Plasma

A common definition of plasma is an ionised gas that is generated by either the disintegration of polyatomic gas molecules or the elimination of electrons from monatomic gas casings. Nevertheless, macromolecular neutrality (quasi-neutrality) is a necessary condition for plasma, so not all ionised gases containing charged particles qualify) is plasma. Neon signs and lightning are examples of partially ionised plasma, while the interior of the sun, the solar corona and the stars are examples of fully ionised plasma, depending on the temperature and density of their environments [85]. Plasma TVs and plasma engraving are just two examples of the many contemporary technologies that take advantage of plasma's reaction to electromagnetic fields [86]. Plasma was first advocated by American physicist Irving Langmuir in 1922. He suggested that the electrons, ions and neutrals in an ionised gas should be thought of as corpuscular substance entrained in some kind of flowing medium [87].

It is commonly believed that 99 percent of the matter in the universe is in the plasma state, which can be described as taking the shape of an electrified atmosphere in which the atoms have been broken apart into positive ions and negative electrons, given that stars, their atmospheres, atmospheric nebulae and much of the interplanetary hydrogen are all plasmas. One comes into contact with the plasma that makes up the Van Allen radiation belts and the solar wind as soon as one departs the earth's atmosphere [86]. The Saha equation of ionization can be written as follows for any gas [88]:

$$n_i / n_n = 2.4 \times 10^{21}\, T^{3/2} / n_i\, e^{-U_i/KT} \quad \ldots\ldots\ldots (2\text{-}14)$$

Here T is the gas temperature in degrees Kelvin, ni is the ionised atomic density (in numbers per unit volume), n_n is the neutral atomic density, and K is Boltzmann's constant and U_i is the ionisation energy of the gas, which is the amount of ergs that are needed to extract the electron from the atomic shell that is furthest away from the nucleus [88]. The Saha equation can be written as follows for a vapour consisting of only a single chemical species [88]:

$$\frac{n_i + n_e}{2a} = \frac{2}{\lambda^3}\,\frac{g_{i+1}}{g_i}\exp -\left[\frac{(\epsilon_{i+1} - \epsilon_i)}{k_B\,T}\right] \ldots \ldots (2\text{-}15)$$

where n_i represents the number of atoms in the i- ionisation state (that is, with i electrons removed), i represents the degeneracy of states for the i-ions, creating an *i*-level ion and *ne* is the electron density, λ is the thermal de Broglie wavelength of an electron [88].

$$\lambda = \sqrt{\frac{h^2}{2\pi\, m_e\, k_B\, T}} \quad \ldots\ldots\ldots\ldots \qquad (2\text{-}16)$$

Where me represents the mass of an electron, T represents the temperature of the atmosphere and h represents Planck's Constant [89].

2.12 Plasma Classification According to Particle Temperature

Plasma can be classified according to temperature into hot plasma and cold plasma:

2.12.1 Hot Plasma (Thermal)

Thermal equilibrium occurs between gas molecules (electrons and molecules) due to repeated collisions between them when discharging high-pressure gas, which means $T_e \cong T_i \cong T_g \cong (10^4\text{-}10^5)$ K [90].

2.12.2 Cold Plasma

Non-thermal equilibrium occurs between the energy of the gas molecules(electrons and molecules) so we will have high-energy electrons and low-energy molecules, which means $T_e >> T_i >> T_g$ where, T_e, T_i and T_g are the temperatures of the electron, ion and gas molecules respectively. They are used in thin film processing and applications medical [90]. By sending a process gas through an electric field at atmospheric pressure, cold plasma can be generated. Because the temperature in the plasma generator is maintained at or near ambient temperature, these plasmas are referred to as “cold” [91]. There is another classification beside of plasma temperature which is plasma density, where is the proportion of what level of gas particles have ionized; all the more especially it is the proportion of what number of free electrons there are per unit volume. As per this rate we will have:

-High Density such as space plasmas, (density range exceeds 1026 m^{-3}).

-Medium Density such as majority of artificial or lab plasmas, (density range between 1015-1025 m^{-3}).

-Low Density also can be observed in artificial or lab plasmas, (density range less than 1015.m^{-3}). Figure (2.17) shows relation between some natural and artificial plasma densities and temperatures [92].

2.13 Plasma Parameters

It's important to remember that in plasma physics, the term "parameter" typically denotes global plasma characteristics. Three primary factors must be considered [91]:

1. particles per unit volume (n) (measured in particles per cubic meter).
2. the species-specific temperature T (typically denoted in eV, where 1 eV=11605 (K).
3. the magnetic field B in its constant condition (measured in Tesla).

From these three foundational parameters, one can determine a large number of subsidiary parameters, such as the Debye length, the Larmor. radius, the plasma frequency, the cyclotron frequency and the thermal velocity In the case of plasmas that are only partially ionized, the fractional ionization and the neutrals' cross-sections are also very significant [89].

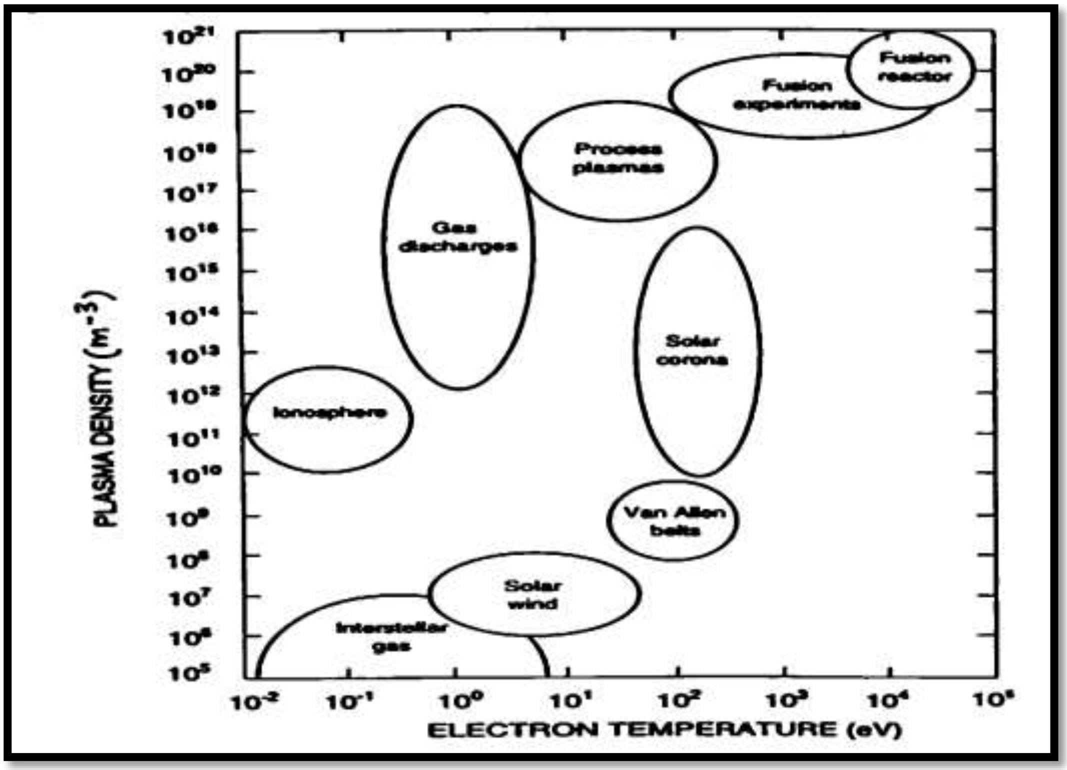

Figure (2.17): Relation between density and temperature for some natural and artificial plasma [92].

2.14 Plasma Production

Plasma is produced in many ways, and one of the well-known, it can produce by applying electric to the inert gas with using two electrodes. Plasma could generated when electron or more negative particles are separated from molecules or atoms under the appropriate pressure. The atom or molecule, which gives the electron, will become the positive ions [93]. In addition, in a laboratory could produce many types of plasma, for example, glow discharges, arcs fluorescent lamps, electrical sparks thermonuclear, arcs [94].

2.15 Plasma Diagnostics

The general goal of plasma diagnosis is to know the properties of plasma by observing experimental processes . important properties of the plasma that must be known is the electron temperature (T) and the electron density (ne). There are several ways to diagnose plasma, including [95]:

2.15.1 Langmore Probe

Langmore and colleagues (1923) used the electric probe to calculate the electron temperature (T) and electron numerical density (ne). The electric probe is a connector, one end of which is placed inside the plasma and the other end is connected to an electric circuit, the probe is made of high-temperature materials such as tungsten and platinum (Pt). There are two types of probes, single and double [95].

2.15.2 Emission Intensity of the Spectral Line

The plasma is diagnosed by knowing the intensity of the spectral line emission. When the electrons move from the lower energy level to the higher, electrons are excited and collisions occur, so the atom or molecule becomes excited as a spectrum is emitted from it and by analyzing the density of the emitted spectrum, we determine the temperature of the electrons (T) and the numerical density of the electron (n_e) [96].

2.15.3 Density Microwaves

Mmicrowave waves propagate in plasma when there is a change between the angular frequency of electron and the plasma frequency of electromagnetic waves, that the frequency of the waves is greater than the frequency of the plasma ($w_e > w_P$) and through the change in frequency we can determine the temperature of the electrons (T_e) and the number density of the electron (n_e) [97].

2.15.4 Invasive Probe Methods

- A ball-pen probe the sensor in the shape of a ball-pen brings the amplitude of the ion saturation current and the electron saturation current into equilibrium with one another. In this case, its floating potential becomes identical to the plasma potential[98]. The difference in potential between the ball-pen probe, which measures plasma and the Langmuir probe, which measures drifting potential is directly proportionate to the temperature of the electrons. This allows for the direct measurement of particle temperature at a high time precision and without the need for an external power source [99].

- A Faraday cup cup made of conductive metal that is used to collect charged particulates. The resulting current can be measured, and its value can be used to calculate the amount of protons or electrons that collide with the cup [100].

2.16 Low Pressure Discharge Plasmas:

In this section, it is one of the common artificial plasmas which is divided into two main techniques which can be observed :

2.16.1 DC Glow Discharge:

This fits into plasma that is not heating and is created by delivering a direct current (DC) electric between two surfaces known as the cathode and the electrode, and in order to generate plasma an inert gas (mostly) is applied which raise the ionization and stimulation of atoms and electrons caused by their inelastic collisions. Concentrations of new ions and electrons will be increased due to increasing of ionization collisions. This process occurs near cathode which means maintain plasma generation [101]. The electrons that were released from the conductors are typically unable to continue the discharge when there will be no potential difference among the electrodes; because of large flowing of the current; the constant potential difference increases the DC discharge. This can be widely used for for the actual process of surface change, including light source, engraving, and Ion-deposition [102].

2.16.2 Radio Frequency Glow Discharge:

It is either inductively or capacitively, producing plasma in either case coupling energy at less than the radio spectrum (3MHz to 300GHz) frequency. There are two different types of RF plasma discharges, the first of which is one in which an AC voltage source is used to energise electrodes all the way through a device capacitor. On the other hand, the other electrode is grounded tightly and that functions properly in capacitive coupled discharge (CCD) as well as inductively coupled discharge (ICD) [103]. Rapid charging of capacitor at the positive side of the voltage source, which results in a drop in voltage all throughout the plasma. For the purpose of material processing in the aerospace and microelectronics industries [104].

The circular spiral coil shape is standard in inductive coupled discharge, where electromagnetic induction is responsible for generating the appropriate electric current. The time-varying magnetic flow is produced by the passage of radio frequency current through the inductor, plasma discharge and unconstrained electron acceleration are maintained by the induced RF periodic electrical field [105]. This phenomenon is of great relevance, it is recommended to use it in deposition and the production of semiconductor devices, as well as for the purpose of manipulating the surfaces of diamond coatings and manufacturing, Figure(2-18) shows a sample of ICD and CCD systems [106].

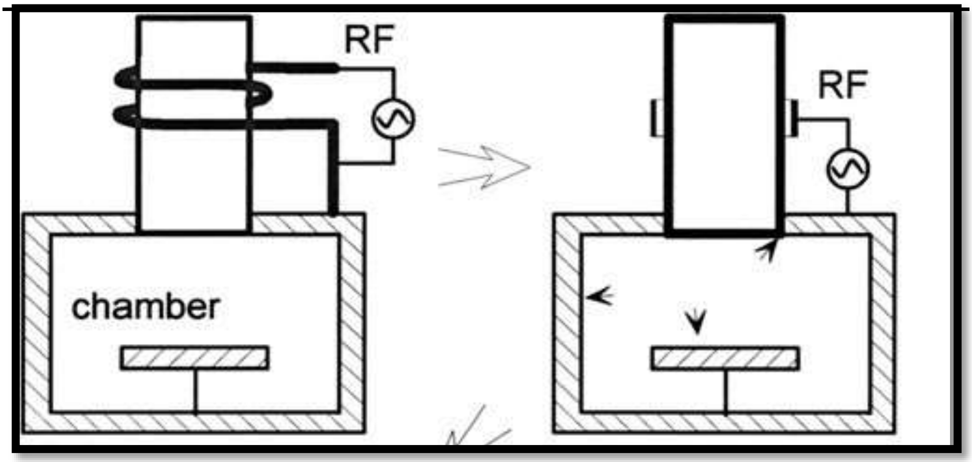

Figure (2.18) : Inductively and capacitive coupled discharge system [109].

2.17 RF Sputtering Technique:

2.17.1 Sputtering Description:

When a solid is attacked with high-energy plasma or gas particles, a process known as "sputtering" occurs in which tiny fragments of the solid are expelled from the surface. It is something that happens naturally in space, but it can be a source of damage that is undesirable in precision components[107]. It can be applied to a wide variety of spark ion sources, thin sheet coating, surface and surface layer analysis, surface cleansing [108].

2.17.2 Influenced Factors on Sputtering:

The main reason of sputtering is the interaction between incident particle with surface of the target; thus sputtering production for certain must be affected by incident particles energy, material of target, particles incident angles and target surface crystal structure [110].

2.17.3 Advantages of Sputtering Technique:

There are several advantages of sputtering techniques over other techniques[110]:

1. Low temperatures of substrate.
2. Films good adhesion.
3. High rates of deposition.
4. Stable and good controlling process.
5. Easy sputtering of various materials with various vapor pressures.
6. Cheap deposition process.
7. Large areas scalability.

2.17.4 RF Magnetron Sputtering:

In sputtering, also known as cathode sputtering, positive ions strike a target, causing the surface atoms to discharge. Depositions that happened when the ejected atoms are concentrated on a substrate to prepare a thin film. Some improvements have been made by scientist Penning who discovered magnetic sputtering [109]. The magnetron sputtering system basic principle is backing planar cathode is by permanent magnets that give a toroidal field to form closed path throughout field lines over the target (cathode) surface. Magnetron sputtering will be functional at lower pressures and target voltages due to confinement and resultant intense plasma comparing with RF diode sputtering, where depositions rates are higher and deposited layer are larger, with possibility of abroad scale of applications due to low substrate heating [109].

2.18 Applications of Plasma

A lot of researchers are focusing their attention on the creation of manufactured plasma and the potential benefits that it could have for humankind.

These benefits could come in a variety of forms, such as in the disciplines of electrical engineering, automotive engineering, chemical engineering, and medicinal. Among these applications are the joining of copper, the processing of semiconductors, the treatment of surfaces.The following is a list of some of the applications that plasma can have:

a)Non-fusion terrestrial plasmas: Neon signs, florescent lights, processing plasmas, welder arcs and lightning are all examples of earthly plasmas and they all have electron temperatures of a few eV and ion temperatures, often at room temperature. Plasmas classified as "everyday" are typically devoid of an externally applied steady-state magnetic field and do not generate substantial levels of their own magnetic fields. Weakly ionised and driven by collisional and radiation processes [111].

b) Living Tissues Treatment: The treatment of living tissue necessitates certain characteristics for the devices that are used to administer cool plasma, such as the following: a). Lessening of disruptive processes on biological things. b) Ensuring that only the distressed cells are affected. c) Trying to avoid the effect of the heat. d) The restriction of the length of time that treatment is administered in order to avoid the utilisation of potentially toxic effects in the process of treating cells [112].

c) Benefits of Plasma Processing: The positive impacts of processing help to mitigate the negative consequences of industrialization[113]. Thus, significant progress towards mitigating climate change and lowering carbon dioxide pollution can be expected from widespread use of plasma-processing techniques; to reductions in pollution and other environmental contaminants, as well as to improvements in the effectiveness of the utilisation of energy [114].

d) Plasma Surface Treatment: The term "plasma surface treatment" refers to the process of modifying the surface properties of solid materials by using the majority of the active species generated by a plasma. It could entail molecular interactions with the surface, resulting in an increase or decrease in surface charge or the number of absorbed monolayers; In addition to this, it has the potential to alter the material's superficial monolayers' physicochemical states[115]. Alterations to surface properties can also be used to categorise plasma surface treatments. Cleaning, boosting surface energy, removing contaminants and sterilising are all examples of the impacts that changes in surface properties [111].

e)Plasma Ion Implantation and Deposition: The target is utilised as a component of the beam generating system in plasma-based ion implantation. These techniques generate and make use of streams of ions, by using a three-dimensionally structured target (substrate)[116]. The surface of the biassed target that was created around the ion acceleration that took place in a dynamic, self-adjusting envelope, to reducing wear and rust through the creation of hard, robust, low-friction and chemically neutral phases [117].

f) Cutting by Plasma: Plasma shear or plasma cutting machine is a machine that cuts steel and other materials with a plasma. Plasma shears emit an electric arc through a gas that passes through a specific orifice. Gas such as nitrogen, argon, oxygen, and others. The gas's temperature increases as a result, pushing it into its fourth phase of existence, the plasma example. The particular opening, known as the nozzle, through which the gas travels causes it to travel at a high velocity[107].

g)Electro-thermal and electromagnetic Plasma for surface treatment: These launchers generate plasma that is extremely heated and dense, has a brief wavelength, and moves at a high velocity. This plasma can directly influence the surface of a substance, Therefore, it is used immediately for covering purposes, in which one material's traits are superimposed on another material to bring out the best in both. Such interface the application to metallic surfaces results in the formation of an exceptionally solid metallic surface that has a very high propensity to withstand corrosion [118].

2.19 Radio Waves:

Radio waves are a form of electromagnetic radiation that generally have frequencies of 300 gigahertz (GHZ) or lower. Radio waves have the greatest wavelengths of any sort of electromagnetic radiation in the electromagnetic spectrum. Radio waves travel at a speed that is very close to the speed of light in the earth's atmosphere. Charged particles that experience acceleration, such as those caused by time-varying electric currents, are what give rise to radio waves. Figure (2.19) [119].

2.20 Applications of Radio Waves:

As a result of the quick development of wireless communication technologies, our environment is rife with radio frequency (RF) electromagnetic radiation. These technologies have many applications, such as the base stations of mobile communication networks and wireless internet terminals.

Some of the key applications can be listed as [120]:

1. Wireless communications: such as, cellular phones, satellites, etc.
2. Radar: such as airborne, marine, vehicle, weather, traffic control, weapon guidance.

4. Remote sensors: such as weather monitoring, water, clouds, flood, snow.

5. Medical : such as MRI.

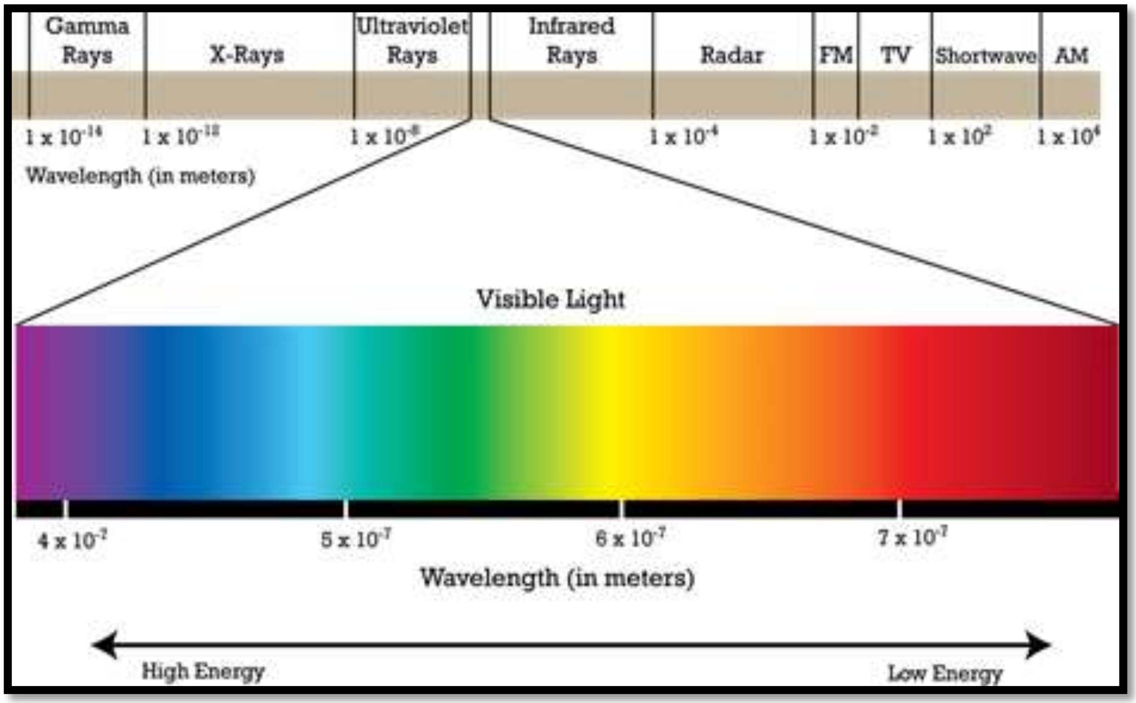

Figure (2.19): Electromagnetic spectrum [119].

Chapter Three

Methodology and Instruments

3.1 Introduction

The main objective of this chapter is to present the experimental method used in this study to prepare of two types of spinel ferrites that carry the general formula where M= (Cd, Cu) at values of sample x = (0.0, 0.2, 0.4, 0.6, 0.8 and1) using sol-gel auto combustion method. The chapter also explains the use of a system RF magnetron sputtering system its design, overview of the system, its technical parameters, its composition, and technical specifications of magnetron target, RF power supply through which the prepared samples are exposed to the plasma and the changes that stimulate the test.

Also, this chapter includes the equipment and materials needed in the research, structural, microwave and magnetic measurements are made through which the results are reached, and explain the most important methods used to produce nanomaterial. Where different programs are used, using the personal computer(pc). Figure(3.1) the steps that are performed.

3.2 Raw Materials Used for the Sol-Gel Method

In this work, the raw materials are chosen with high purity, as the increase in purity is reflected in the materials that will be to obtain, which in turn are reflected on the properties of the materials prepared with quality. As shown in Table (3.1).

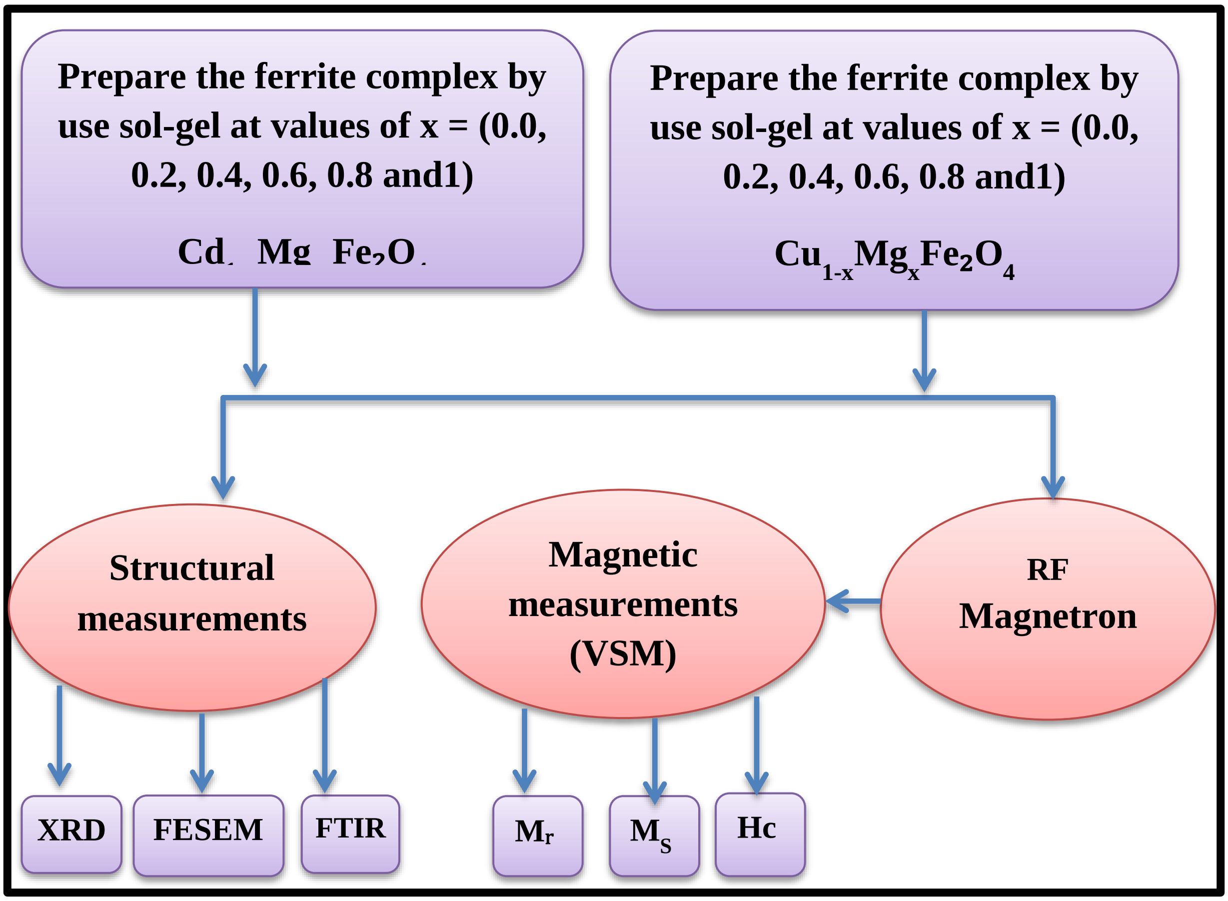

Figure (3.1): Main steps of the experimental work.

3.3 Preparation of the Samples

3.3.1 Calculation Molar Masses of raw materials

The masses are calculate as the primary mass, where the proportions of the components of one mole are determined in terms of the atomic weights for each element and according to the relationship:

$$n = \frac{W}{W_m} \quad \dots\dots\dots \text{(3-1)}$$

where:

(n) :Number of moles.

(W): Weight to be calculated to preparation of the samples.

(Wm) : Molecular weight.

the rest of the materials whose values are shown in Table (3.1).

Table (3.1): The purity of the used raw materials

Chemical formula	Molar weight. g.mol^{-1}	Country	Purity
$Cd(NO_3)_2.4H_2O$	308.47	India	99%
$Cu(NO_3)_2.3H_2O$	241.60	India	95%
$Mg(No_3)_2.6H_2O$	256.41	England	99%
$Fe(NO_3)_2.9H_2O$	404	India	98%
$C_6H_8O_7$	192.12	United Kingdom	99%
NH_3	35.05	India	98 %

3.3.2 Calculating Reactive Material Masses

The reactive equation is used to calculate molar masses of the reactants for the production of a ferritic compound $M_{1-X}\,Mg_XFe_2O_4$, where M = (Cd, Cu) at value of x= (0, 0.2, 0.4, 0.6, 0.8 and1), (x) represents different ratios of weights. Tables (3.2) and (3.3) show the weights used in preparing ferrite compounds. This process can be represented by the following equation:

$$_{(X)}Mg(NO_3)_2.6H_2O + _{(1-X)}Cd(NO_3)_2.4H_2O + 2Fe(NO_3)_2.9H_2O + C_6H_8O_7$$

$$\longrightarrow Cd_{1-x}\,Mg_xFe_2O_4 + 4N_2 + 6CO_2 + 22H_2O + 10.5O_2 + 10H_2$$

$$_{(X)}Mg(NO_3)_2.6H_2O + _{(1-X)}Cu(NO_3)_2.3H_2O + 2Fe(NO_3)_2.9H_2O + C_6H_8O_7$$

$$\longrightarrow Cu_{1-x}\,Mg_xFe_2O_4 + 4N_2 + 6CO_2 + 22H_2O + 10O_2 + 9H_2$$

Table (3.2): The weights used in the preparatory work of the composite $Cd_{1-x}Mg_xFe_2O_4$.

No. of mole	$Fe(NO_3)_2.9H_2O$	$Mg(No_3)_2.6H_2O$	$C_6H_8O_7$	X	1-X	$2Fe(NO_3)_2.9H_2O$	$Cd(NO_3)_2.4H_2O$
1	404.0	256.41	192.12			808	308.47
0.1	404	25.641	19.212			808	30.847
	40.4	0		0	1	80.8	30.847
		5.128		0.2	0.8		24.677
		10.256		0.4	0.6		18.508
		15.384		0.6	0.4		12.338
		20.512		0.8	0.2		6.169
		25.641		1	0		0

Table (3.3): The weights used in the preparatory work of the composite $Cu_{1-x}Mg_xFe_2O_4$.

No. of mole	$Fe(NO_3)_3.9H_2O$	$Mg(No_3)_2.6H_2O$	$C_6H_8O_7$	X	1-X	$2Fe(NO)_3.9H_2O$	$Cu(NO_3)_2.3H_2O$
1	404.0	256.41	192.12			808	241.60
0.1	404	25.641	19.212			808	24.160
	40.4	0		0	1	80.8	24.160
		5.128		0.2	0.8		19.328
		10.256		0.4	0.6		14.446
		15.384		0.6	0.4		9.664
		20.512		0.8	0.2		4.832
		25.641		1	0		0

3.4 Preparation Steps for the Automatic Combustion Sol-Gel Method.

The sol- gel technique method is used here for preparation of hematite M_{1-X} Mg_X Fe_2O_4 where M = (Cd ,Cu) with different values x= (0, 0.2, 0.4, 0.6, 0.8 and1), with magnesium ferrite nanoparticles to produce nano composite.

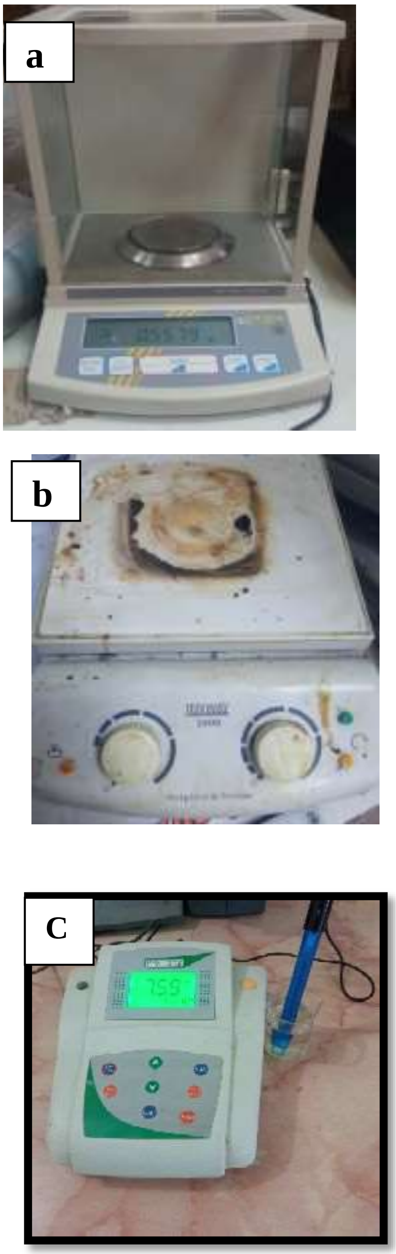

Figure (3.2):a, b and c Measurement used instruments.

1- The material is weighed as shown in the Tables above in a highly sensitive electronic balance (HR-2000) with high accuracy $(10^{-4}g)$ located in the College of Science - University of Babylon advanced thin film laboratory, as shown in Figure (3.2a). The materials were put in a heat-resisting baker size (500) mL, then add distilled water free of ions to the size of (300)mL and put the solution on a magnetic mixer (magnetic stirring) type (JENWAY-1000), as shown in Figure (3.2b) to obtain a homogeneous solution (complete melting of raw materials) and reach the temperature of the solution at 60˚C.

2- In the sol-gel process, the conversion of sol to gel is usually done by changing the pH or changing the concentration of the solution by add ammonia is added to the solution to change the PH of the solution to be (PH>7). This is confirmed by using a PH-meter type (HI-2211), as shown in Figure (3.2c). Then it will rise temperature is gradually to 60 °C for two hours.

3- The temperature is increased to 70 °C, we keep it at this temperature for 20 minutes, then temperature we will gradually raises to 80 °C and for three hours to obtain a thick-density solution, at this temperature the solution begins to gradually shift to gel.

4- Raises the temperature to 90 °C for 15 minutes, then raises the temperature again to 100 °C for the same previous time and also raises temperature again to 110 °C where the gel begins to turn into a dry gel where the top surface of the gel is a coherent surface. as shown in Figure (3.3a)

5- After the temperature reach to more than 120°C, the dry gel begins to self-combustion, when the combustion is complete, a strong glow appears with rising fumes its shape is loose structure, fluffy, and when touched it falls and then leaves to cool and grind in a ceramic mortar for 6 hours to get the powder in the flour as shown in Figure (3.3b,c).

6- Then it is re-grinded with an electric grinder available in the market for an hour and then re-grinded by hand until we reach a nanomaterial and homogeneous cationic distribution in spinel crystals.

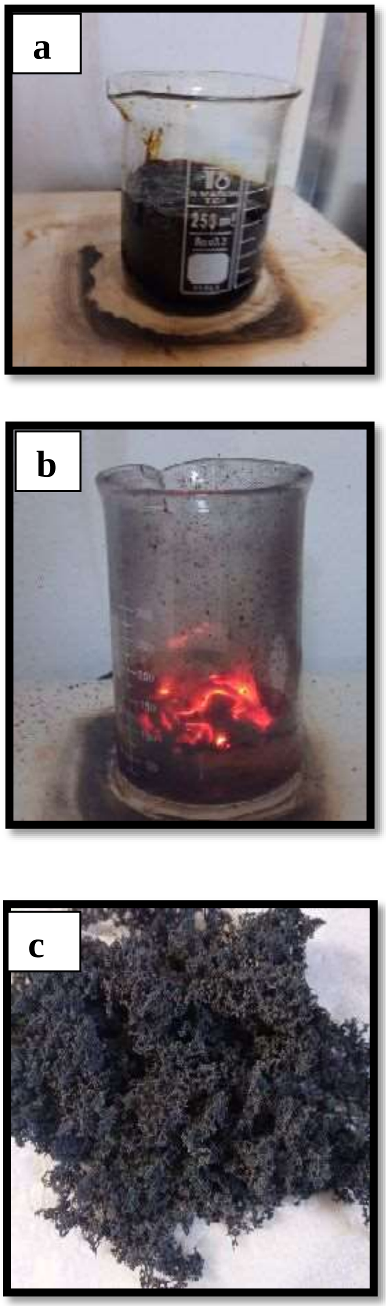

Figure (3.3):a, b and c Burning ferrite.

7- It is brought back to the convection oven at a temperature of 1100 °C for 2 hours, known as sintering and then left inside the oven to cool for 24 hours and milling process is repeated so that the result is homogeneous.

8- Powder then mixed with glycerin material 6% wt. Then the powder was pressed by a hydraulic press at a pressure of 150 kN within two minutes shape as a disc with a diameter of 20mm, where the molds were used according to the intended purpose as shown in Figure (3.4).

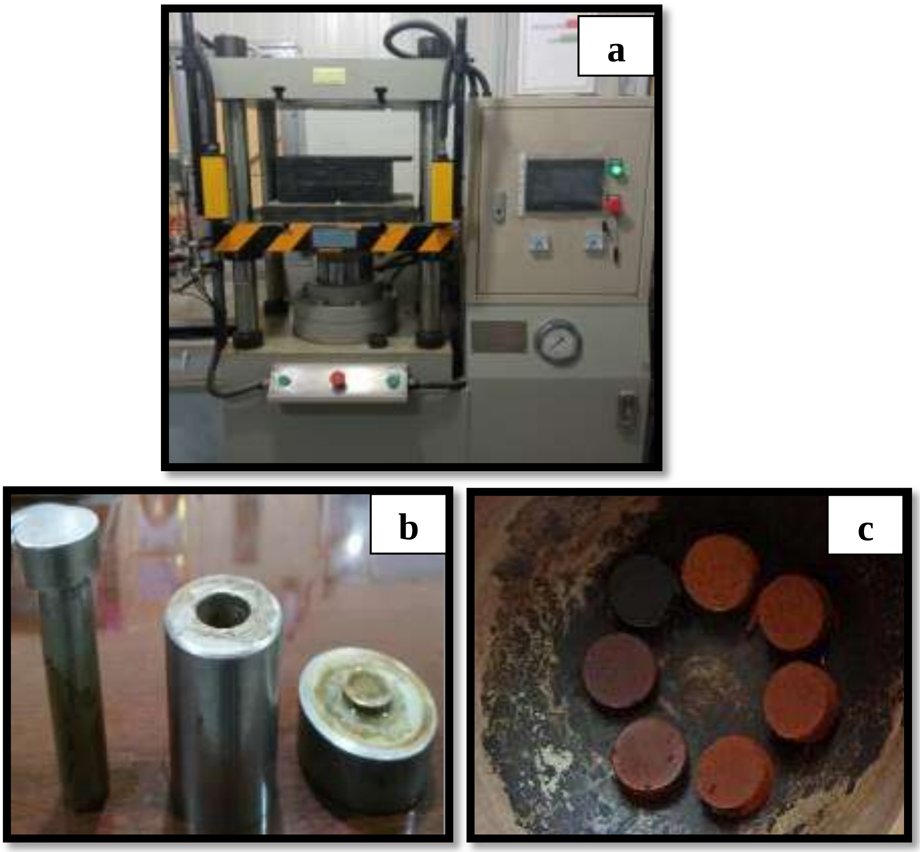

Figure (3.4): a:Hydraulic press, b: Molds used in the formation of ferrite, c: Samples.

After compressing the models, we display them to the plasma using the RF system, in the advanced plasma laboratory in the Physics Department of the College of Education, Al-Qadisiyah University. It took two hours to expose each sample inside the system. The main steps for preparing the ferrite complex shown in Figure (3.5).

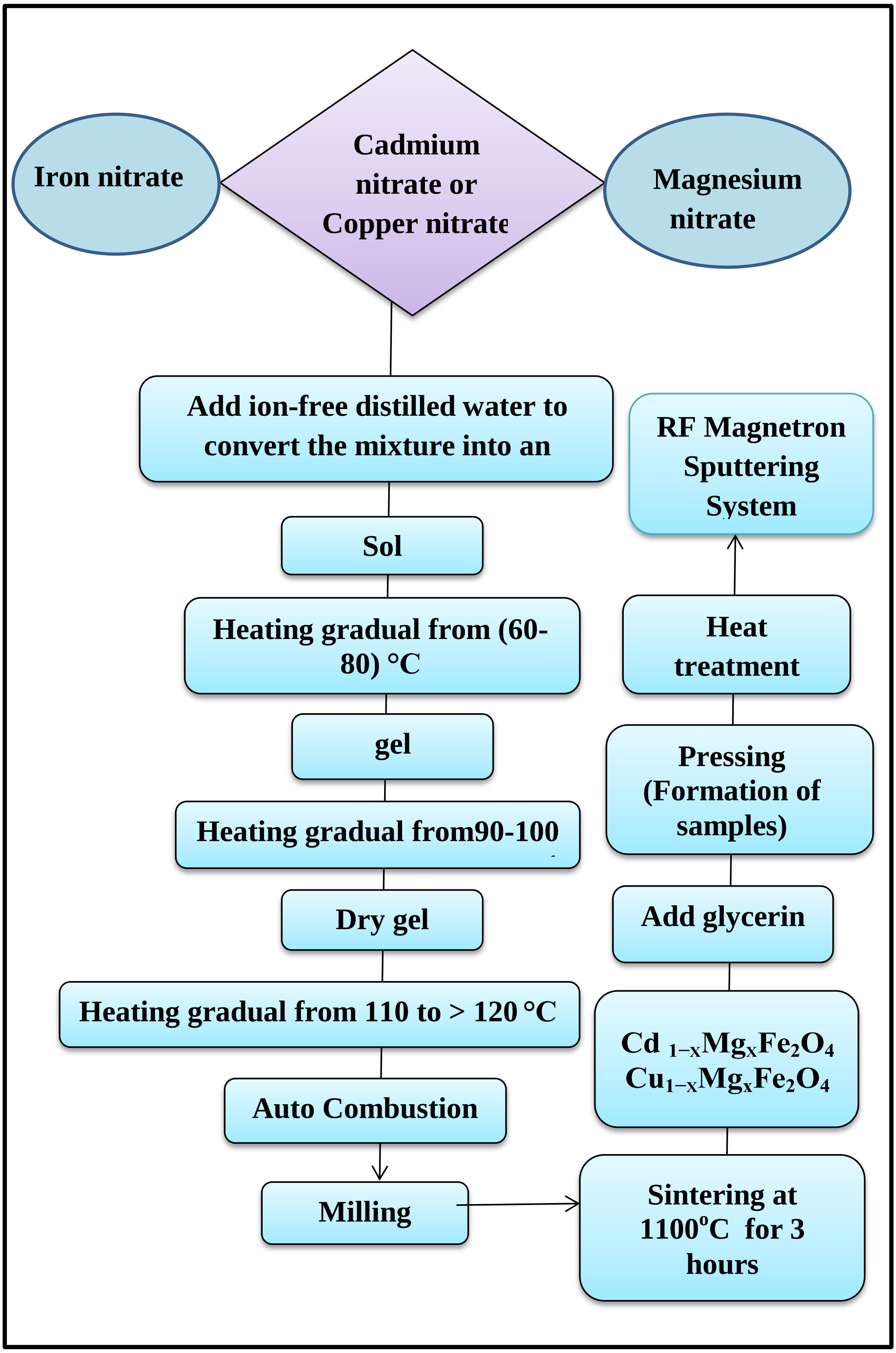

Figure(3.5): Shows the main steps for preparing the ferrite complex.

3.5 Devices Used in Ferrite Characterization

They are devices used to obtain structural, microwave and magnetic measurements and include:

3.5.1 Fourier Transmission Infrared Spectrum Technology (FTIR)

Infrared spectroscopy takes advantage by recording a fingerprint of a sample with absorption peaks which correspond to the frequencies of vibrations between the bonds of the atoms making up the material. The compounds on where the measurement process is done inorganic laboratory in the department of chemistry - college of science-University of Babylon and the device is of type (ALPHA-BRUKER), Figure (3.6) shows the FTIR device used for the examination.

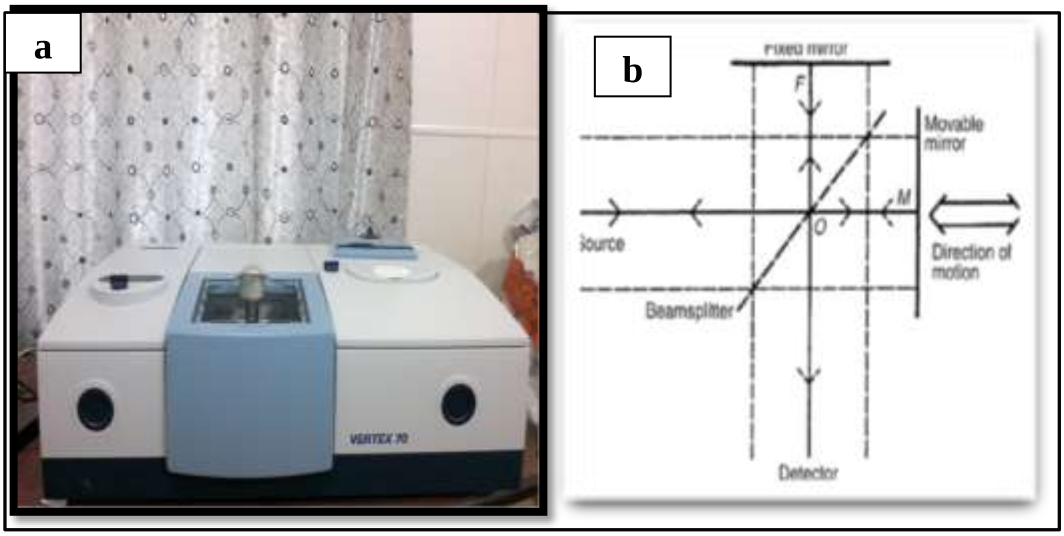

Figure (3.6): (a) FTIR device used for examination. (b) Schematic diagram of the FTIR components.

3.5.2 X-Ray Diffraction (XRD)

Using the XRD device, the crystal structure and synthetic information of the prepared ferrite were verified **(X' Pert PW 3040/60)**, it is found in (Par-e-Tavous Research Institute- Mashad - IRAN) is shown in Figure (3.7), which carries the specifications in Table (3.4).

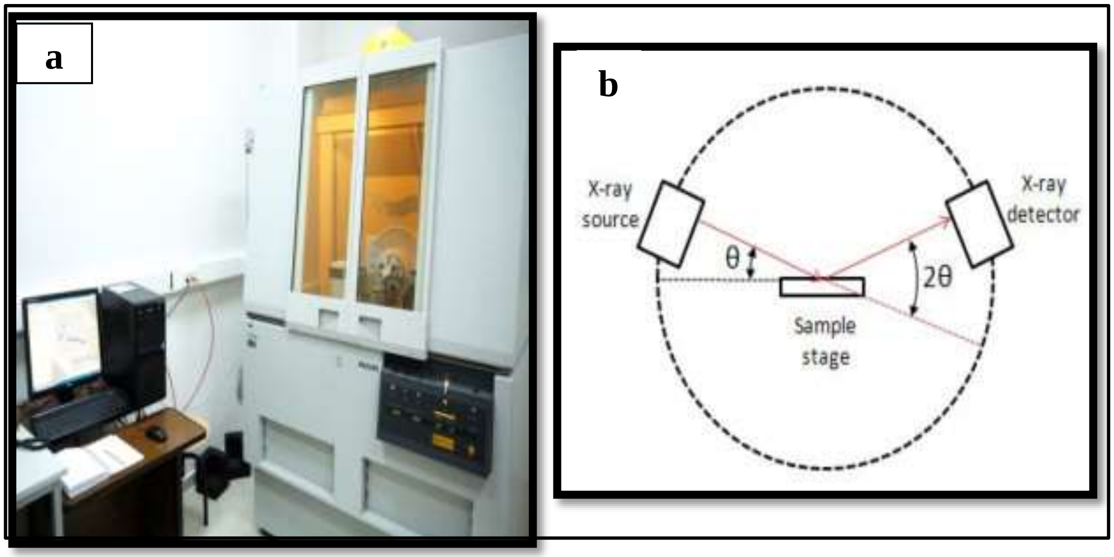

Figure (3.7): a)X-ray diffraction system, (b) Schematic diagram of an X-ray diffraction experiment.

Table (3.4): XRD device specifications

Current	**30 mA**
Voltage	**40 Kv**
Wave length	**1.54056 Å**
Range of angles (2θ)	**º10-º80**
Target	**Cu-K** α

3.5.3 Field Emission Scanning Electron Microscope(FESEM)

The scanning electron microscope (FESEM) provides topographic information for the scanned samples at magnifications of 10x to 300,000x, with virtually unlimited depth of field, which gives information about the surface formation and topography. The examination was conducted at the University of Tehran - Iran and the device is of type (TESCAN MIRA3) shown in Figure (3.8).

Figure (3.8): a) Shows Field Emission Scanning Electron Microscope (FESEM), (b) Schematic diagram of FE-SEM.

3.5.4 Vibrating Sample Magnetometer (VSM)

The(VSM) device is used to measure the magnetic hysteresis loop of the sample to be measured and assign magnetic properties. The magnetic properties are measured at the Spadana Institute of Materials Science in Isfahan-Iran by using a device (Model 7400 VSM USA) shown in Figure (3.9) where the applied field strength ranged between ±15000Oe at room temperature.

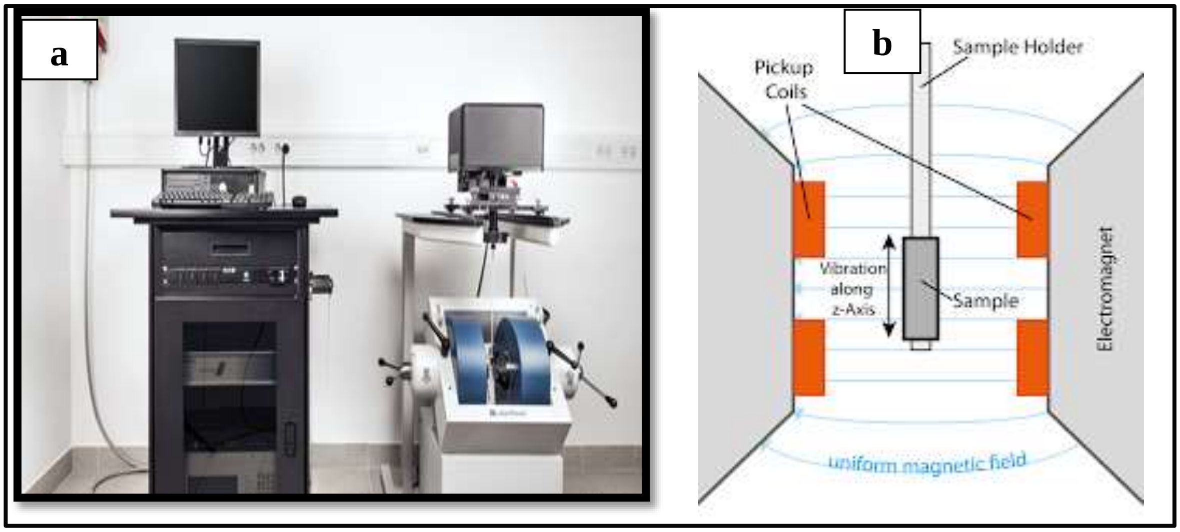

Figure (3.9):a) VSM device (b) Schematic diagram of the VSM components, (b) Schematic diagram of the VSM components.

3.6 RF Magnetron Sputtering System:

3.6.1 The RF Magnetron Sputtering System:

Figure (3-10) illustrates the of RF magnetron sputtering system, as the sputtering system consists of three main parts; chamber, RF power supply and vacuum system. The RF magnetron sputtering system is a three-target magnetron targets. In order to facilitate the experimental operation, the coating machine is also equipped with an electric baffle, which can directly control the opening and closing of the baffle through the screen.

The coating machine is equipped with a maximum 150w or 200W RF power supply, by manually switching the output lines, it is possible to share one power supply (not simultaneous) with the three targets, thereby enabling operation of plating multiple or multiple layers of membranes in a single experiment, also the targets are connected to water chiller to keep the targets cooled Table (3.5) technical parameters of magnetron sputtering system.

The second part is the control box which contains a touch screen to control starting of system, flowing of gas, sample rotation speed and stage temperature setting, in addition to inlet gas and air switch. As shown in Figure (3-11).The third part is the RF power supply, device is compact and well designed and can be placed on the desktop, making it ideal for lab usage. The upper surface of the chamber is as shown in Figure (3-12), mainly for the upper structure of the magnetron target, with water-cooled pipe joint.

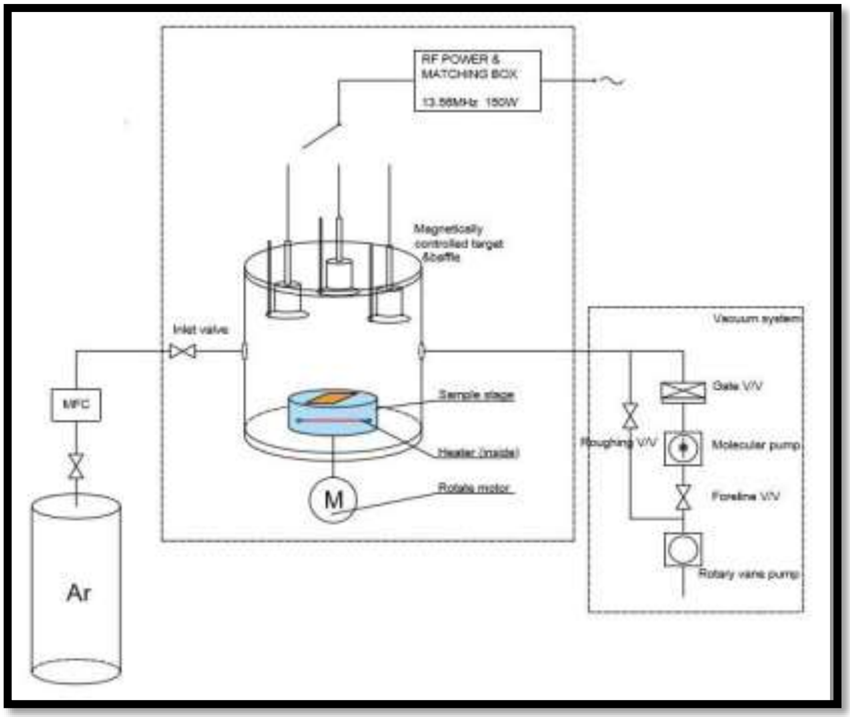

Figure (3.10): Schematic diagram of sputtering system.

Table(3.5): Technical Parameters of Magnetron Sputtering System.

Input voltage , Frequency	AC220V, 50HZ
Max. RF power supply	200W continuously adjustable
Cavity Material (Chamber)	Stainless steel
Cavity Size	300mm × 300mm
Magnetron sputtering heads	3 heads
Magnetron target parameter	Tilt angle 0-25°,the distance from the target to the sample stage is 50-80 mm
Sample stage parameter	Size 185mm, speed 1-10 pm adjustable, heating up to 500℃ temperature control accuracy ±1℃.

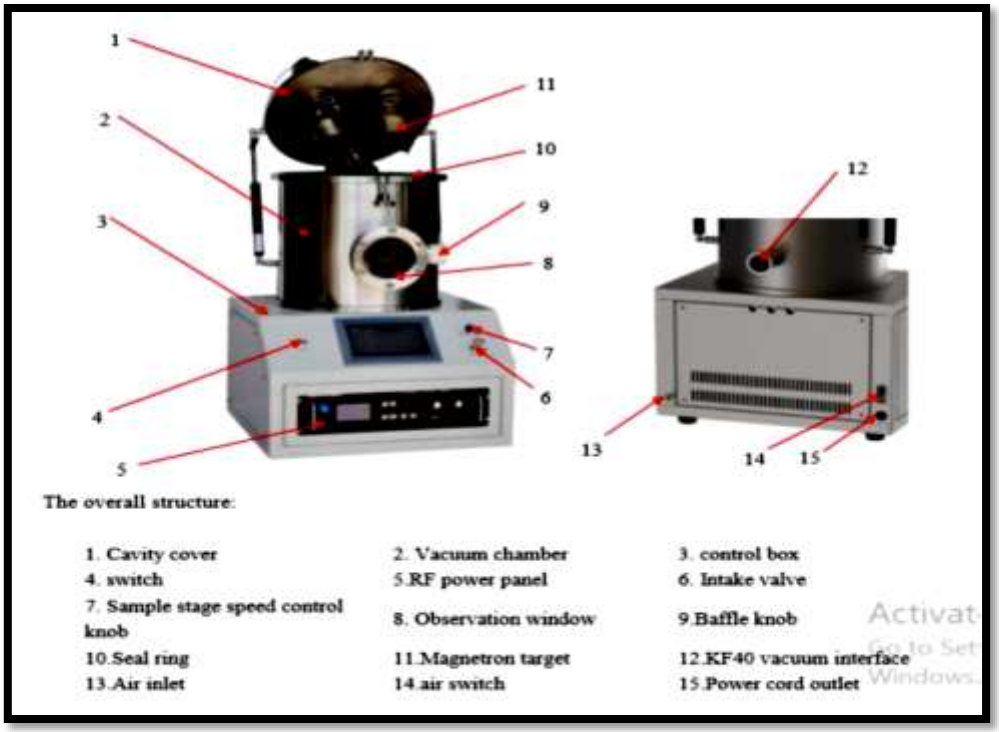

Figure (3.11): Composition of RF magnetron sputtering system.

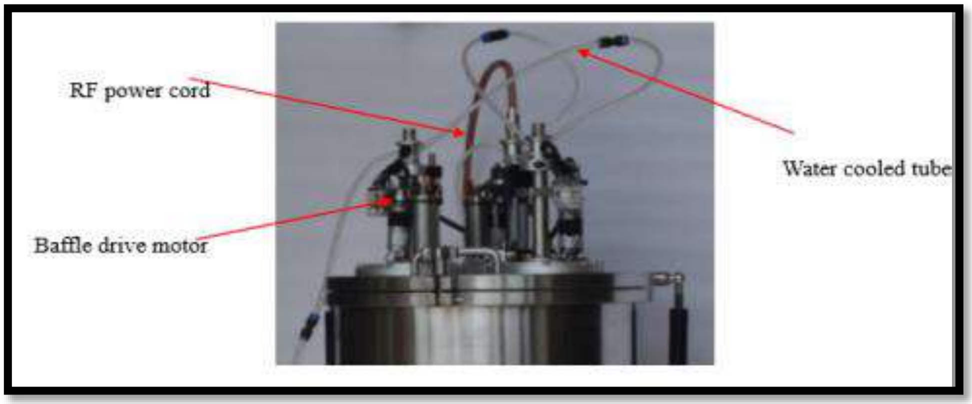

Figure (3.12): Upper surface of RF magnetron sputtering system.

3.6.2 Technical Specifications of Magnetron Target:

The magnetron target of this system is tabulated in Table (3-6) and shown in Figure (3-13):

Table (3.6): Technical specifications of magnetron target

Shell material	Stainless steel
Target head material	Red copper
Magnetron Head dia. Size	2 Inches
Maximum Withstand Power	500W.
Available Power Supply	RF/DC.
Cooling Mode	Water Cooling

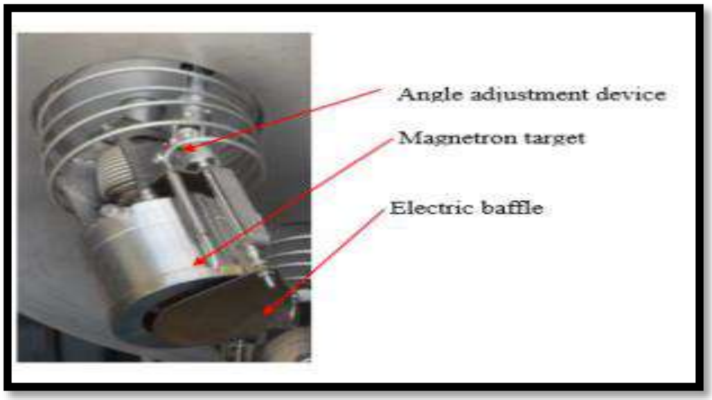

Figure(3.13): Inside structure of single magnetron target.

3.6.3 Specifications of Vacuum System

The two stages rotary vacuum that used in this with the specifications listed in Table (3-7):

Table (3.7): Specifications of vacuum system.

Power	0.4 KW
Voltage	AC 220V
Frequency	50 HZ
Current	2.5 A
Rotation Speed	1440rpm
Speed of Vacuum	4 $m^3.h^{-1}$
Maximum Vacuum Pressure	$5*10^{-2}$ pa

3.6.4 Waterway Installation

The magnetron sputtering head of this system is cooled by water cooling machine for cooling with capacity of 10 L./min. This machine is connected with two water pipes which used to the inlet and the outlet of water cooling as shown in Figures (3.14) and (3.15).

Figure (3.14): Water chiller to cool magnetron targets.

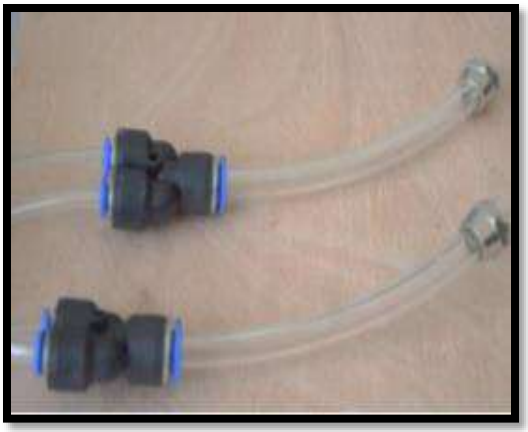

Figure (3.15): Reserved water pipes.

3.6.5 RF Power Supply:

The sputtering coater has equipped with RF power supply with 200 Watt maximum power, the operation panel contains switch for power on and off, display to show the applied and reflected power values, buttons to control digital menu of power supply options and power adjustment control. It is important to mention that best plasma generation might result at zero reflected power.

3.7 Operation of Sputtering System

In this work, two models of ferrite are prepared using a sol-gel method, and the models are pressed into circular discs with a diameter of 20 mm, then we continue the work as follows::

1. The clean substrate is placed on the sample stage in the center of the chamber. At this point we use CuO the case of the compound ($Cd_{1-x}Mg_xFe_2O_4$), and we use the target ZnO when placing the compound ($Cu_{1-x}Mg_xFe_2O_4$).
2. Clean the brass target as well as the inner chamber from the remnants of previous runs.
3. Close the chamber lid and operate the door knob judiciously until it is tightened securely.
4. Starting the rotary vacuum to evacuated the chamber of this system.
5. Turning on the pressure gauge to measure the gas pressure in the chamber.
6. Setting the desirable heating degree .
7. Filling the chamber with gas.
8. Turning on the water chiller to cool the targets.
9. Turn on RF supply, loading the wanted power, reducing the reflected power until reached zero to generate most effective plasma.
10. After reaching the pressure value 7×10^{-2} mbar, the device was turned on.
11. Set the temperature up to 523 K.
12. The chamber was filled with argon gas (purity 99.99%), the pressure reached 4.5×10^{-2} mbar.
13. RF source turned on, power load up to 150W, reducing reflected power until it reaches zero for most efficient plasma generation.
14. At this point the deposit process started, and the deposit time lasted 2 hours.
15. Experiment run is terminated, the device is turned off and cooled to room temperature.

Chapter Four

Results and Discussion

4.1 Introduction

In this chapter, I will discuss the obtain results and the examinations of samples that prepared using various devices and techniques that helped saved the effort the time for identification the nature of the stacking system, the type of crystal levels and trends in interpreting the results associated with the properties according to the conditions of preparation. I well discussing the magnetic properties of the prepared materials, and the possibility of classification and its uses depend on the properties of the desired application, as well as clarifying the extent of the effect of the samples prepared for the plasma the RF system on the properties that have been studied.

I will handle the results and examinations in two stages, the first stage before exposure to plasma and the second after exposure to plasma.

4.2 Structural Properties

4.2.1 X-ray diffraction (XRD)

X-ray crystallography is a method of knowing the arrangement of atoms within crystals and provide information on the crystal structure of solid materials such as the predominant direction of crystal growth and crystal structure, as well as calculating the average granular size of the crystal, crystal grid constants and crystal phases. The X-ray diffraction diagram is important for diagnosing the material by comparing the results of the prepared material with the International Center of Diffraction Data (ICDD).

The XRD test of $Cd_{1-X}Mg_XFe_2O_4$ ferrite prepared by sol-gel method is carry out at room temperature after sintering at 1100 °C and the final firing process followed by grinding the ceramic slurry of the agglomerates from the generation process and converting them into a homogeneous nanomaterial that ensures obtaining the ferrite spinel phase. It is found that the pure $MgFe_2O_4$ ferrite compound contaminated with manganese ion in different proportions is polycrystalline and in the preferred orientation (222) and conforms to the tag (No. 96-591-0006).

As shown in Figures (4.1a, b) shows the face-centered cubic spinel phase (FCC) and all the samples that are prepared without the presence of impurities or secondary phases. The height of the peak increases when the cadmium ion is replaced by the magnesium ion, with an increase in the concentration of magnesium and there is a shift to the right, towards $CdFe_2O_4$ and we also notice an increase in intensity with an increase in concentration, then it returns by decreasing at x = 1, that is, when replacing the cadmium ion with the magnesium ion, Figure (4.1f).

The prevailing trend of crystal growth (222) the width of the peak increases and decreases depending on the concentration, which decreases with decreasing intensity of cadmium ion and that there is a slight shift to the right in the cadmium ferrite, which indicates a decrease in the crystalline frit of cadmium and this decrease is due to saturation of the activity level [121]. However, as the concentration of magnesium increases, the effect of the cadmium ion, which has a larger ionic diameter decreases .The $CdFe_2O_4$ ferrite compound is larger than the compound $MgFe_2O_4$ because the ionic diameter of cadmium is greater , that is the increase in the interface distance of the d_{hkl} surfaces, than that of magnesium this appears when Cd=0

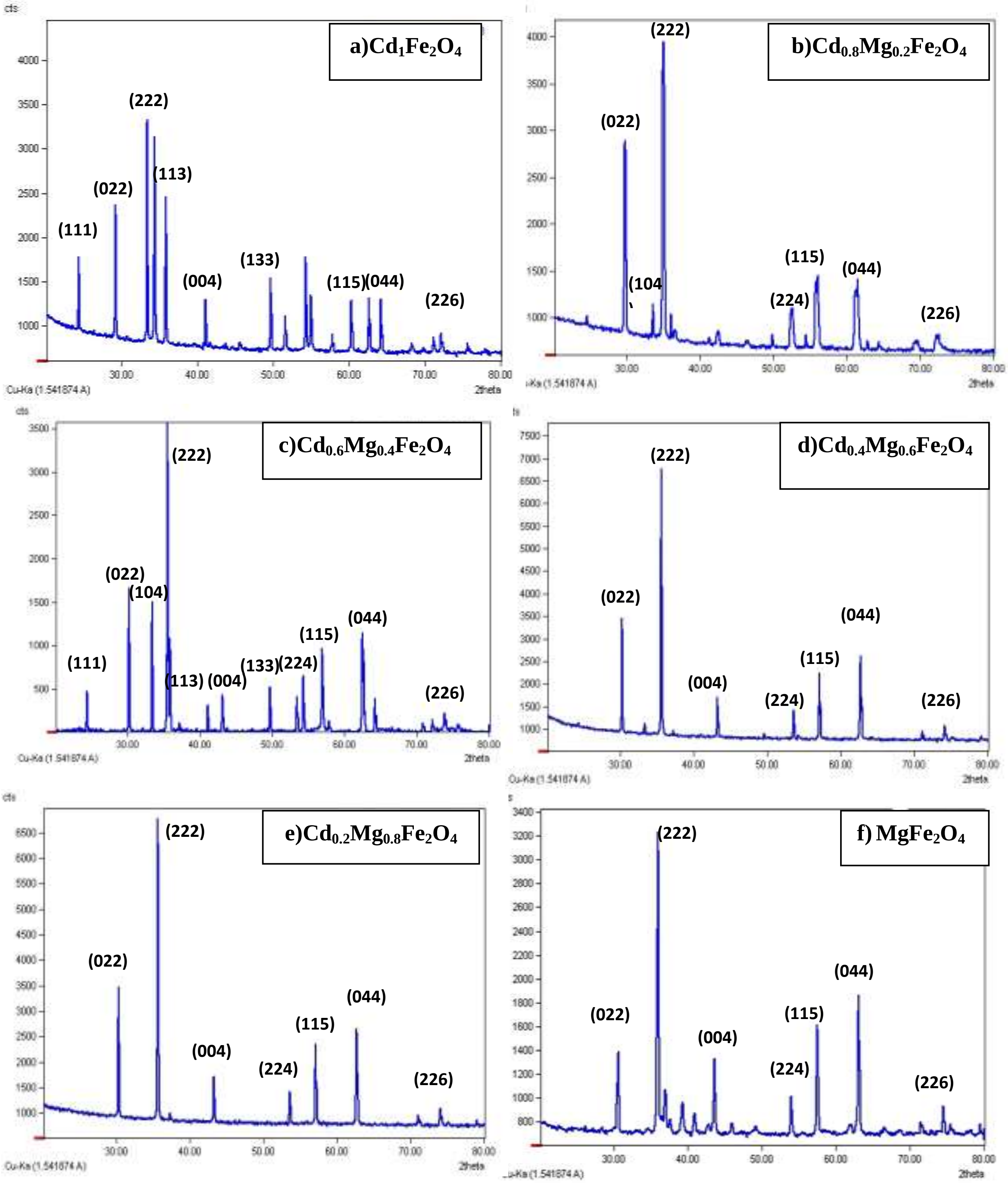

Figure (4.1): X-Ray patterns of $Cd_{1-X}Mg_X Fe_2O_4$ with a)x=0, b)x=0.2, c)x=0.4, d)x=0.6, e)x=0.8 and f)x=1 Mg before plasma exposure.

When conducting an XRD examination of the rest of the samples according to the ratio x = (0.2, 0.4, 0.6, 0.8) for the ferrite compound $Cd_{1-X}Mg_X Fe_2O_4$ as in Figure (4.1 c, d, e, f) where the interfacial distance of the incoming surfaces (d_{hkl}) is calculated and the constant of crystal (a), granular size (D) and intensity of eruptions at the highest peak (222) as shown in Table (4.1) using equations (2.8), (2.9), (2.11) and (2.12) respectively.

Note that the preferred direction for crystal growth is (222), as there is a displacement of the peaks to the right, as there is an increase in the width of the peaks when the ratio (x) of the cadmium ion, the crystalline size increases and the interface distance to the inner surfaces d_{hkl} increases at the highest peak due to the crystal size of the particles and since the cadmium ionic radius is greater than the ionic radius of magnesium and since cadmium occupies the tetrahedral sites and cannot occupy octahedral sites surfacesits presence at this site leads to an increase in the size of the particles, but the rate of the nanoparticles decreases with the replacement of cadmium ions (Cd^{+2}) with (Mg^{+2})ions in the crystal lattice [123].

XRD shows the individual spinel phase of all samples examined before and after plasma exposure, Figure (4.2) after exposure shows that for the majority, the intensity of the peaks decreased after plasma exposure, at x=0 some peaks also disappear as we move to the right, especially peaks (111),(113) and (133).

Also at x=0.2 after exposure shows the intensity of the peaks decreased after plasma exposure. In addition, the peak intensity is also observed (104) it disappeared and so did the peak (226).

Table (4.1): Structural parameters of $Cd_{1-X}Mg_X Fe_2O_4$. before plasma exposure.

The Component	(hkl)	Peak-position (2theta)	FWHM	Size of crystallite D (nm)	$\delta = 1/D^2$ nm^{-2}	d_{hkl} (nm)	a(nm)
$CdFe_2O_4$	(222)	35.8	0.1577	32.78025	0.000930	0. 2625	0.86392
$Cd_{0.8}Mg_{0.2}Fe_2O_4$	(222)	35.56	0.1371	28.93128	0.001194	0. 2485	0.87258
$Cd_{0.6}Mg_{0.4}Fe_2O_4$	(222)	35.45	0.1811	20.55399	0.002367	0. 2528	0.86738
$Cd_{0.4}Mg_{0.6}Fe_2O_4$	(222)	35.55	0.1574	19.76503	0.002559	0. 2507	0.87847
$Cd_{0.2}Mg_{0.8}Fe_2O_4$	(222)	35.61	0.118	36.49799	0.000750	0.2552	0.87050
$MgFe_2O_4$	(222)	35.82	0.1397	27.64796	0.001308	0.2528	0.87327

When the magnesium concentration is increased at x=0.4, we notice a decrease in the peak intensity with the appearance of the peak intensity (111), (004), (133). Also, after exposure with plasma, the intensity of the peaks decreased after plasma exposure. The intensity of the peak also disappeared (111), (104), (133).

When x=1 the intensity of the peak is at (222), but after exposure with plasma, the intensity decreased for this peak, while the peak (022) and (044) increased after exposure and the peak disappeared (266). It can be explained that the plasma may have affected the rearrangement of the atoms in the crystal lattice and changed the location of the atoms.

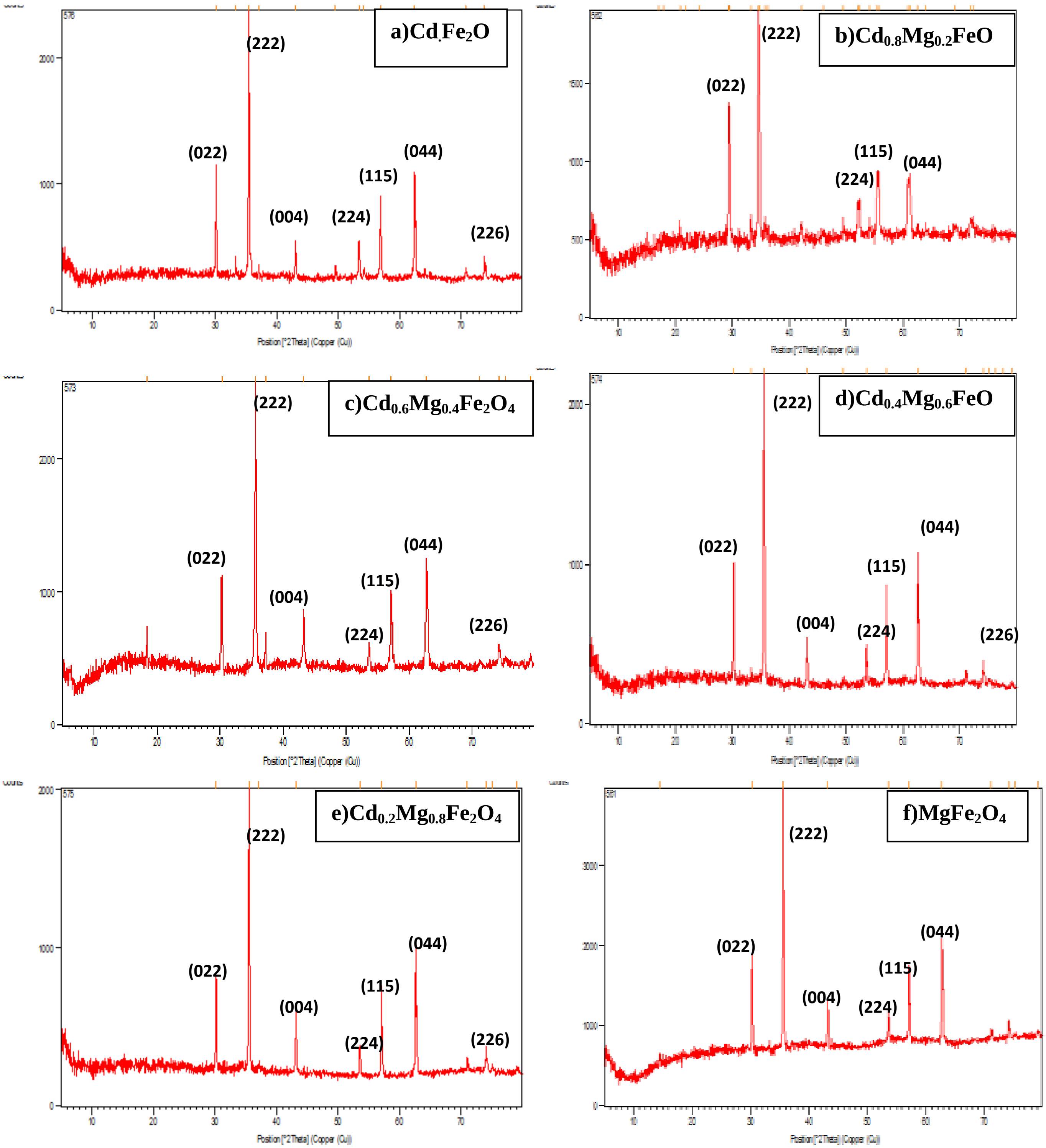

Figure (4.2): X-Ray patterns of $Cd_{1-X}Mg_X Fe_2O_4$ with a)x=0, b)x=0.2, c)x=0.4, d)x=0.6, e)x=0.8 and f)x=1Mg after plasma exposure.

Crystal size (D), which can be taken as an indicator of the particle size as shown in Table (4.2). It was observed that the value of (D) decreases after exposure to plasma than its value before exposure. The value of (a) decreases after exposure to plasma for all concentrations compared to its values before exposure. Thus, X-ray measurements showed that samples exposed to plasma have a cubic spinel structure, and the variation of structural parameters with exposure is not uniform, which enhances the diffusion of atoms deposited on the substrate and improves the crystallinity and grain size of the sample. The plasma exhibits a strong tendency for molecular adsorption on the surface of the substrate during the deposition process, so the movement of incoming particles is limit and results in somewhat small particle size [124].

Table (4.2): Structural parameters of $Cd_{1-X}Mg_X Fe_2O_4$ after plasma exposure.

The Component	(hkl)	Peak-position (2theta)	FWHM	Size of crystallite D (nm)	$\delta = 1/D^2$ nm^{-2}	d_{hkl} (nm)	a(nm)
$CdFe_2O_4$	(222)	35.04	0.1422	30.35334	0.000756	0.25310	0.87673
$Cd_{0.8} Mg_{0.2}Fe_2O_4$	(222)	34.55	0.1520	26.09525	0.001468	0.25935	0.83838
$Cd_{0.6} Mg_{0.4}Fe_2O_4$	(222)	35.56	0.1810	20.56535	0.002364	0.2522	0.87362
$Cd_{0.4} Mg_{0.6}Fe_2O_4$	(222)	35.53	0.1837	16.93531	0.003486	0.2524	0.87431
$Cd_{0.2} Mg_{0.8}Fe_2O_4$	(222)	35.52	0.1921	22.41938	0.001989	0.2525	0.87646
$MgFe_2O_4$	(222)	35.58	0.1717	22.49516	0.001976	0.25208	0.87320

Upon examination of $Cu_{1-x}Mg_xFe_2O_4$, the compound is identical to the card ((No.96-591-0006), as shown in Figures(4.3 a,b) showing diffraction peaks at the crystal levels (022), (222), (004), (224), (115), (044), (226) fixing the concentrated spinel phase (FCC) for all the prepared samples without the presence of impurities or secondary phases and this result that the preparation method. The XRD scan is perform for the rest of the samples according to the ratio x = (0, 0.2, 0.4, 0.6, 0.8 and 1) for the ferrite compound as in Figures (4.3c, d, e, and f). The prevailing trend of crystal growth (222) the width of the peak increases and decreases depending on the concentration, which increases with decreasing intensity of copper ion, and that there is a slight shift to the right in the copper ferrite, which indicates a decrease in the crystalline frit of copper. Diffraction peaks doped samples showed minor shift in their positions towards higher diffraction angles which means that Mg^{+2} ions were simultaneously replaced by the Cu^{+2} ions. These results are in accordance with the fact that the substituted ions accommodate the crystallographic sites [28].

When the Mg ion concentration increases this leads to a remain to the preferred direction of crystal growth with increases of the intensity of due to, the pressure on the crystal structure and the difference in crystal sizes between the replaced ions as a result of the difference of the ionic radius for copper it leads to a decrease and increase in the size of the nanoscale. Table (4.3) shows the structural parameters measurements, the volume (D) was calculated, where d is the spacing among the charts obtained from Bragg and hkl are miller indices. The lattice coefficient a, as shown in Table (4.2). As the (x) ratio of the Mg ion increases, the crystal size change, increasing it leads to a decrease in the size of the nanoscale levels whenever the Cu^{+2} are replaced by the Mg^{+2} ions due to difference the crystal size of the particles where the Cu ion radius is smaller

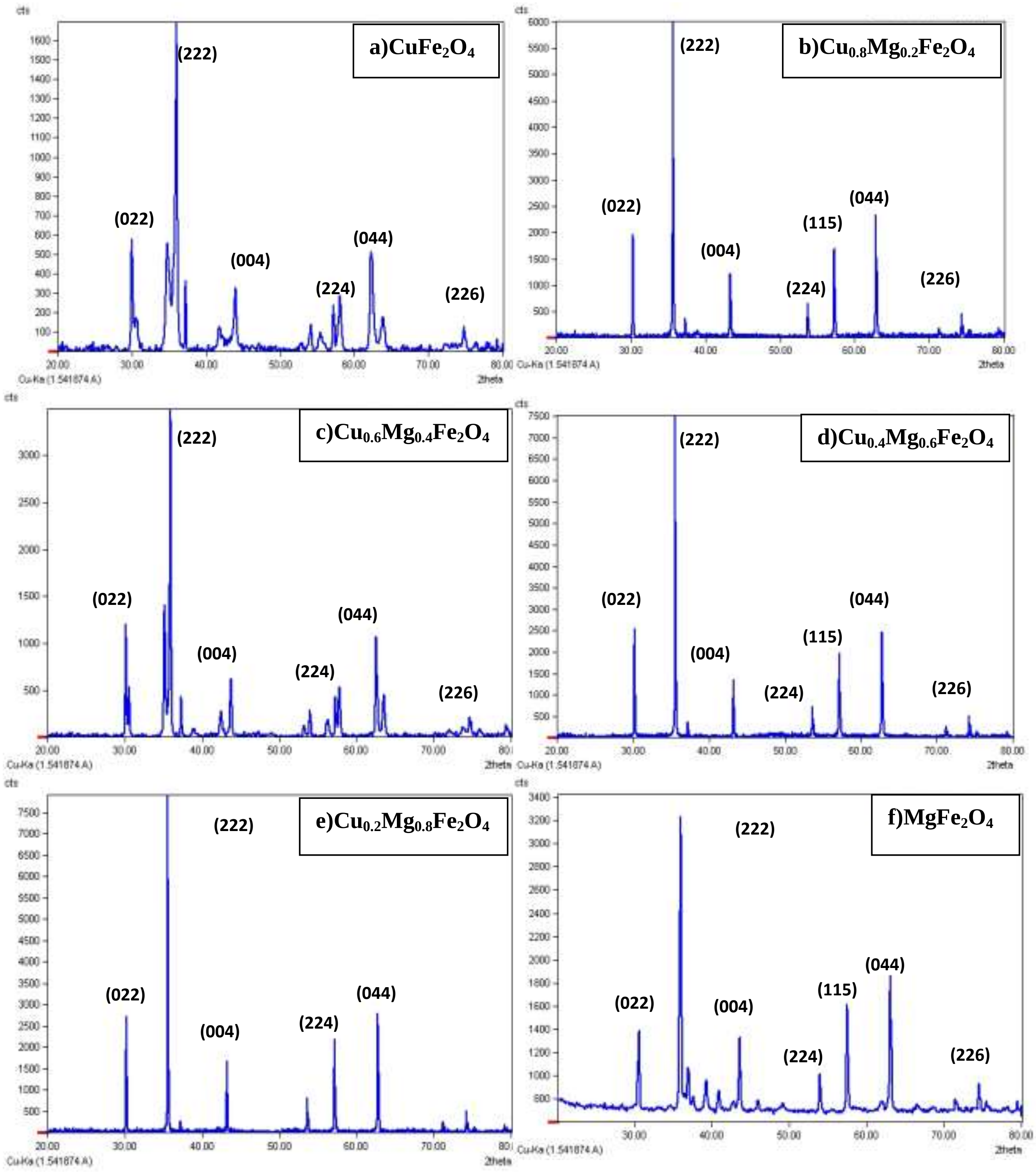

Figure (4.3): X-Ray patterns of $Cu_{1-X}Mg_X Fe_2O_4$ with a)x=0, b)x=0.2, c)x=0.4, d)x=0.6, e)x=0.8 and f)x=1 Mg before plasma exposure.

than the ionic radius of Mg, lead to the decrease in the interface distance to the internal surfaces d_{hkl} and the increase in the intensity and led to the crystal shrinkage and thus reducing its crystal size [49].

Table (4.3): Structural parameters of $Cu_{1-X}Mg_X Fe_2O_4$. before plasma exposure.

The Component	(hkl)	Peak-position (2theta)	FWHM	Size of crystallite D (nm)	$\delta = 1/D^2$ nm^{-2}	d_{hkl} (nm)	a(nm)
$CuFe_2O_4$	(222)	35.97	0.137	30.733	0.000702	0.2494	0.82292
$Cu_{0.8}Mg_{0.2}Fe_2O_4$	(222)	35.68	0.157	25.264	0.001566	0.2513	0.87050
$Cu_{0.6}Mg_{0.4}Fe_2O_4$	(222)	35.49	0.136	27.370	0.001334	0.2511	0.86981
$Cu_{0.4}Mg_{0.6}Fe_2O_4$	(222)	35.59	0.157	19.815	0.002546	0.2536	0.87847
$Cu_{0.2}Mg_{0.8}Fe_2O_4$	(222)	35.61	0.118	33.497	0.000750	0.2511	0.86981
$MgFe_2O_4$	(222)	35.62	0.119	32.457	0.000949	0.2521	0.87527

After exposure of plasma the prevailing trend of crystal growth remained at (222), while the intensity of the peak decreased for most of the concentrations compared to before the samples were exposed to plasma, a peak (111) appeared at x= (0, 0.4 and 0.6), Figures (4.4 a, c and d), at x=0.6 the peak (113) appeared but the peak (226) is disappeared, in the Figure (4.4 e, f), is not change after plasma exposure.

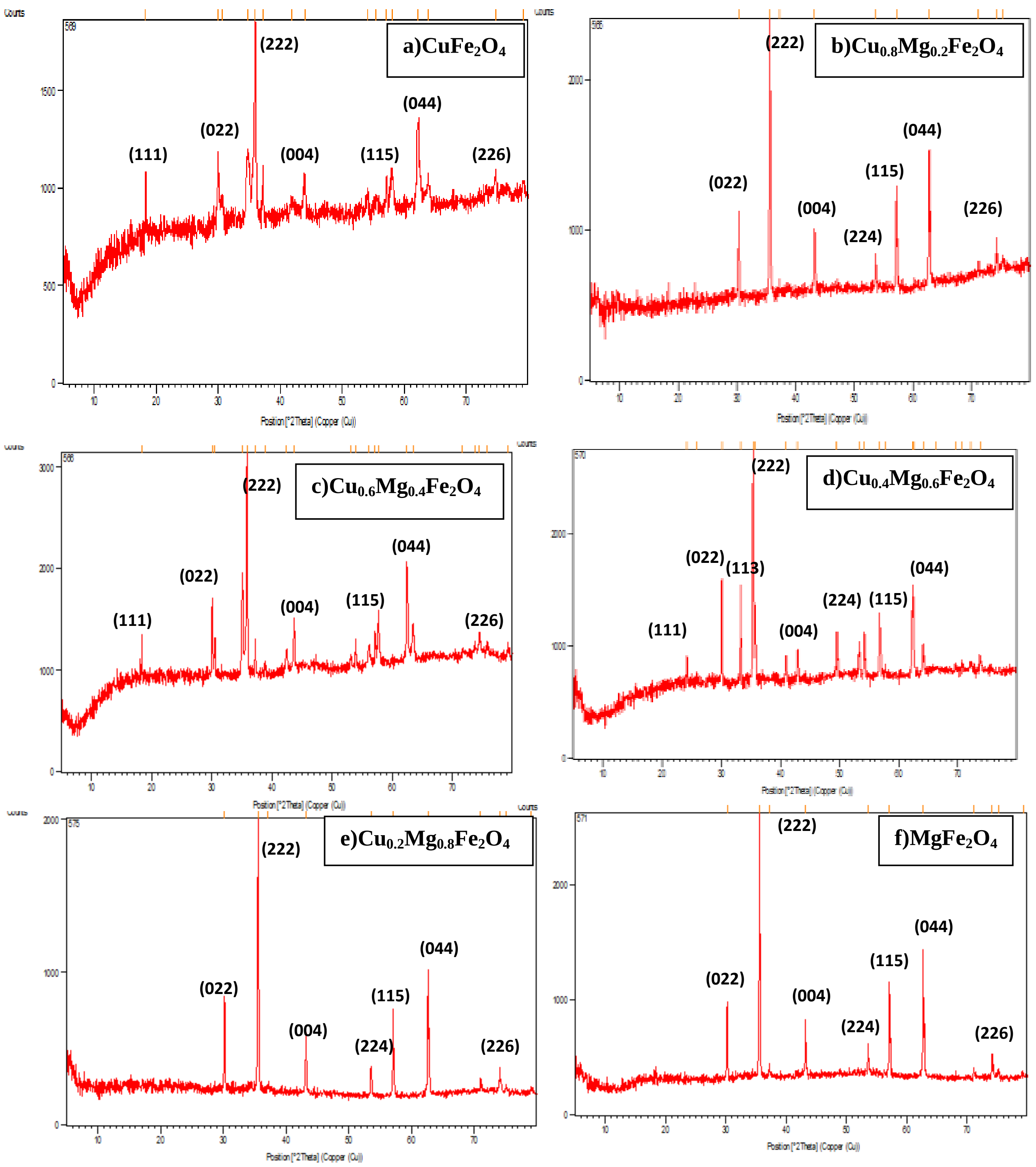

Figure (4.4): X-Ray patterns of $Cu_{1-X}Mg_X Fe_2O_4$ with a)x=0, b)x=0.2, c)x=0.4, d)x=0.6, e)x=0.8 and f)x=1 Mg after plasma exposure.

Results such as these on the relative intensity of some reflective have been reported by a study and have been attributed to a distortion in the cubic lattice after plasma exposure, Figure (4.4d)[126]. However, at x=1 after exposure, the diffraction peaks remained the same with a decrease in intensity, Figure (4.4f). It is observe that the crystal size (D) decreased with increasing Mg concentration after plasma exposure

Parameter lattice (a) for the examined samples, it is evident that increasing concentration of Mg the parameter lattice takes increases approx. This result can be explained by the basis ionic radius is due to the substitution of ions because the ionic radius of copper (0.70Å) is smaller than that of magnesium (0.75Å).

In addition, it is clear that (a) for all plasma exposure samples is greater than that of not plasma- exposure [126]. Through the shape of the samples for X-ray measurements after exposure to plasma, much fewer peaks were found in the ones when the Mg ion concentration was increased. The maximum intensity peak before plasma exposure is (222), which is well suited to the same angle after plasma exposure.

The XRD study indicates that the sample that is not exposed to plasma and the sample that is expose to plasma are essentially cubic and it is known that these differences in XRD shapes are because the copper ferrite has undergone Jahn-Teller distortion [127].

Table (4.4): Structural parameters of $Cu_{1-X}Mg_X Fe_2O_4$ after plasma exposure

The Component	(hkl)	Peak-position (2theta)	FWHM	Size of crystallite D (nm)	$\delta = 1/D^2$ nm^{-2}	d_{hkl} (nm)	a(nm)
$CuFe_2O_4$	(222)	35.97	0.142	23.631547	0.001790	0.2494	0.87676
$Cu_{0.8} Mg_{0.2}Fe_2O_4$	(222)	35.60	0.161	25.636513	0.001647	0.2519	0.87258
$Cu_{0.6} Mg_{0.4}Fe_2O_4$	(222)	35.53	0.149	25.419426	0.001547	0.2524	0.87431
$Cu_{0.4} Mg_{0.6}Fe_2O_4$	(222)	35.56	0.191	19.797607	0.002505	0.2522	0.87362
$Cu_{0.2} Mg_{0.8}Fe_2O_4$	(222)	35.52	0.1287	28.563198	0.001225	0.2525	0.87466
$MgFe_2O_4$	(222)	35.58	0.152	28.361976	0.001243	0.2520	0.87550

4.2.2FieldEmissionScanningElectronMicroscopeTest(FESEM).

Field emission scanning electron microscopy (FESEM) provides topographical and elemental information analysis was done for all ferrite samples prepared for ferrite $Cd_{1-X}Mg_X$ Fe_2O_4 by using FESEM, which gives clear information about the particle size and shape of nanocrystal[27]. Nano-crystals are find for each of the as-prepared compounds as shown in the Figures(4.5 a, b, c, d, e and f) and the particles differed from each other in size and FE-SEM micrographs it shows that the grains have a non-uniform grain size distribution. The particle sharpness is somewhat spherical, indicating crystallization also confirmed by the XRD pattern except at higher concentration.

It is also clear from the pictures that it is not uniform distributed and the particle size increases as Cd^{+2} cadmium ions are replaced by Mg^{+2} magnesium ions in the crystal lattice because the ionic half-diameters of Cd^{+2} ions are larger than that of Mg^{+2} ions, this increase crystal size ranges between (14.08-55.60) nm as in the Figures (4.5 c, d, e and f). The reason for this increase in crystal size is the substitution of the cadmium ion to replace it the magnesium ion. The as-prepared particles differ from each other and for all samples, they are usually nanoscale or microscale. These results also matched those of XRD [23].

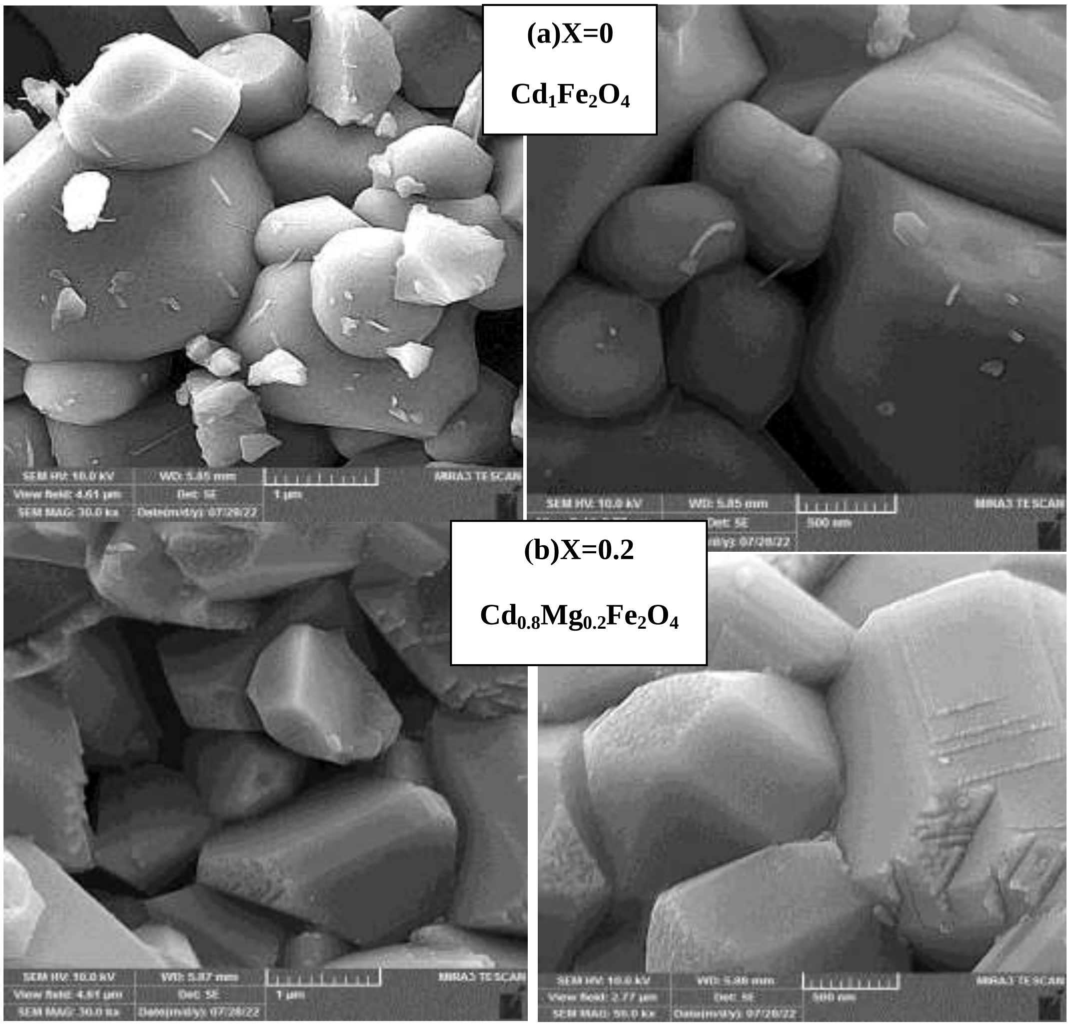

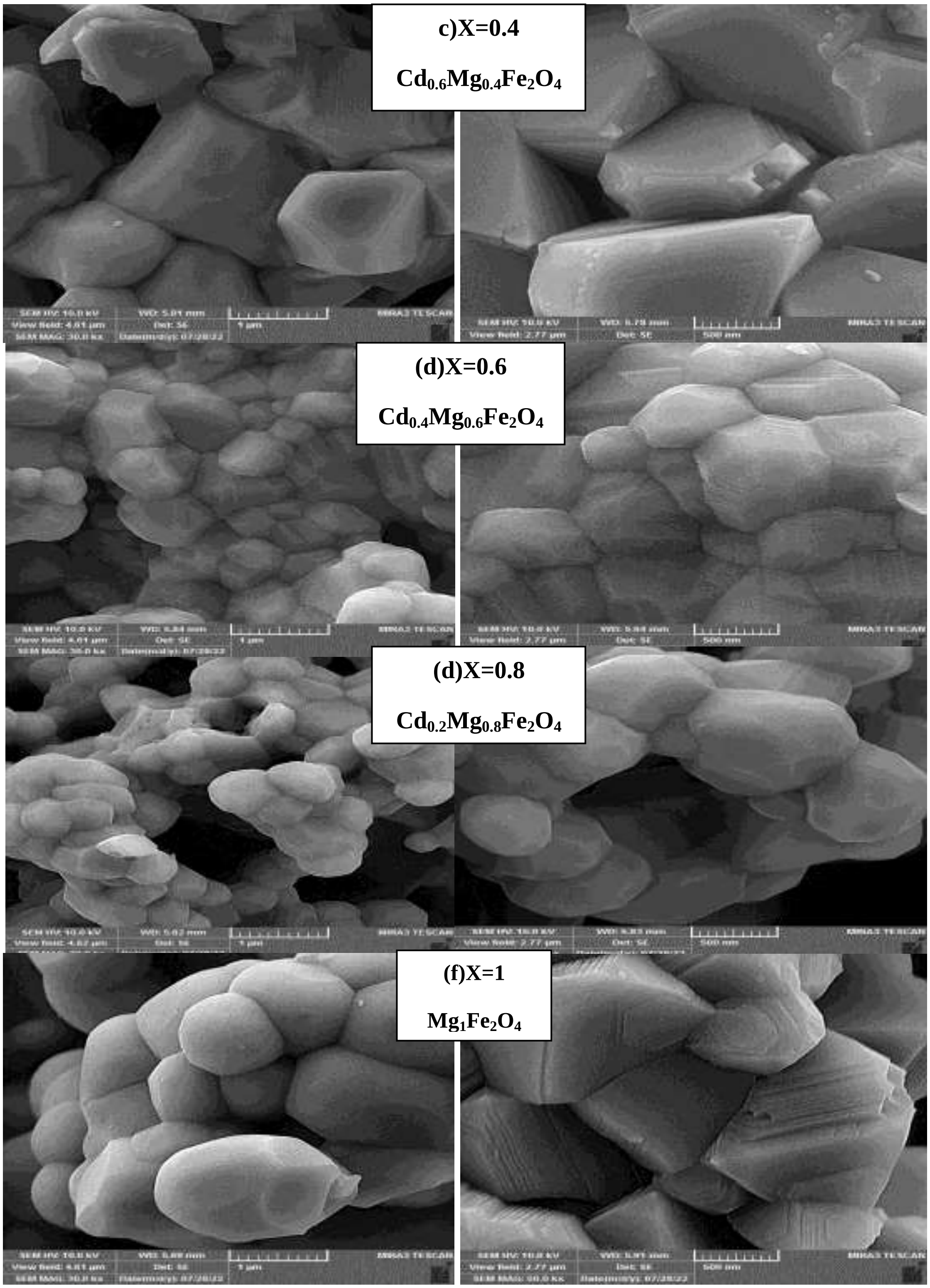

Figure (4.5): FESEM images of $Cd_{1-x}Mg_x Fe_2O_4$ with a)x=0, b)x=0.2, c)x=0.4, d)x=0.6, e)x=0.8 and f)x=1 Mg before plasma exposure.

After the exposure of the compound $Cd_{1-X}Mg_X Fe_2O_4$ to plasma, we notice a change in the topography of the surface, also a clear change at the concentration (x = 1) in the surface structure after exposure to the plasma, this change the crystal size decrease ranges between (12.1- 41.33) nm after the substitution of the cadmium ion to replace it the magnesium as in the Figures (4.6 c, d, e and f) and the surface exposed to the plasma shows a change in the positions of the crystals and their cohesion with each other after the plasma carries them away to most concentrations, which may result from a increase in magnetic effect and lattice defects in ferrite nanocrystalline [128].

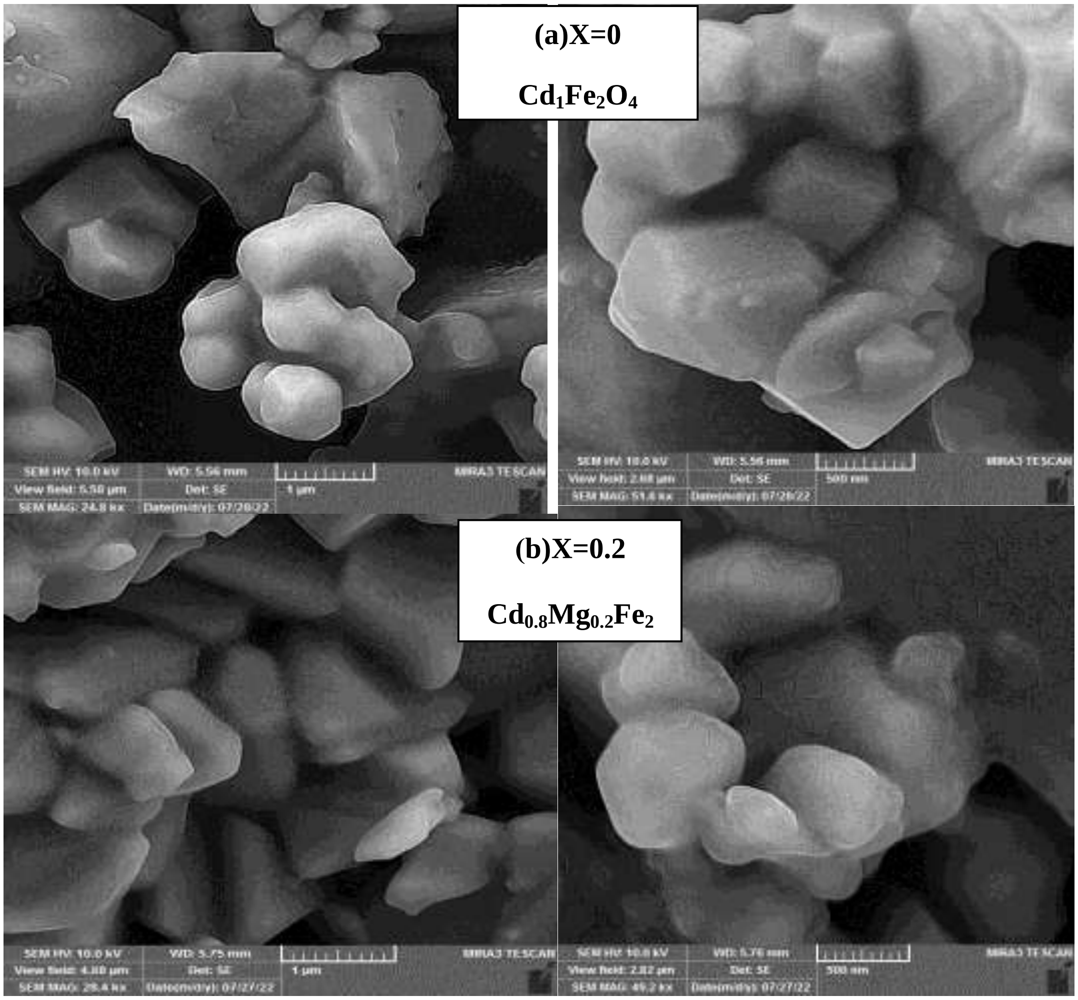

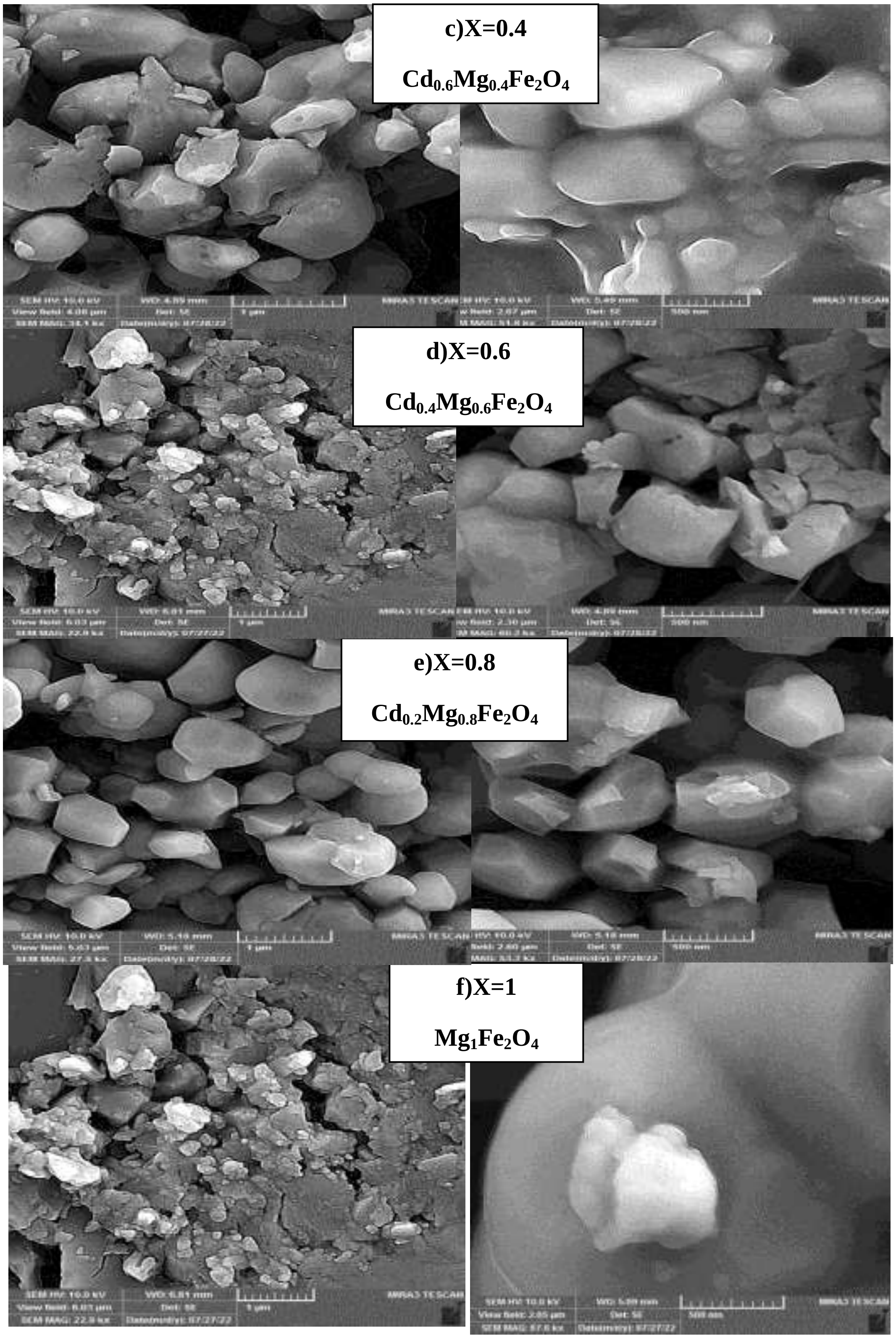

Figure (4.6): FESEM images of $Cd_{1-x}Mg_x Fe_2O_4$ with a)x=0, b)x=0.2, c)x=0.4, d)x=0.6, e)x=0.8 and f)x=1 Mg after plasma exposure.

The samples are examine according to the ratio x = (0, 1) of the ferrite compound $Cu_{1-x}Mg_x Fe_2O_4$ as shown in Figure (4.7 a, b) respectively which shows the particle shapes where it ranges crystal size of the copper ferrite is (36.14)nm. Whereas the crystal size of the magnusum frit, it (38.43)nm, it is observe that the crystal size of magnesium ferrite is larger than that of copper ferrite because the ionic radius of the magnesium ion is greater than the radius of the copper ion. The remaining samples are examine according to the ratio x=(0.2, 0.4, 0.6 and 0.8) of ferrite, this increase range between(18.115-40.213)nm, as the crystalline size of the compound $Cu_{1-x}Mg_xFe_2O_4$ decreases or increase, as the (x) value is an increase for the copper ion as shown in the figures (4.6c, d, e and f). The reason for the decrease in crystal size of the prepared particles is due to the Cu ion that occupies the surface sites of the tetrahedral, radius of the copper ion (Cu^{+2}) is smaller than that of the magnesium ion, so it cannot occupy octahedral positions.

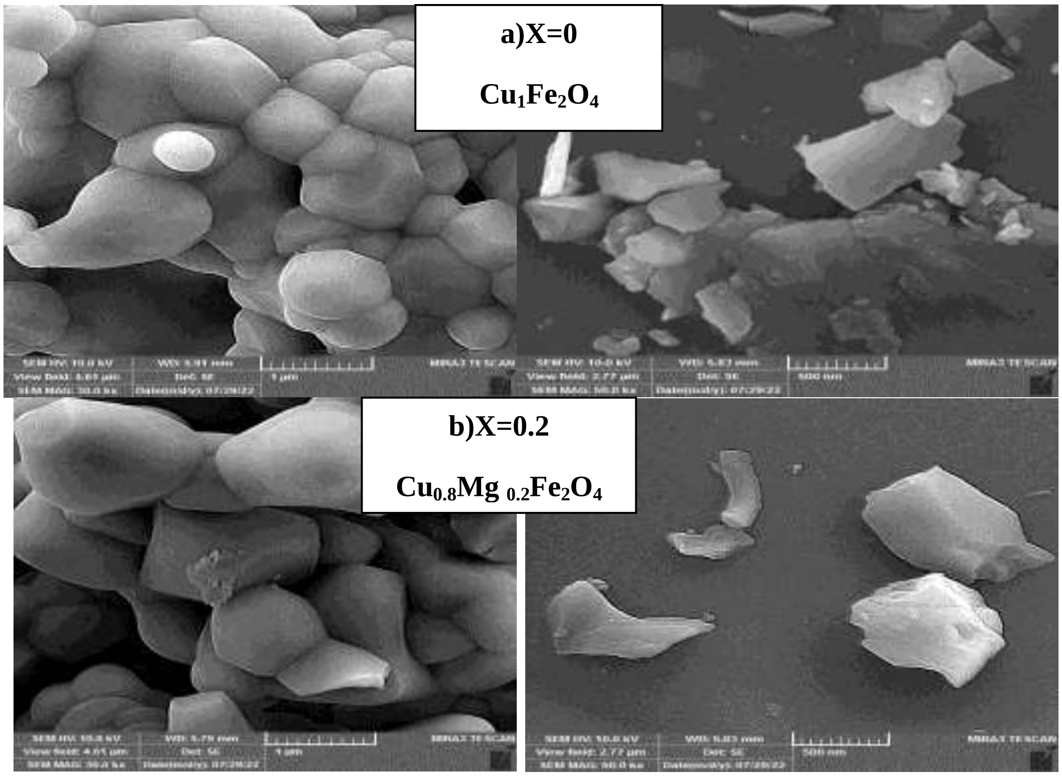

a)X=0

$Cu_1Fe_2O_4$

b)X=0.2

$Cu_{0.8}Mg_{0.2}Fe_2O_4$

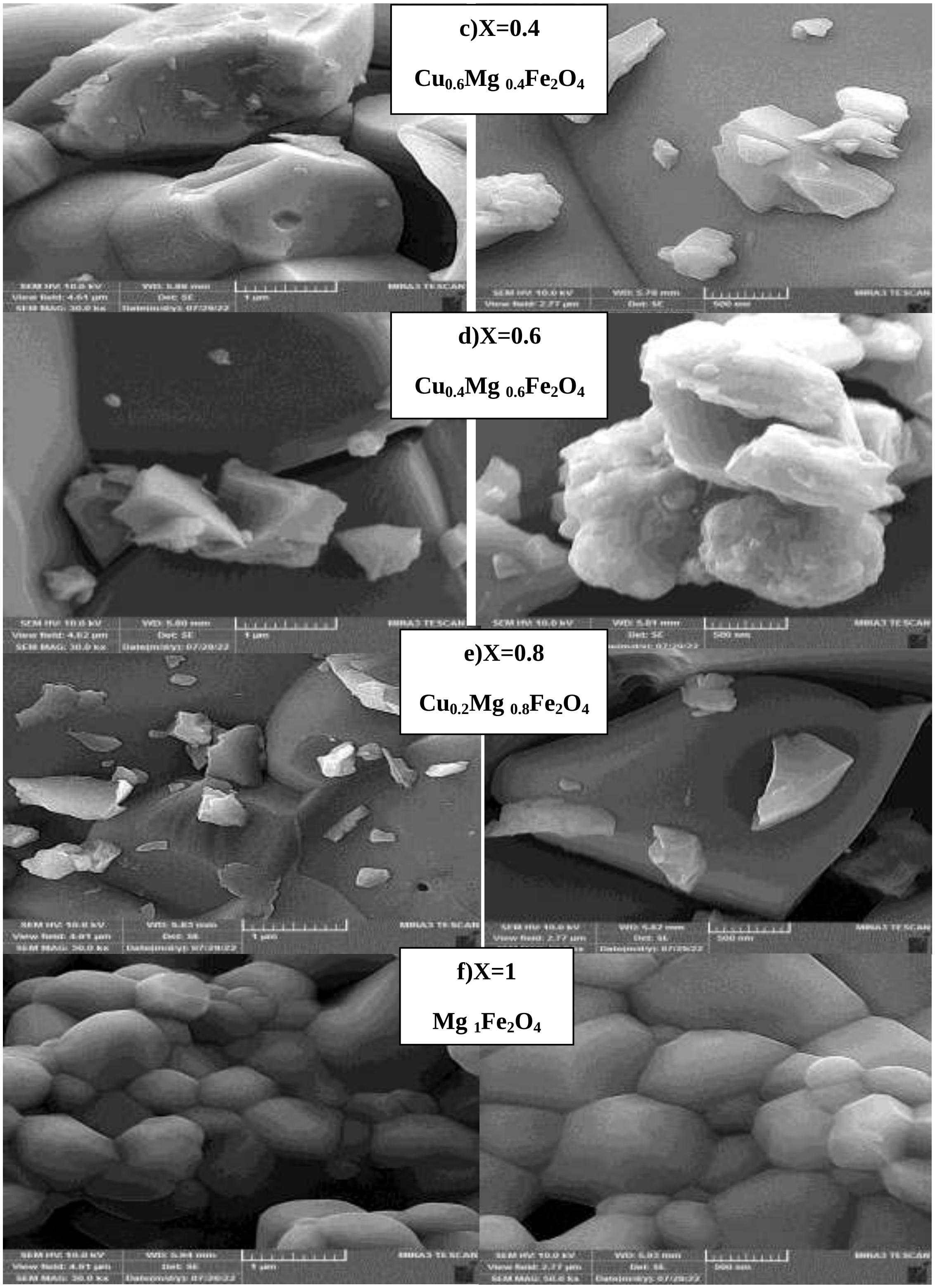

Figure (4.7): FESEM images of $Cu_{1-x}Mg_x Fe_2O_4$ with a)x=0, b)x=0.2, c)x=0.4, d)x=0.6, e)x=0.8 and f)x=1 Mg before plasma exposure.

Therefore, the presence of the copper ion at the surface of the tetrahedral site leads to a decrease in the size of the nanoparticles, that is, the particle rate decreases as the copper ion (Cu^{+2}) is replaced by the magnesium ion (Mg^{+2}) in the crystal lattice [14]. The results of the XRD examination matched the results obtained from the FESEM examination.

The samples are examined according to the different ratios of magnesium ion concentrations for the $Cu_{1-x}Mg_x Fe_2O_4$ ferrite compound, as shown in Figure (4.8a), change in the size and shape of the sample before exposure to the plasma. In terms of size the copper ferrite crystal is rather large. However, when the concentration of magnesium ion increased, a decrease in the particle size was also observed we notice a significant change in the shape and size of the crystal, as it is no longer spherical and it became inhomogeneous..

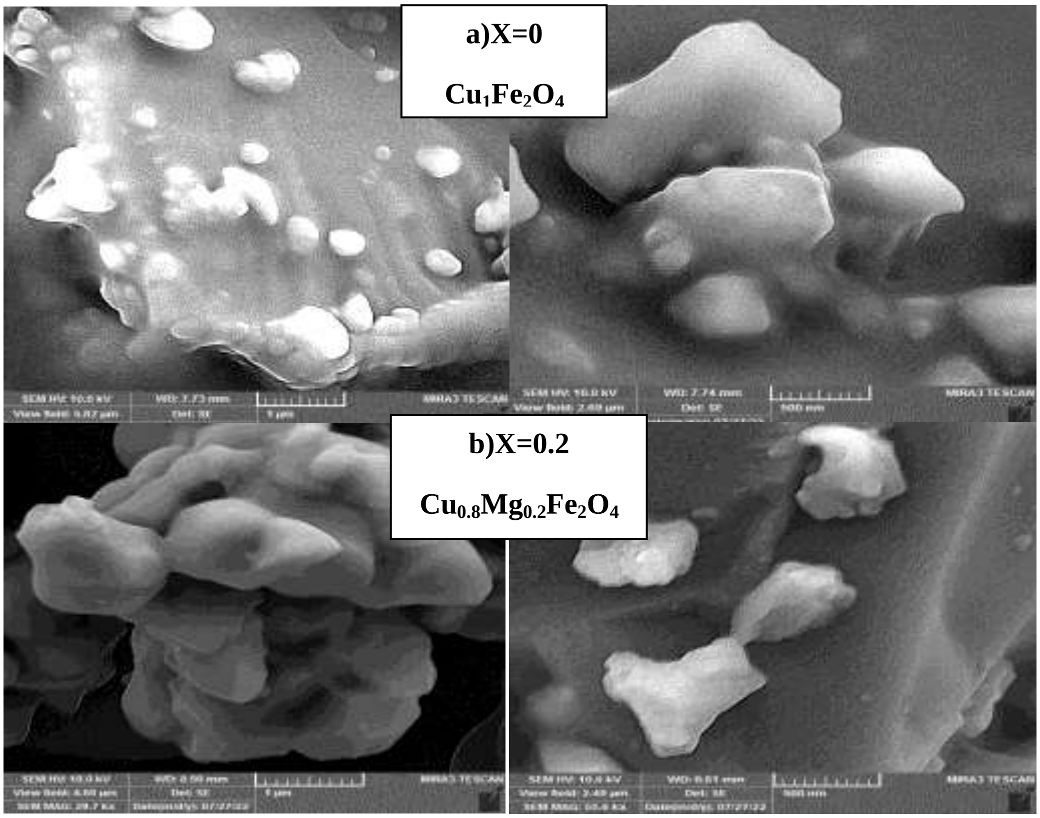

a)X=0

$Cu_1Fe_2O_4$

b)X=0.2

$Cu_{0.8}Mg_{0.2}Fe_2O_4$

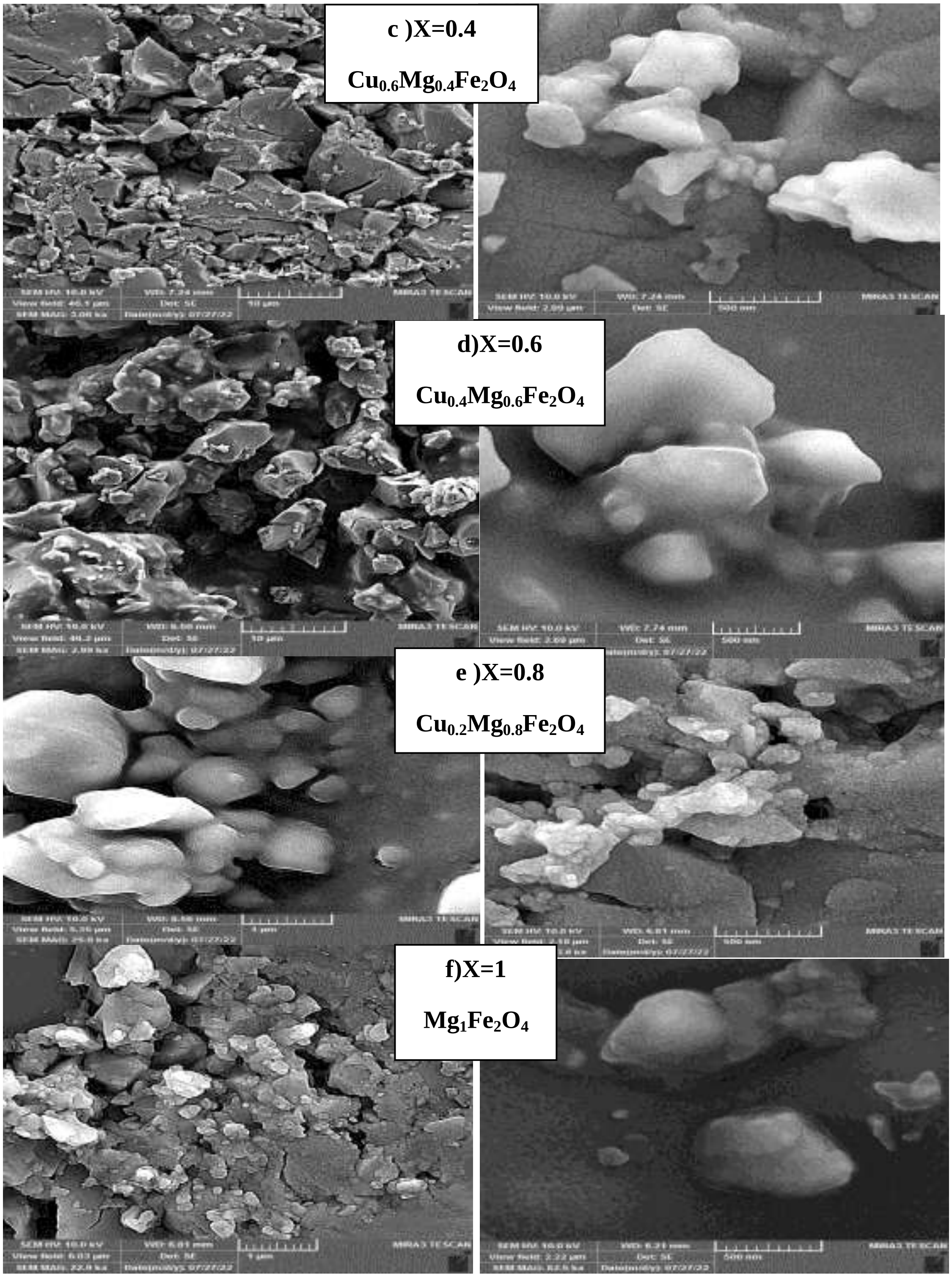

Figure (4.8): FESEM images of $Cu_{1-x}Mg_x Fe_2O_4$ with a)x=0, b)x=0.2, c)x=0.4, d)x=0.6, e)x=0.8 and f)x=1 Mg after plasma exposure.

The remaining sample x = (1) of ferrite was examined, in which the magnesium ion occupies the place of the copper ion of the compound $Cu_{1-x}Mg_xFe_2O_4$, Figure (4.8a). As for the change that occurs to the compound after exposing it to plasma, Figure (4.8), the plasma contains positive ions, electrons, atoms, or neutral gas molecules. This change is because the plasma contains positive ions, electrons, atoms, or neutral gas molecules. All of these components can interact with the surface during the plasma treatment [127].

4.2.3 Fourier-transform infrared spectroscopy analysis(FTIR)

This test is an excellent tool for studying the distribution of cations in tetrahedral sites and octahedral sites in the ferrite system and to show the properties and characterization of materials, which is a human fingerprint. For the infrared of $Cd_{1-x}Mg_xFe_2O_4$ ferrite at x =(0, 0.2, 0.4, 0.6, 0.8 and 1) where Figure (4.9) shows the FTIR spectra in the frequency range (400-4000) cm^{-1} in room temperature. That is clear from the figure that two strong absorption bands appear in the infrared spectra for each of the two samples. The high frequency band belongs to the tetrahedral site while the low frequency band belongs to the octahedral complexes. As observed from Figure (4.9), the absorption peak found may be at bands (576.37-566.41) cm^{-1}. The structural changes resulting from the metal ions that strongly affected the vibrations of the lattices, including those vibrations also depend on the cations and oxygen ion moreover the bonding strength, and the figure indicates a distinctive feature of all ferrite as the vibration modes correspond to all spinel compounds which confirmed the formation of metal oxides for the prepared compounds [15].

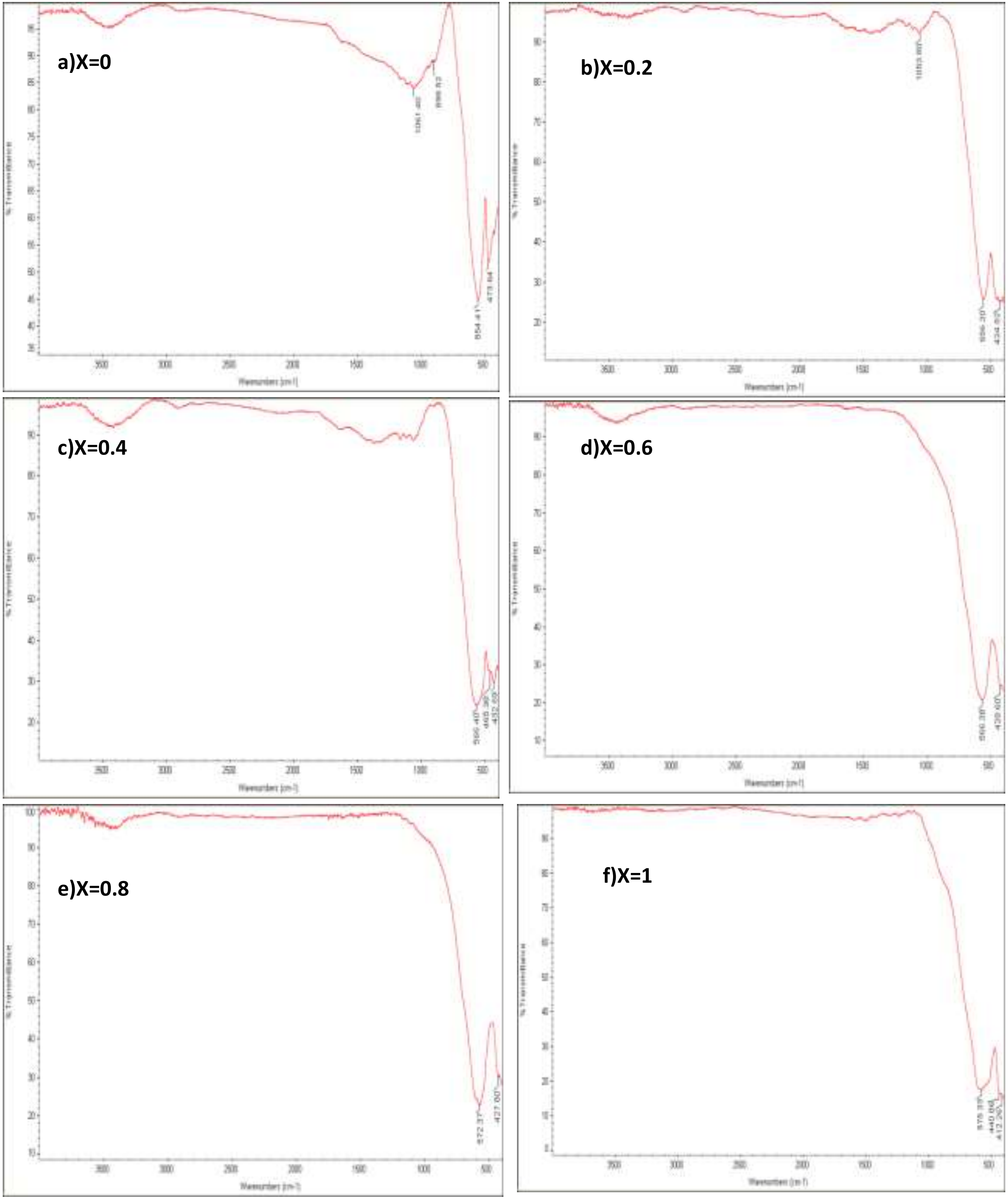

Figure (4.9): FTIR for ferrite component $Cd_{1-x}Mg_xFe_2O_4$,a)x=0, b)x=0.2, c)x=0.4, d)x=0.6, e)x=0.8 and f)x=1 Mg before plasma exposure.

The main vibrations occur led to a small red displacement in the peaks with the value (x) when increasing the magnesium ion due to the increased contribution of this element to the electronic density of the iron oxygen [21].

After exposure of the compound to plasma FTIR spectroscopy indicates sites the ions participating in the crystal lattice through vibration modes. Infrared spectra in Figure (4.10) show two essential components peaks around (557.38-434.34) cm^{-1}as well as at (2922.31-2583.56)cm^{-1} for most annealed samples, which correspond to crystal vibrations of bonds in the iron ring. It is noted that after exposure to infrared plasma it is very likely that clusters that already possess a significant dipole momentum will start such as C-O, O-H that is, the inductive or physical effect by creating an asymmetric or parabolic side with iron oxygen as a deformation of the system leads to an increase in the relaxation of cadmium with oxygen and thus its absorption by means of a red displacement [32].

Figure (4.11) shows the infrared spectrum of the compound $Cu_{1-x}Mg_xFe_2O_4$ when x= (0, 0.2, 0.4, 0.6, 0.8 and 1). Several bonds were observed through the FTIR spectrum between the (561-575) cm^{-1}. This increase led of magnesium ratio to a more red displacement than copper because it has the ability to absorbing or pushing the surrounding electronic densities equitably also because the copper radius is less than the magnesium radius, so the displacement with respect to the copper ion is greater than the magnesium ion it was clear from the results [128].

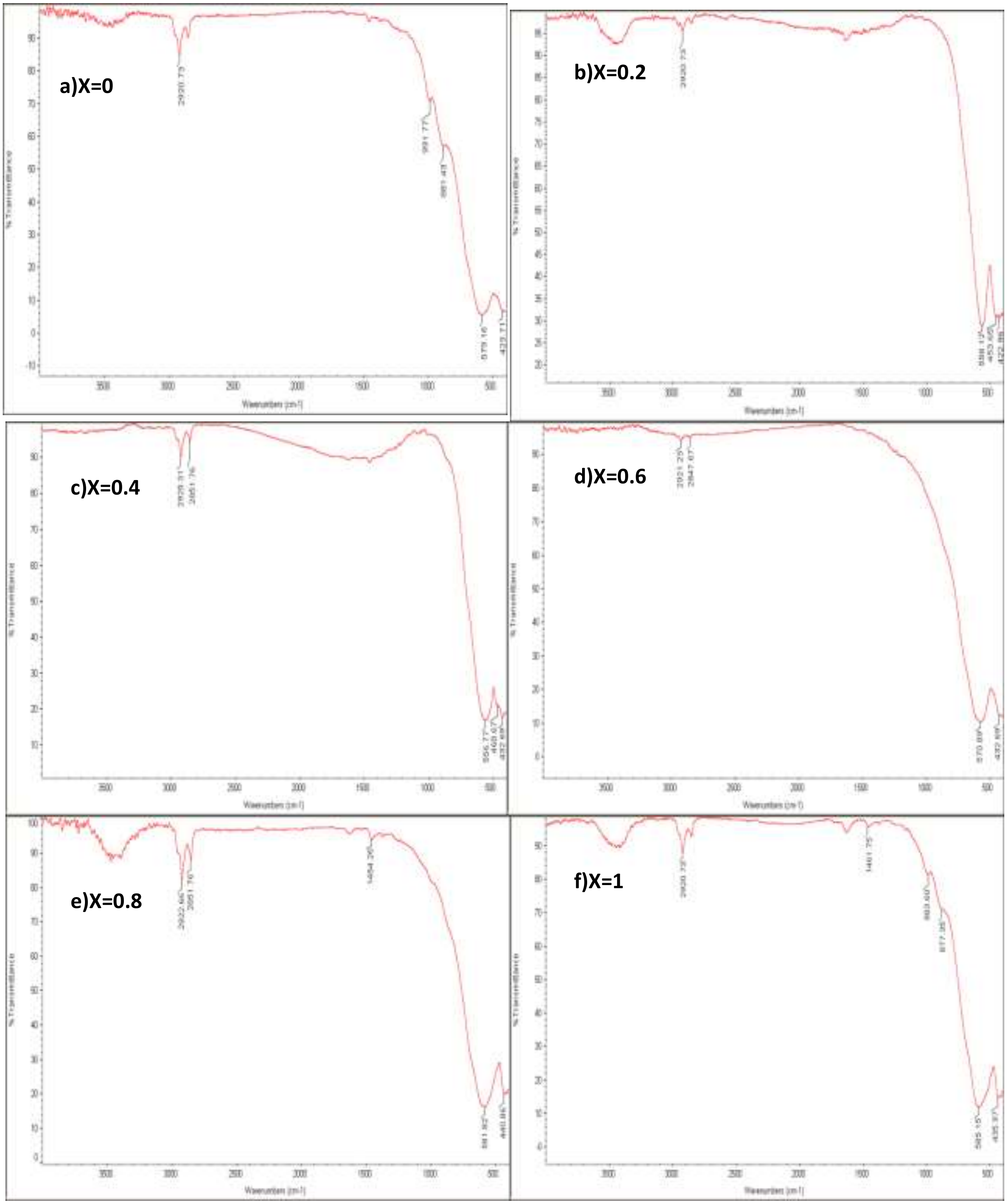

Figure (4.10): FTIR for ferrite component $Cd_{1-x}Mg_xFe_2O_4$,a)x=0, b)x=0.2, c)x=0.4, d)x=0.6, e)x=0.8 and f)x=1 Mg after plasma exposure.

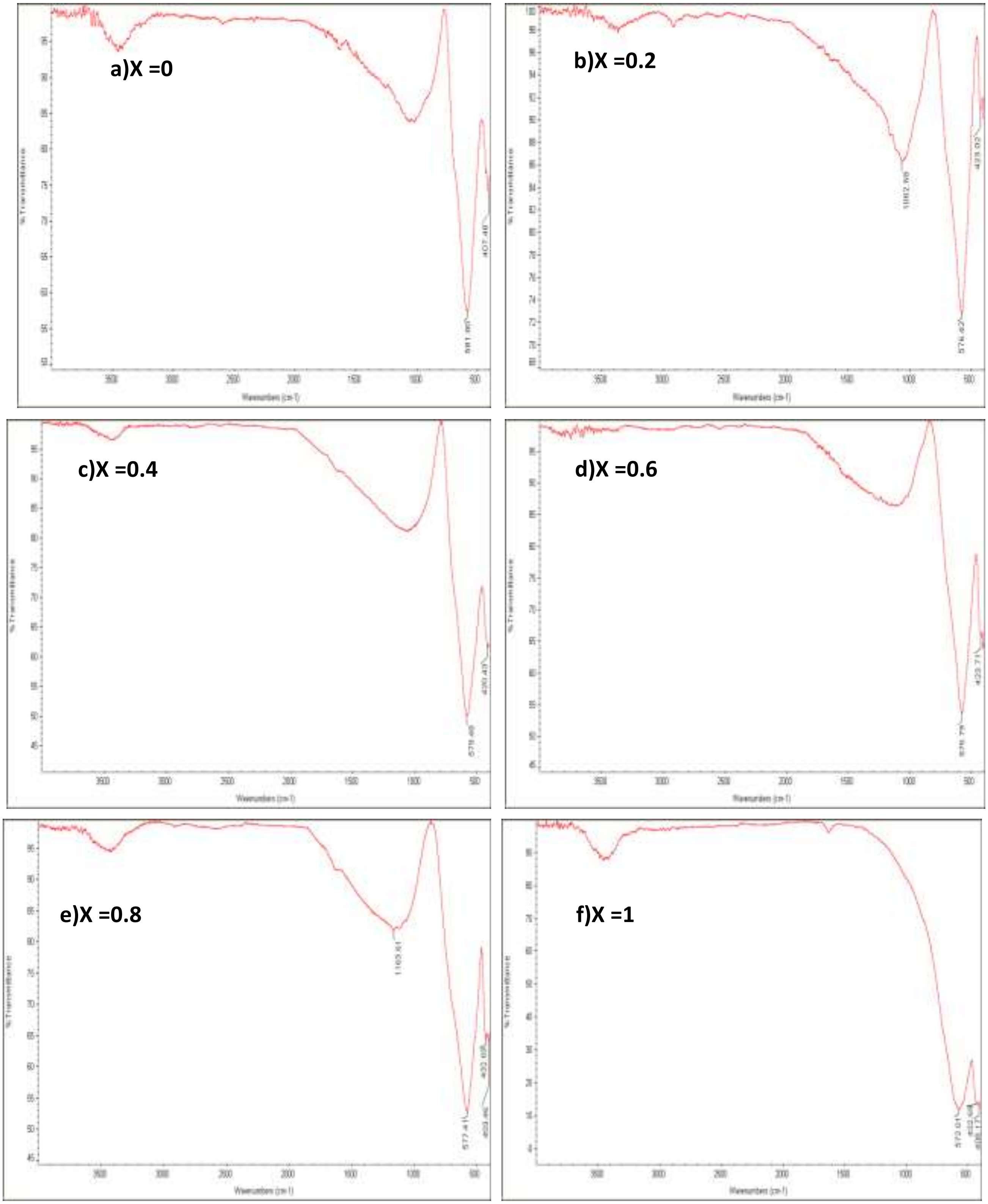

Figure (4.11): FTIR for ferrite component $Cu_{1-x}Mg_xFe_2O_4$,a)x=0, b)x=0.2, c)x=0.4, d)x=0.6, e)x=0.8 and f)x=1 Mg before plasma exposure.

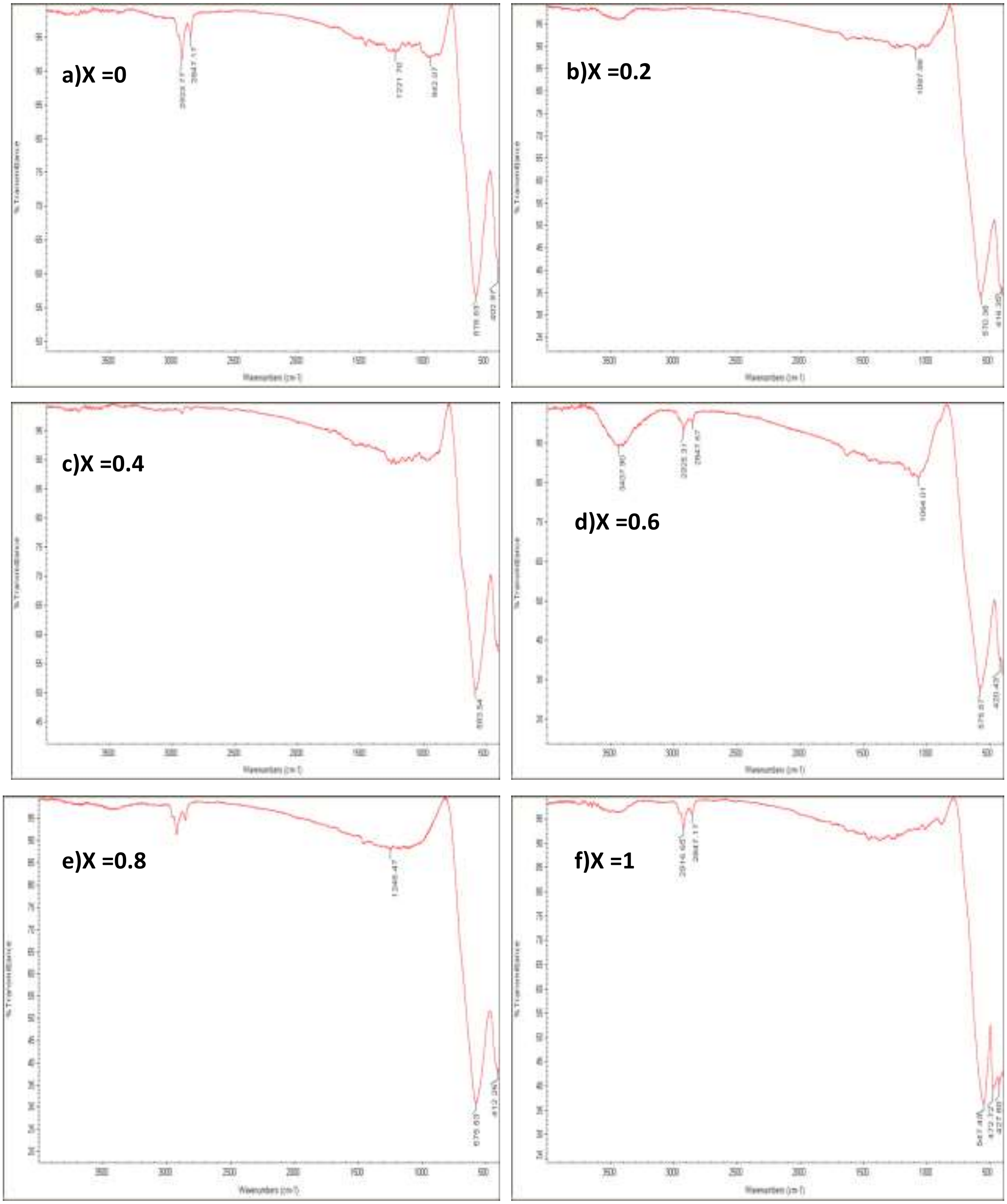

Figure (4.12): FTIR for ferrite component $Cu_{1-x}Mg_xFe_2O_4$,a)x=0, b)x=0.2, c)x=0.4, d)x=0.6, e)x=0.8 and f)x=1Mg after plasma exposure.

After exposure of the same compound $Cu_{1-x}Mg_xFe_2O_4$ to the plasma, the infrared spectra Figure (4.12) show the presence of two absorption bands at (576.31- 422.34) cm $^{-1}$ for all models, which these bands sites indicate the presence of Cu^{+2} ions in the octahedral sites and Fe^{+3} ions in the tetrahedral sites. Found that the increase in the concentration of Mg^{+2} ion , the band shifts towards higher frequencies and is evident at concentrations (x = 0, 0.6 and 1) where the infrared spectra appear (2925.75- 2847.17) cm^{-1} after exposure to plasma.

4.2.4 Vibrating Sample Magnetometer (VSM) Test.

The magnetic properties of the as-prepared samples and the magnetic field strength are studied using a vibration sample magnetometer (VSM) at room temperature. The principle of magnetic hysteresis can help in understanding the magnetic behavior of samples and also provide researchers with information about specific magnetic factors.

Figure (4.13) shows the hysteresis loop analysis of $Cd_{1-x}Mg_x Fe_2O_4$ ferrite at x = (0, 0.2, 0.4, 0.6, 0.8 and1). The Figure shows the magnetic behavior of the as-prepared composite and distinct magnetic parameters such as saturation magnetization (M_S), residual magnetization (M_r) and coercive field (H_C). These parameters are significantly affected by cation occupancy among them the tetrahedral (a) and octahedral (b) sites, secondary phases, material density and grain size.

After hysteresis loop tracing of the as-prepared nanoparticles, the narrow curves indicate the magnetic properties of ferrite spinel behavior.

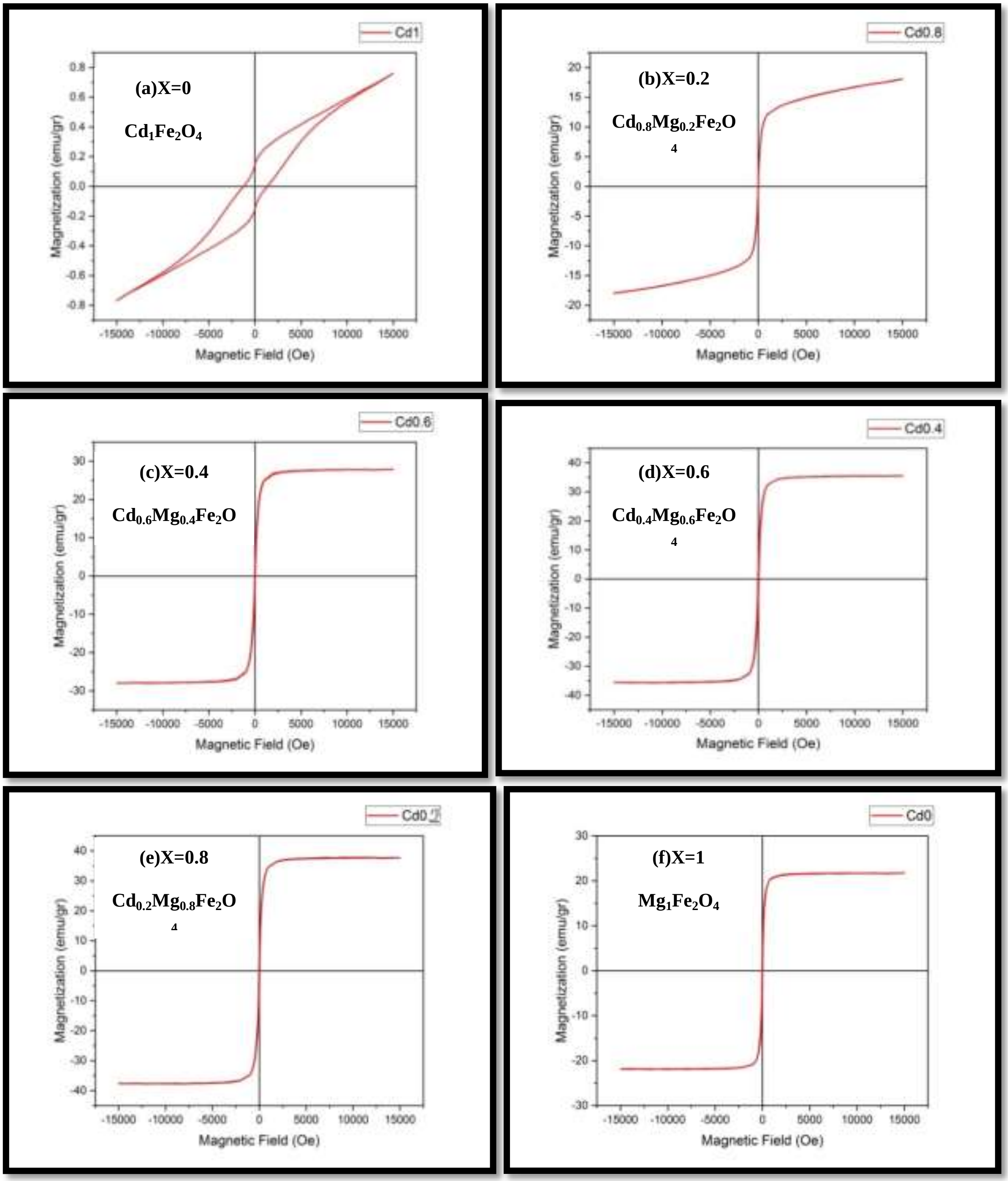

Figure (4.13): Magnetic hysteresis curves of $Cd_{1-x}Mg_x Fe_2O_4$ with a)x=0, b)x=0.2, c)x=0.4, d)x=0.6, e)x=0.8 and f)x=1 Mg before plasma exposure.

As the narrow hysteretic ring indicates a loss of magnetism, and this is one of the characteristics of soft spinel, that is, a material in which magnetism is not stored, as we notice that the area of the hysteretic ring decreases with increasing (x) of the Mg^{+2} ion [129]. The magnetic material here has a small area inside the ring which shows that a small amount of energy is dissipated. The compound content is tabulated in Table(4.5) showing saturation magnetization (M_S), coercivity (H_c) and residual magnetization (M_r). It can be seen from the Table (4.5) the increase and decrease in the saturation region of the (x) ratio, as in Figure (4.14a), as well as the difference in the residual magnetization in the (x) ratio, as in Figure (4.14b).

This is due to the size and shape of the particles and the distribution of positive ions in the tetrahedral sites and the surface of the octahedral sites and the reason for the decrease in magnetic saturation is the rearrangement of the sites between the ions and the magnetic behavior for the Cd^{+2} ion larger than the Mg^{+2} ion and this is reflected in the increase in the coercive force by increasing the Mg^{+2} as in Figure (4.14 c) [21].

This is indicated in the pure sample when Mg= 0.0 and the small increase in coercivity may be due to the anisotropy of the crystal magnetism and due to the spin perturbation on the surface of the particles [22].

Table (4.5): Magnetic saturation(M_s), remaining magnetism(M_r) and force coercive(H_c) as a function of Manganese ratio before plasma exposure.

Ratio(x)	Component	M_s emu/g	M_r emu/g	H_c Oe
0	$CdFe_2O_4$	15. 78	0.15	25
0.2	$Cd_{0.8}Mg_{0.2}Fe_2O_4$	18.11	0.33	25
0.4	$Cd_{0.6}Mg_{0.4}Fe_2O_4$	27.8	1.99	22
0.6	$Cd_{0.4}Mg_{0.6}Fe_2O_4$	32.4	3.5	28
0.8	$Cd_{0.2}Mg_{0.8}Fe_2O_4$	31.8	3.6	25
1	$MgFe_2O_4$	21.75	0.5	20

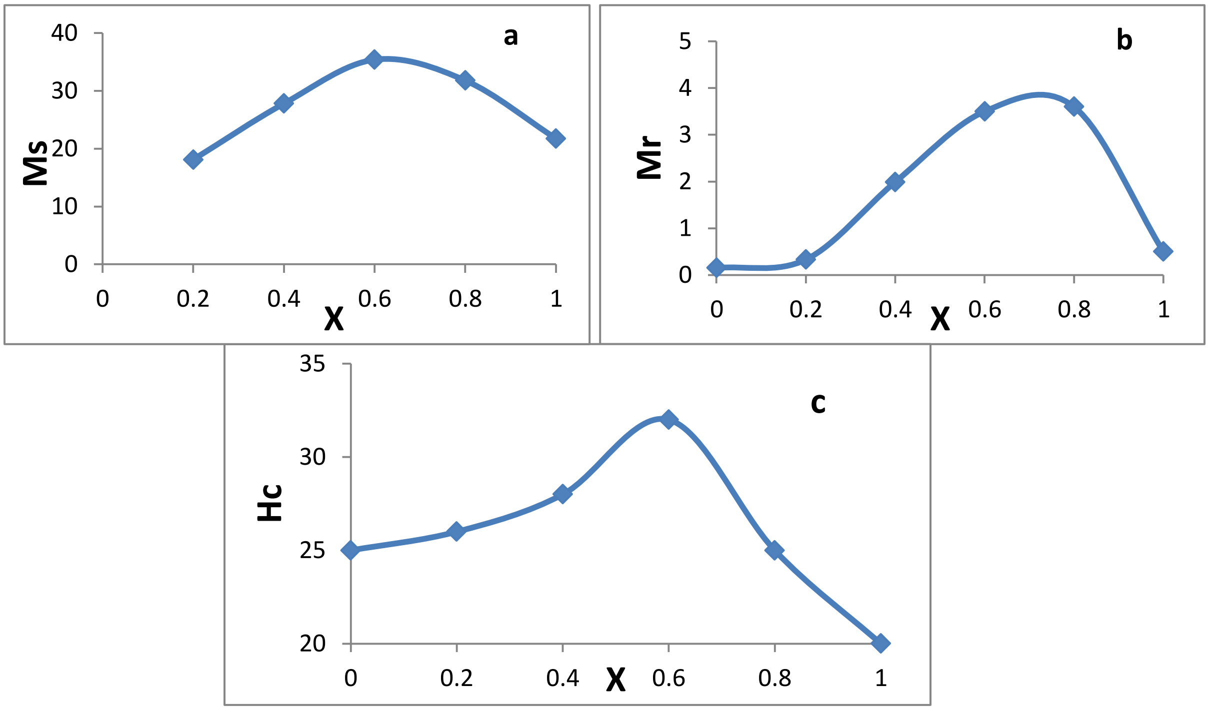

Figure (4.14): Shows the change of magnetic properties with all the ratios(x) before plasma exposure.

Figure (4.15) shows the magnetization or hysteresis loop curves of the analyzed samples for the same compound $Cd_{1-x}Mg_xFe_2O_4$ after exposure to plasma. The change is also shown in magnetization M with an applied magnetic field H at room temperature for the samples examined, notes that magnetization increases with the applied magnetic field, consistent with natural behavior in which all rings confirm the soft magnetic nature of Cd- Mg ferro.

From the Table (4.6) show the saturation magnetization increase after exposure to plasma, also it increase and decrease with increasing magnesium ion concentration (Figure (4.16a). This is because of the damage it is done for ferromagnetic ordering. We attribute the increase of M_S to the better crystallinity and larger grain size, The highest value of saturation magnetization x=0 because the crystal size of cadmium ferrite is larger than crystal size of magnesium ferrite. Also, the value of the M_r increased compared to after exposure to plasma Figure (4.16b), due it the maximum grain size obtained from compressed ferrite [130].

also the distribution of cations that is partially uniform will result in the crystal lattice the growing. Meanwhile, the H_C for the samples varied over a range as a function of increasing Mg ion concentration and also after plasma exposure. The increase in H_C could also be attributed to the increase in grain size and the highest value was at reached it at x=0.6, Figure (4.16c).

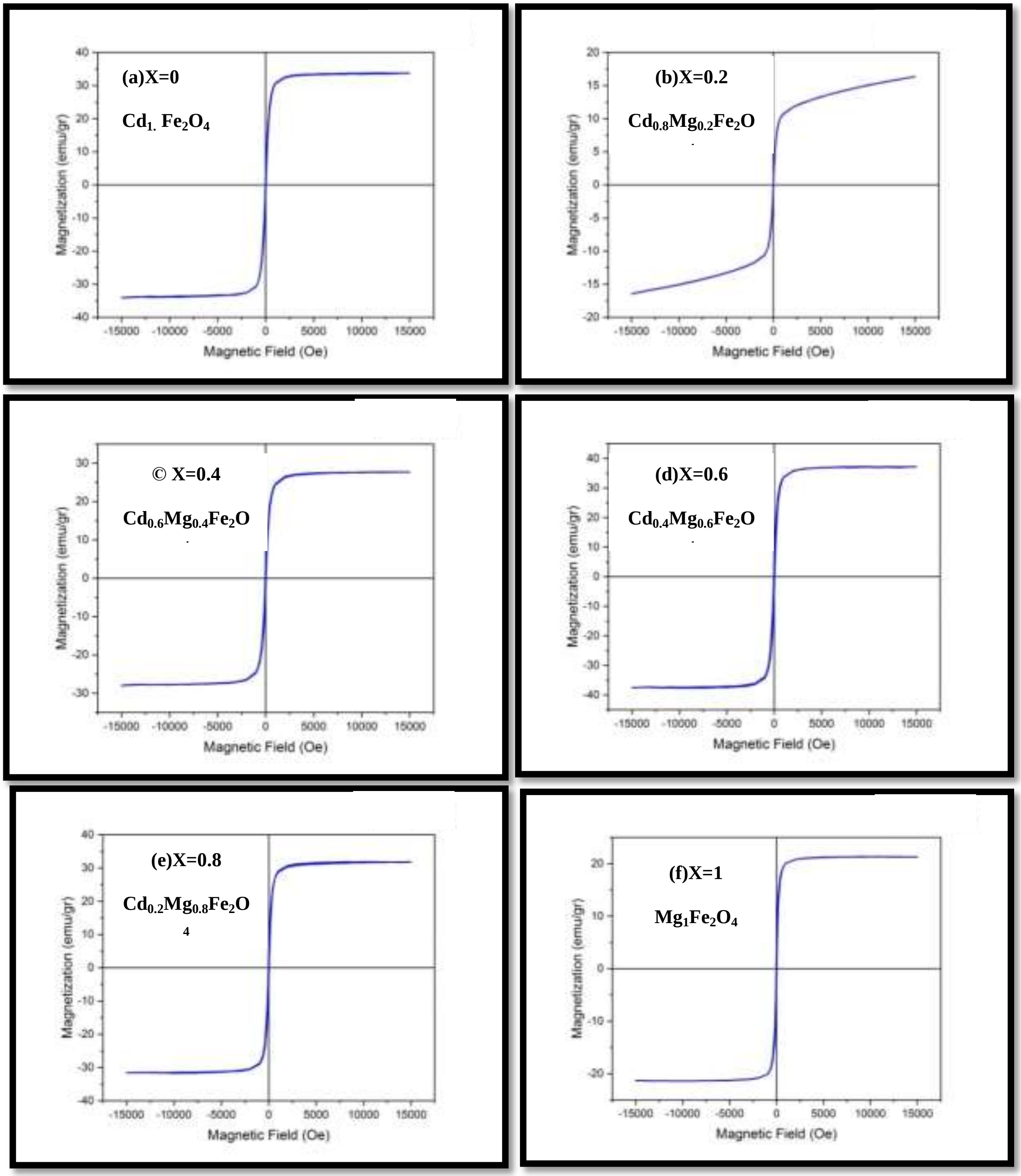

Figure (4.15): Magnetic hysteresis curves of $Cd_{1-x}Mg_x Fe_2$ with a)x=0, b)x=0.2, c)x=0.4, d)x=0.6, e)x=0.8 and f)x=1 Mg after plasma exposure.

Table (4.6): Magnetic saturation(M_s), remaining magnetism(M_r) and force coercive(H_c) as a function of Manganese ratio after plasma exposure.

Ratio(x)	Component	M_s emu/g	M_r emu/g	H_c Oe
0	$CdFe_2O_4$	33.78	1.95	25
0.2	$Cd_{0.8}Mg_{0.2}Fe_2O_4$	19.36	0.31	15
0.4	$Cd_{0.6}Mg_{0.4}Fe_2O_4$	27.7	2.75	25
0.6	$Cd_{0.4}Mg_{0.6}Fe_2O_4$	33.2	1.85	27
0.8	$Cd_{0.2}Mg_{0.8}Fe_2O_4$	31.87	3.2	25
1	$MgFe_2O_4$	21.28	2.67	25

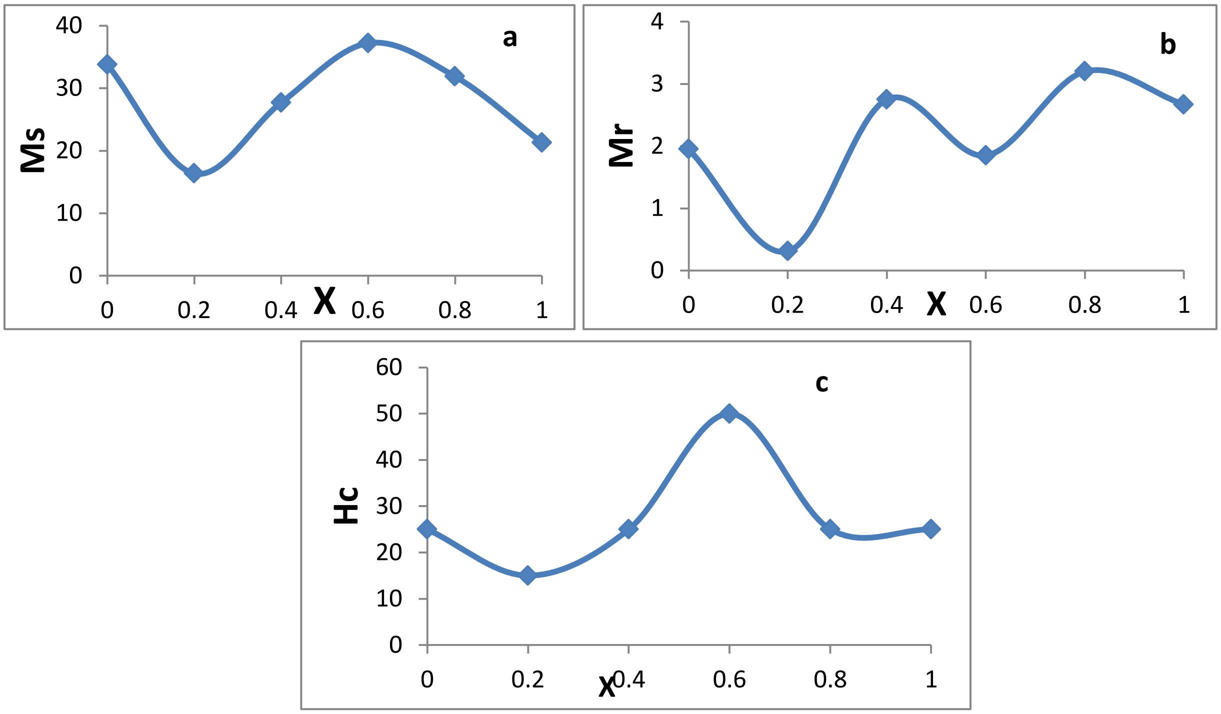

Figure (4.16): Shows the change of magnetic properties with all the ratios(x) after plasma exposure.

Figure (4.17) shows the hysteresis loop of $Cu_{1-x}Mg_xFe_2O_4$ ferrite at room temperature, from which it is possible to understand the magnetic behavior of the samples. The narrow curves indicate the magnetic properties with ferrite spinel behavior and the XRD data confirmed this result. Since a narrow hysteretic ring indicates a loss of magnetism and this is a characteristic of soft ferrite, a material that does not maintain magnetism in it the figure shows the magnetic behavior of the composite prepared at x = (0, 0.2, 0.4, 0.6, 0.8, 1) and magnetic factors such as saturation magnetism (M_s), residual magnetization (M_r) and coercive force (H_c). Where we notice a decrease in the area of the hysteretic ring with the increase of Mg^{+2} ion [14].

It is clear from the table (4.7) that the replacement of magnesium with copper leads to a continuous fluctuation in the values of magnetization. However, this increase unable to get higher magnesium dope formulations. Mg substitution enhances to a lesser extent than saturated magnetization values , which may be due to configuration Mg^{+2} ion in cubic structures. Ductility decreases with increasing magnesium concentration the decrease and increase in the saturation magnetization of the (x) ratio as in Figure (4.18a), as well as the difference with the residual magnetization ratio in the (x) ratio as in Figure (4.18b) can be seen. This is due to the particle size and shape as well as the distribution of positive ions in the tetrahedral and octahedral sites. The coercive force is illustrated in Figure (4.18c), the decrease in coercion may be due to the variation in crystal magnetism and the change in the exchange of properties due to the spin disturbance on the surface of the particles [130].

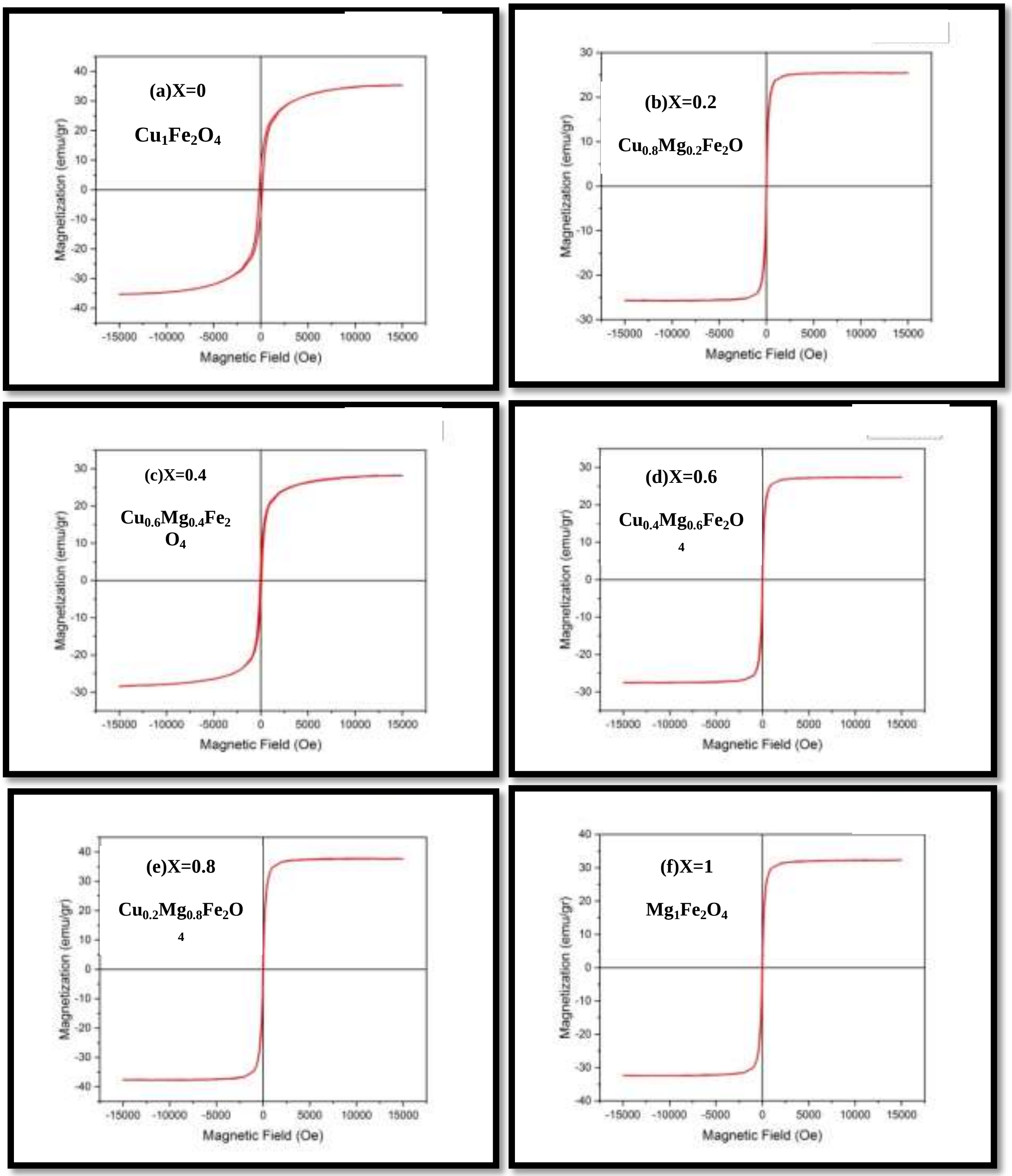

Figure (4.17): Magnetic hysteresis curves of $Cu_{1-x}Mg_x Fe_2O_4$ with a)x=0, b)x=0.2, c)x=0.4, d)x=0.6, e)x=0.8 and f)x=1 Mg before plasma exposure.

Table (4.7): Magnetic saturation(Ms), remaining magnetism(M_r) and force coercive(H_c) as a function of Manganese ratio before plasma exposure.

Ratio(x)	Component	M_s emu/g	M_r emu/g	H_c Oe
0	$CuFe_2O_4$	30.5	7.9	150
0.2	$Cu_{0.8}Mg_{0.2}Fe_2O_4$	26.15	2.22	35
0.4	$Cu_{0.6}Mg_{0.4}Fe_2O_4$	32.61	2.21	75
0.6	$Cu_{0.4}Mg_{0.6}Fe_2O_4$	32.1	2.7	50
0.8	$Cu_{0.2}Mg_{0.8}Fe_2O_4$	24.9	2.3	25
1	$MgFe_2O_4$	31.2	1.33	25

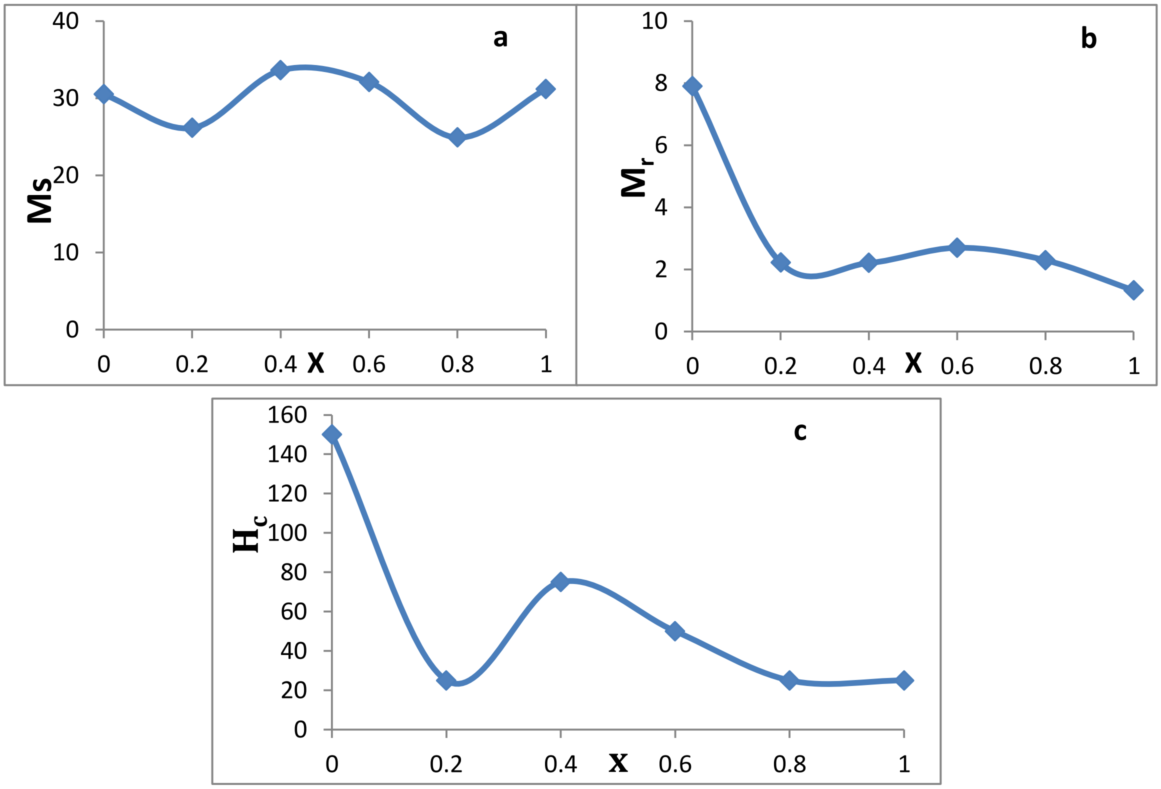

Figure (4.18): Shows the change of magnetic properties with all the ratios(x) before plasma exposure .

Figure (4.19) shows the loop magnetization or hysteresis curves of the analyzed samples of the $Cu_{1-x}Mg_xFe_2O_4$ complex after exposure to plasma. The ferrite hysteresis loop was plotted using the applied field and the corresponding magnetization. From the shapes, it is clear that it corresponds to the natural behavior in which all rings confirm the soft magnetism of Cu-Mg ferro. The narrow hysteretic ring indicates the loss of magnetism. The magnetic properties of spinel ferrite are affected by various factors, including the path of synthesis, and the distribution of the cation on the tetrahedral and octahedral sites, and increasing crystalline size with x. The magnetic properties of ferrite nanoparticles can be modified from using different doping ions [31].

In Table (4.8) the magnetic parameters were calculated using the hysteresis loop. That it is evident from the table that exposure to plasma lead the decrease and increase in the saturation region of the ratio of (x) as unexposed samples the same goes for values M_r and H_c , an increase in M_s is observed in the plasma-treated ferrite samples and higher the value was 35.8 emu/g after replacement with $MgFe_2O_4$. This escalation in saturation magnetization correlates with direct contact of ferrite samples with microwave plasma, change in compulsion can be associated with surface effects generated during plasma exposure [31].

Thus analysis of magnetic properties by microwave plasma treatment is an effective technique used to modify ferrite surface and can be valuable good in newer applications. When the ferrite samples are exposed directly to the plasma, the mobility can be improved magnetic dipoles are significantly increased due to the higher temperature, thereby enhancing saturation magnetization [131].

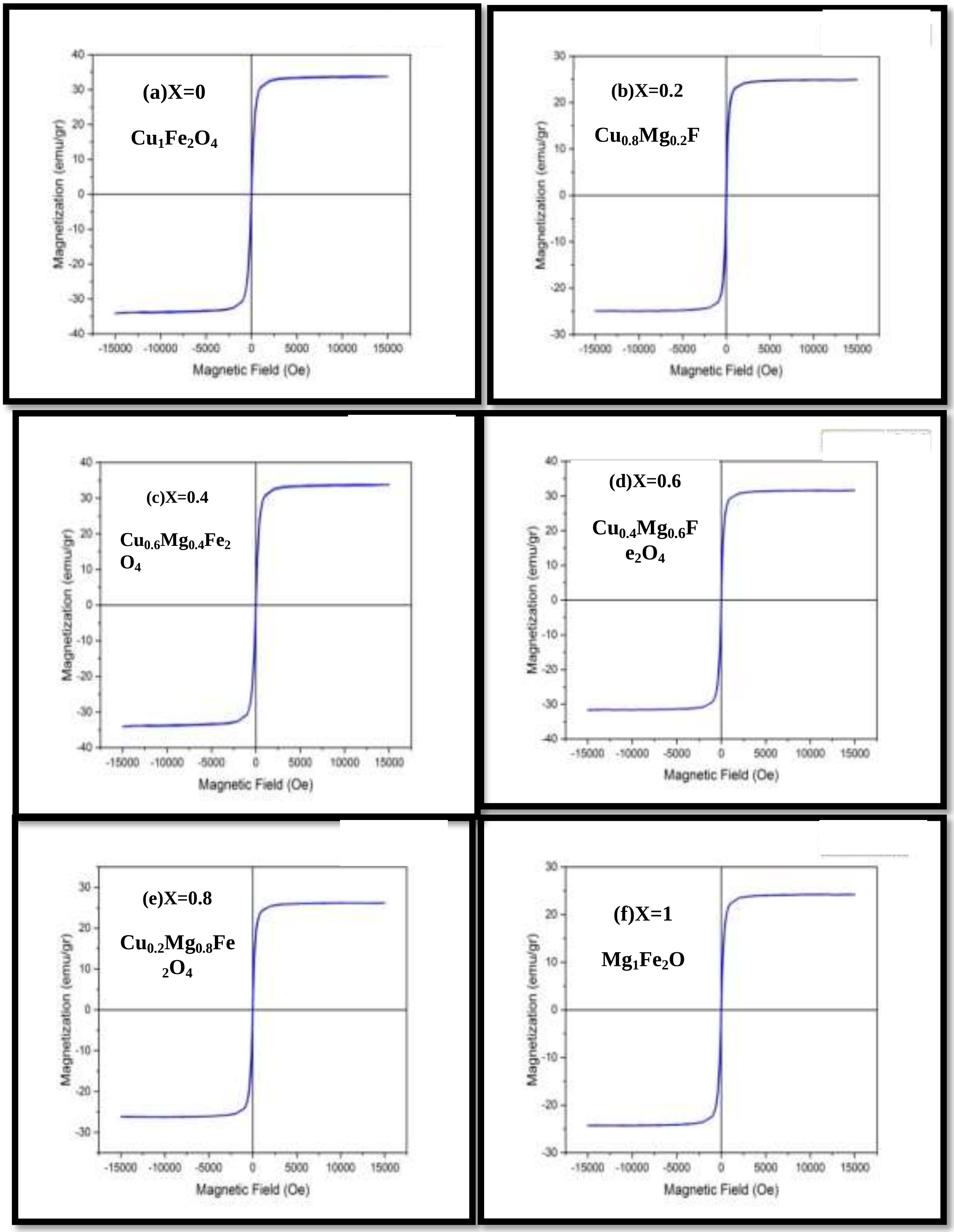

Figure (4.19): Magnetic hysteresis curves of $Cu_{1-x}Mg_x Fe_2O_4$ with a)x=0, b)x=0.2, c)x=0.4, d)x=0.6, e)x=0.8 and f)x=1 Mg after plasma exposure.

Table (4.8): Magnetic saturation(M_s), remaining magnetism(M_r) and force coercive(H_c) as a function of Manganese ratio after plasma exposure.

Ratio(x)	Component	M_s emu/g	M_r emu/g	H_c Oe
0	$CuFe_2O_4$	34.32	7.84	150
0.2	$Cu_{0.8}Mg_{0.2}Fe_2O_4$	25.45	1.64	51
0.4	$Cu_{0.6}Mg_{0.4}Fe_2O_4$	28.2	4.35	50
0.6	$Cu_{0.4}Mg_{0.6}Fe_2O_4$	27.4	1.96	25
0.8	$Cu_{0.2}Mg_{0.8}Fe_2O_4$	30.61	2.3	25
1	$MgFe_2O_4$	35.8	1.35	25

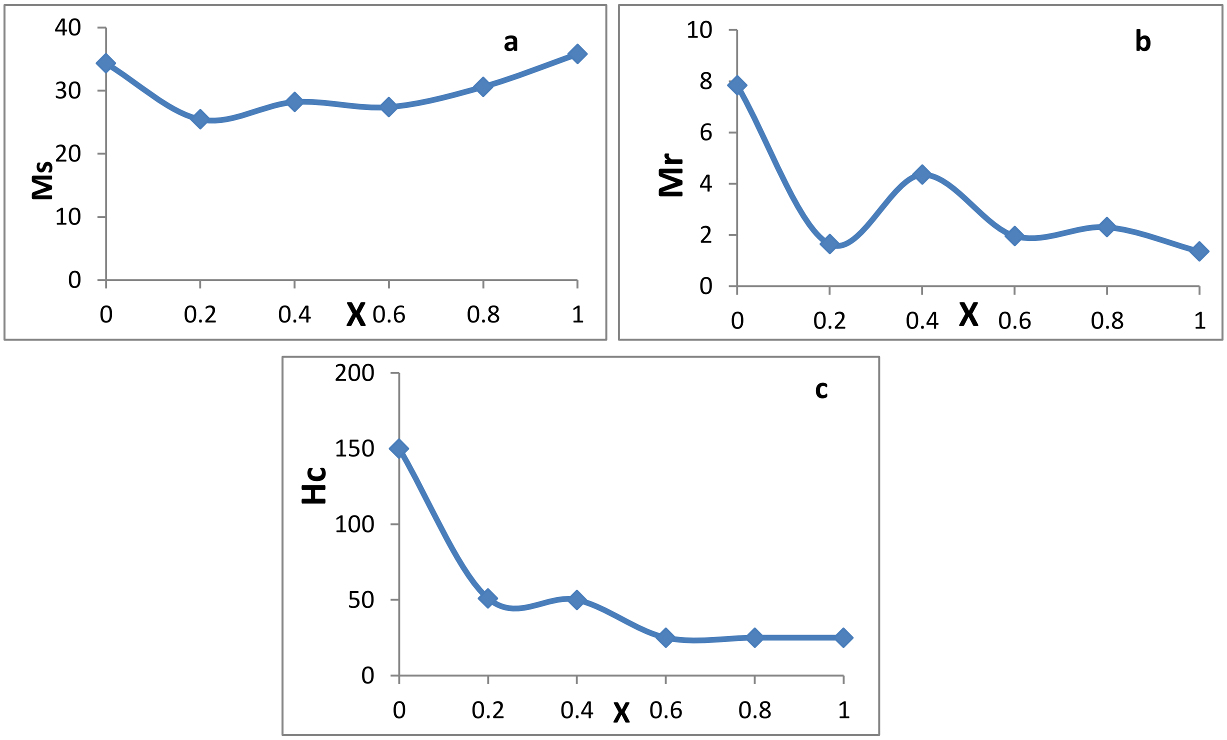

Figure (4.20): Shows the change of magnetic properties with all the ratios(x) after plasma exposure.

Chapter Five

Conclusions and Suggestions

5.1 Conclusions

1- The sol-gel process has advantages due to the ease of purification of liquids (being the starting material for the process), high purity materials are produced in prepare ferrites materials.

2- The tests conducted showed an increase in the crystal size of $Cd_{1-x}Mg_xFe_2O_4$ ferrite compound with increasing Mg concentration according to the ratios used. Also, a decrease in the crystal size of $Cu_{1-x}Mg_xFe_2O_4$ ferrite is observed with increasing Cu concentration.

3- Expose the prepared samples to plasma using the RF system using the target material CuO to the ferrite compound $Cd_{1-x}Mg_xFe_2O_4$. Tests showed that the size of the crystal decreases after exposure to plasma with an increase in the concentration of cadmium according to the proportions used, as for the ferrite compound $Cu_{1-x}Mg_xFe_2O_4$, the target material use ZnO is observe a decrease in the size of the crystal with the increase in the concentration of copper. Thus, X-ray measurements show that samples exposure to plasma have a cubic spinel structure and the variation of structural parameters with the exposure is irregular.

4- The FESEM results showed polymorphic particles within the nanoscale for all the prepared samples, the particles differed from each other in size and the FESEM microscopic images show that the grains have an irregular grain size distribution. The particle sharpness is more or less spherical, indicating crystallization which was also confirmed by the XRD pattern except at the higher concentration.

5- After exposure of the compound $Cd_{1-X}Mg_X\ Fe_2O_4$ to plasma, we conclusion a change in the topography of the surface, where the exposed surface on the plasma shows a change in the positions of the crystals and their coherence with each other. The ferrite $Cu_{1-x}Mg_x\ Fe_2O_4$ the crystal of copper ferrite is rather large. However, after exposure to plasma we notice a significant change in the shape and size of the crystal and it has become heterogeneous as it is no longer spherical.

6- FTIR measurements prior to exposure to the plasma demonstrate two strong absorption bands appearing in the infrared spectra of both samples. The FTIR spectrum of the sample the presence of two concentric absorption bands corresponding to the tetrahedral vibrations octahedral complexes, respectively (metal-oxygen-bonds). With plasma exposure of the two compounds both strips expands and also shows the survival of O-H and C–O.

7- VSM measurements included that soft ferritic materials have a small magnetic remaining loop. The compound $Cd_{1-x}Mg_xFe_2O_4$ before exposure to plasma had an increase in magnetic saturation magnetization with a increase in the magnesium ion, which was reflected in a decrease in the coercive force. We conclusion a continuous fluctuation in the saturated magnetization values, due to the size and shape of the particles. The decrease in coercivity is caused by the difference in crystal magnetism.

8- To the compound $Cd_{1-x}Mg_xFe_2O_4$ after plasma exposure. The change is also seen in saturation magnetization with an applied magnetic field where it is observed that the magnetization increases with an applied magnetic field where it is observed that the magnetization increases with the applied magnetic field, consistent with the normal behavior in which all loops confirm the soft magnetic of Cd-Mg ferro. An increase or fluctuation occurs in the value of the coercive force Hc.

9- The compound $Cu_{1-x}Mg_xFe_2O_4$ before exposure to plasma have fluctuation in magnetic saturation magnetization was observed, which affected the force coercive by increasing the ratio(x) due to the difference in crystalline magnetism.

10- It is clear to the compound $Cu_{1-x}Mg_xFe_2O_4$ that exposure to plasma actually led to an increase of M_s, M_r and H_c for the unexposed samples. This escalation due to higher tempreature surface the ferrite samples with the microwave plasma.

5.2 Suggestions

1-The possibility of studying the compounds that were prepared in this work, after exposing it to plasma and depositing it on quartz as a thin film, and studying its electrical, optical and magnetic properties, and the possibility of manufacturing a gas sensor.

2- For the same prepared compounds, the mechanical properties of the prepared ferrite can be studied, as well as the electrical properties, and the extent of its use in electrical appliances.

3- Preparation of new compounds in formulas, as follows, Mg1xZnxFe2O4, $Cd_{1-x}Zn_xFe_2O_4$, $Mg_{1-x}Cu_xFe_2O_4$, $Mg_xCd_{1-x}Fe_2O_4$, $Mg_xZn_{1-x}Fe_2O_4$. Also, exposure to plasma, study and comparison of properties before and after exposure.

4- Preparation of the same compounds with formulas $Cu_{1-x}Mg_xFe_2O_4$ or $Cd_{1-x}Mg_xFe_2O_4$ where M are cations (Co, Ni, Mg, Cu) with changing PH using co-precipitation or sol-gel method.

5- Study the effect of temperature on the dielectric and magnetic properties of the prepared samples.

6 - After preparing the nanocomposites, they can be exposed to the plasma using a homemade cold plasma jet system, which is a dielectric barrier discharge (DBD) type.

7- Preparation of ferrite by adding trivalent elements and studying the magnetic properties.

References

[1] Y. Miao, H. Zhu, P. Gao and L. Li, “The Effects of Spraying Power on Microstructure, Magnetic and Dielectric Properties of Plasma Sprayed Cobalt Ferrite Coatings”, Journal of Materials Research and Technology, Vol. 9, 2020.

[2] W. Fontijn, P. Zaag and L. Feiner, “ A Consistent Interpretation of the Magneto-Optical Spectra of Spinel Type Ferrites Invited”, Journal of Applied Physics, Vol. 85,1999.

[3] J. Massoudi, M. Smari, K. Nouri, E. Dhahri, K. Khirouni, S. Bertaina, L. Bessaisc and E. Hlilf, “Magnetic and Spectroscopic Properties of Ni–Zn–Al Ferrite Spinel: from the Nanoscale to Microscale”, The Royal Society of Chemistry, Vol. 10, 2020.

[4] G. Herzer, “Round Table Discussion: Present and Future Applications of Nanocrystalline Magnetic Materials”, Journal Magn. Mater., Vol. 294, 2005.

[5] M. Pardavi-Horvath, “Microwave Applications of Soft Ferrites”, Journal of Magnetism and Magnetic Materials, Vol. 215, pp. 171-183, 2000.

[6] K. Wiesemann, “A Short Introduction to Plasma Physics”, Scientific Information Service CERN, Vol.54, 2012.

[7] O. Tarvainen, T. Ropponen, V. Toivanen, J. Arje and H. Koivisto, “ Plasma Breakdown Diagnostics with the Biased Disc of Electron Cyclotron Resonance Ion Source”, Plasma Sources Science and Technology, Vol.9, 2009.

[8] P. Gao, V. Rebrov, M. Tiny, M. Verhoeven, J.Schouten, R. Kleismit, G. Kozlowski, J.Cetnar, Z. Turgut and G. Subramanyam, “Structural Investigations and Magnetic Properties of Sol-Gel $Ni_{0.5}Zn_{0.5}Fe_2O_4$ Thin Films for Microwave Heating”, Journal of Applied Physics ,Vol.107, 2010.

[9] D. Guo, Xi.Fan, G. Chai, C. Jiang, X. Lim and D. Xue, “Structural and Magnetic Properties of NiZn Ferrite Films with High Saturation Magnetization Deposited by Magnetron Sputtering”, Applied Surface Science,Vol.256, 2010.

[10] A. Nawale, N. Kanhe, K. Patil, S. Bhoraskar, V. Mathe and A. Das, “ Magnetic Properties of Thermal Plasma Synthesized Nanocrystalline Nickel Ferrite ($NiFe_2O_4$)”, Journal of Alloys and Compounds, Vol.509, 2011.

[11] Y. Liua, Y.Li, H. Zhang, D. Chen and C. Mu, “Structural and Magnetic Properties of NiZn–Ferrite Thin Films Prepared by Radio Frequency Magnetron Sputtering”, Journal of Applied Physics, Vol.109, 2011.

[12] I. Zalite, G. Heidemane, M. Kodols, J. Grabis and M. Maiorov, “The Synthesis, Characterization and Sintering of Nickel and Cobalt Ferrite Nanopowders”, Materials Science Medziagotyra, Vol.18, 2012.

[13] N. Sanpo, C.Berndt and J. Wangm, “Microstructural and Antibacterial Properties of Zinc-Substituted Cobalt Ferrite Nanopowders Synthesized by Sol-Gel Methods”, Journal of Applied Physics, Vol. 112, 2012.

[14] A. Druc, A. Borhan, G. Nedelcu, L. Leontie, A. Iordan and M. Palamaru, “Structure-Dielectric Properties Relationships in Copper Substituted Magnesium Ferrites”, Materials Research Bulletin, Vol.48, 2013.

[15] S. Kanagesan, M. Hashim, S. Tamilselvan, N. Alitheen, I. Ismail and G.

Bahmanrokh, “Cytotoxic Effect of Nanocrystalline $MgFe_2O_4$ Particles for Cancer Cure”, Journal of Nanomaterials,Vol.8, 2013.

[16] N. Najmoddin, A. Beitollahi, H. Kavas, S. Mohseni, H. Rezaie, J. Akerman and M.Toprak, “XRD Cation Distribution and Magnetic Properties of Mesoporous Zn-Substitute $CuFe_2O_4$”,Journal Ceramics International, Vol.40, 2014.

[17] K. Praveena, K. Sadhana and H. Virk, "Structural and Magnetic Properties of Mn-Zn Ferrites Synthesized by Microwave-Hydrothermal Process" , Solid State Phenom, Vol. 232, 2015.

[18] H. Le Trong, T. Bui, L. Presmanes, A. Barnabe, I. Pasquet, C. Bonningue and Tailhades,"Preparation of Iron Cobaltite Thin Films by RF Magnetron Sputtering", Thin Solid Films, Vol. 58,2015.

[19] H. Harzalia, F. Saidaa ,A. Marzoukia, A. Megrichea, F. Baillonb, F. Espitalierb and A. Mgaidia, "Structural and Magnetic Properties of Nano-Sized Ni Cu Zn Ferrites Synthesized by Co-precipitation Method with Ultrasound Irradiation", Journal of Magnetism and Magnetic Materials, Vol. 419, 2016.

[20] M. Reddy, R. Shakoor, A. Mohamed, M.Gupta and Q.Huang, "Effect of Sintering Temperature on the Structural and Magnetic Properties of $MgFe_2O_4$ Ceramics Prepared by Spark Plasma Sintering", Journal Ceramics International, Vol.42, 2016.

[21] A. Nawale, N. Kanhe, S. Rout, S. Bhoraskar, A. Das and V. Mathe, "Investigation of Structural Optical and Magnetic Properties of Thermal Plasma Synthesized Ni-Co Spinel Ferrite Nanoparticles", Ceramics International, Vol.43, 2017.

[22] L. Frolova and M. Derhachov, "The Effect of Contact Non-equilibrium Plasma on Structural and Magnetic Properties of $Mn_XFe_{3-X}O_4$ Spinels", Nanoscale Research Letters, 2017.

[23] L. Thorata, J. Patilb, D. Nadargib, U. Ghodakec, R. Kambaled and S. Suryavanshib, " Co^{+2} Substituted Mg–Cu–Zn Ferrite: Evaluation of Structural, Magnetic, and Electromagnetic Properties", Journal of Advanced Ceramics,Vol.7, 2018.

[24] J. Lin, Y. He, X. Du, Q. Lin, H. Yang and H. Shen, “Structural and Magnetic Studies of Cr^{+3} Substituted Nickel Ferrite Nanomaterials Prepared by Sol-Gel Auto-Combustion”, Journal Crystals, Vol. 8, 2018.

[25] S. Mallesh and V. Srinivas, “A Comprehensive Study on Thermal Stability and Magnetic Properties of MnZn-Ferrite Nanoparticles”, Magn. Magn. Mater, Vol. 475, 2019.

[26] A. Farheen and R. Singh, “Effect of Hydrothermal Annealing on Structure and Magnetic Properties of RF Sputtered Mn-Zn Ferrite Thin Films”, Materials Research Express, Vol. 6, 2019.

[27] F. Mulud, N.Dahham and I. Waheed, “Synthesis and Characterization of Copper Ferrite Nanoparticles”, Materials Science and Engineering,Vol.928, 2020.

[28] T. Hammad, S. Kuhn , A Abu Amsha , N.Hejazy and R. Hempelmann, “Comprehensive Study of the Impact of Mg^{+2} Doping on Optical, Structural, and Magnetic Properties of Copper Nanoferrites”, Journal of Superconductivity and Novel Magnetism, Vol. 33, 2020.

[29] J. Gil-Monsalve, M . Martinez-Puente, C. Ostos, J. Uribe, J .Osorio and O. Arnache, “Electronic Structure of Nickel Ferrite Thin Films Growth on Strontium Titanate”, Journal of Physics: Conference Series, Vol. 2046, 2021.

[30] M. Munir, M. Naz, S. Shukrullah, M. Ansar, M. Farooq, M. Irfan, S. Nasar, F.Mursal, S. Legutko, J. Petr and M. Paga,“ Enhancement of Magnetic and Dielectric Properties of $Ni_{0.25}Cu_{0.25}Zn_{0.50}Fe_2O_4$ Magnetic Nanoparticles through Non-Thermal Microwave Plasma Treatment for High-Frequency and Energy Storage Applications”, Journal of Materials, Vol. 15, 2022.

[31] A. Safari, Kh. Gheisari and M. Farbod, “The Effect of Plasma Arc Discharge Process Parameters on The Properties of Nanocrystalline (Ni, Fe)Fe_2O_4 Ferrite: Structural, Magnetic and Dielectric Studies”, Journal of Magnetism and Magnetic Materials, Vol. 451,2022.

[32] R. Kancharla and A.Vudayagiri, “Structural, Magnetic and Optical Properties $CoFe_2O_4$ Thin Films”, Journal of Superconductivity and Novel Magnetism,Vol.32, 2023.

[33] V. Gavrilov-Isaac, “Synthese de nanoparticules magnetiques energie d’anisotropie modulable”, Phd Thesis, University Pierre et Marie Curie - Paris VI, 2015.

[34] J. Massoudi, M. Smari, K. Nouri, E. Dhahri, K. Khirouni, S. Bertaina, L. Bessaisc and E. Hlilf, “Magnetic and Spectroscopic Properties of Ni-Zn-Al Ferrite Spinel: from the Nanoscale to Microscale”, The Royal Society of Chemistry, Vol. 10, 2020.

[35] C. Sujatha, K. Reddy, K. Babu, A. Reddy, and K. Rao, “Structural and Magnetic Properties of Mg Substituted Ni Cu Zn Nano Ferrites”, Phys. B Condens. Matter, Vol. 407, 2012.

[36] I. Petrov, M. Niemela,P. Ponomarev and J. Pyrhönen,“Rotor Surface Ferrite Permanent Magnets in Electrical Machines Advantages and Limitations”, Transactions on Industrial Electronics, Vol.64, 2017.

[37] S. Mohammed, A. Ridha and G. Khalaf Salman, “Synthesis and Characterization of Magnesium Ferrites Material”, M.Sc. Thesis, Department of Applied Sciences, University of Technology,Vol.32, 2012.

[38] A. Goldman, "Modem Ferrite Technology", Springer New York, 2006.

[39]M. Abdulmajeed, “Dielectric Behavior of Nickel-Zinc Dopped Hexagonal W-type Barium Ferrite”, Journal of Al-Nahrain University Vol.15, 2012.

[40] R. Buchanan, “Ceramic Materials for Electronics”, CRC Press Taylor and Francis Group, 2018.

[41] B. Cullity and C. Graham, “Introduction to Magnetic Materials”, Jon Wily , Hoboken, New Jersey, 2009,

[42] R. Sridhar, D. Ravinder and K. Kumar, “Synthesis and Characterization of Copper Substituted Nickel Nano-Ferrites by Citrate-Gel Technique”, Advances in Materials Physics and Chemistry, Vol.2, 2012.

[43] R. Valenzuela, “Novel Applications of Ferrites”, Physics Research

International, 2012.

[44] R. Hilzinger and W. Rodewald, “ Magnetic Materials: Fundamentals, Products, Properties, Applications”, Vacuumschmelze, Hanau, 2013.

[45] C. Liu, Q. Xu, Yu Tang, Z. Wang, R. Ma, N. Maa and P. Du “Zr^{+4} Doping-Controlled Permittivity and Permeability of $Bafe_{12-X}ZrxO_{19}$ and the Extraordinary EM Absorption Power in the Millimeter Wavelength Frequency Range”, Journal of Materials Chemistry,Vol.40, 2016.

[46] J. Sharma, P. Srivastava, G. Singh and H. Virk, “Nanoferrites of Transition Metals and Their Catalytic Activity”, Solid State Phenomena,Vol.241, 2016.

[47] S. Daliya and R. Juang, “An Overview of the Structure and Magnetism of Spinel Ferrite Nanoparticles and Their Synthesis in Microemulsions”, Journal Chemical Engineering, Vol. 129 ,2007.

[48] M. Neel, “Proprietes Magnetiques Des Ferrites; Ferrimagnetisme Et Antiferromagnetisme,” Ann. Phys. (Paris), Vol. 12. 1994.

[49] A. Arora, “Optical and Electric Field Control of Magnetism”, Ph.D. College of Mathematics and Natural Sciences from the University of Potsdam, 2018.

[50] S. Blundell and D. Thouless, “ Magnetism in Condensed Matter”, Am. J. Phys., Vol. 71, 2003.

[51] R. Geyer, “Ferrite Ceramics at Microwave Frequencies”, National Institute of Standard and Technology, 2001.

[52] Jackson and Roland, “John Tyndall and the Early History of Diamagnetism”, Annals of Science, Vol.72, 2014.

[53] H. Sulaiman Mahmood, “Preparation of Nano Barium Ferrite and Measurement of Its Electrical Properties at (X-Band) Region Using Waveguide”, M.Sc Thesis, University of Diyala, 2016.

[54] M. Vijaya, G. Rangarajan, “ Materials Science”, McGraw-Hill Publishing Company Limited, Vol. 447, 2000.

[55] S. Chikazumi and C. Graham, “Physics of Ferromagnetism”, International Series of Monographs on Physics, 2009.

[56] N. Spaldin ,“Magnetic Materials Fundamentals and Applications”, Hardback University of California, 2011.

[57] Y. Zhu, “Modern Techniques for Characterizing Magnetic Materials”, Springer Science, 2005.

[58] C. Gonano, R. Zich, and M. Mussetta, “Definition for Polarization P and Magnetization M Fully Consistent with Maxwell’s Equations”, Progress In Electromagnetics Research, Vol. 64, 2015.

[59] M. Karkare and R.Bahuguna, “Applied Physics”, Nanotechnology: Fundamentals and Applications and Applied Physics, Vol.1,2007.

[60]M. Al Janaideh, S. Rakheja and Chun-Yi Su, “An Analytical Generalized Prandtl–Ishlinskii Model Inversion for Hysteresis Compensation in Micropositioning Control”, IEEE/ASME Transactions on Mechatronics, Vol.16, 2010.

[61] F. Abed Yasseen Hussein AL-Kufy, “Characterization of Nano Spinel Ferrite Fields”, Ph.D.Thesis, University of Babylon.2020.

[62] S. Prasad, N. Gajbhiye and J. Alloys,“ Magnetic Studies of Nanosized Nickel Ferrite Particles Synthesized by the Citrate Precursor Technique”, Vol. 265 ,1998.

[63] P. Dolcet, K. Kirchberg, A. Antonello, C.Suchomski, R. Marschall, S. Diodati, R. Munoz-Espí, K. Landfester and S. Gross,“ Exploring Wet Chemistry Approaches to $ZnFe_2O_4$ Spinel Ferrite Nanoparticles with Different Inversion Degrees: A Comparative Study,” Inorganic Chemistry Frontiers, Vol. 6, 2019.

[64] M. Huq, D. Saha, R. Ahmed and Z. Mahmood, “Ni-Cu-Zn Ferrite Research: a Brief Review,” Journal of Scientific Research.,Vol.5 2013.

[65] N. Jahan, F. Chowdhury and A. Zakaria, “Structural and Electrical Properties of Chromium Substitutednickel Ferrite by Conventional Ceramic Method”, Materials Science-Poland, Vol.34, 2016.

[66] J. Park and E.Matijevic, “Model of Formation of Monodispersed Colloids” , Journal of Physical Chemistry, Vol. 105,2001.

[67] S. Dembski, C. Schneider, B. Christ and M. Retter, “Core-shell Nanoparticles and their Use for in Vitro and in Vivo Diagnostics”, Publishing Series in Biomaterials,2018.

[68] G. Huang, Huang-Hao Yang and Chun-Hua, “Novel Nanomaterials for Biomedical, Environmental and Energy Applications”, Micro and Nano Technologies, 2019.

[69] B. Kafle, “Chemical Analysis and Material Characterization by Spectrophotometry”, Chemical Analysis and Material Characterization by Spectrophotometry, 2020.

[70] S. Hasany, I. Ahmed, J .Rajan and A. Rehman, “Systematic Review of the Preparation Techniques of Iron Oxide Magnetic Nanoparticles”, Scientific and Acsdemic Publishing , Vol.2, 2011.

[71] A. Tavakoli, M. Sohrabi and A. Kargari, “A Review of Methods for Synthesis of Nanostructured Metals with Emphasis on Iron Compounds”, Journal Chemical Papers, Vol.61, 2007.

[72] U. Lam, R. Mammucari, K. Suzuki, N. Foster, “Processing of Iron Oxide Nanoparticles by Supercritical Fluids”, American Chemical Society, Vol. 47, 2008.

[73] Y. Natsume and H. Sakata, “Zinc Oxide Films Prepared by Sol-gel Spin-Coating”, Thin Solid Films, Vol. 372, 2000.

[74] R. Corriu and N. Trong Anh, “Molecular Chemistry of Sol-gel Derived Nanomaterials” , A Jon Wiely and Sons, France, 2009.

[75] S. Rahman, W. Agami and M. Eltabey, “Frequency, Temperature and Composition Dependence of Dielectric Properties of Nd^{+3} Substituted Cu-Zn Ferrites” , Life Science Journal, Vol. 9, 2012.

[76] E. Camponeschi, J.Walker, H. Garmestani, and Rina Tannenbaum, "Surfactant Effects on the Particle Size and Formation of Iron Oxides via a Sol-Gel Process ", ACS Symposium Series, Vol. 996, 2008.

[77] R. Gould and W. Massa, " Crystal Structure Determination", Springer Berlin Heidelberg, 2013.

[78] R. Neutze, R. Wouts, D. van der Spoel, E. Weckert and J. Hajdu, "Potential for Biomolecular Imaging with Femtosecond X-Ray Pulses", journal (Refereed)of Uppsala University Publications, Swede, Vol.406, 2000.

[79] S. Mondal, K. Kanta, and P. Mitra, "Preparation of Al-doped ZnO (AZO) Thin Film by SILAR," Journal Physics Science, Vol. 12, 2008.

[80] A. Monshi, M. Foroughi, and M. Reza Monshi , "Modified Scherrer Equation to Estimate More Accurately Nano-Crystallite Size Using XRD", World Journal of Nano Science and Engineering, Vol. 2, 2012.

[81] S. Sharma, H.Rasool, V. Palanisamy, C. Mathisen, M. Schmidt, D. Wong, and J.Gimzewsk, "Structural-Mechanical Characterization of Nanoparticle Exosomes in Human Saliva, Using Correlative AFM, FESEM and Force Spectroscopy", Coastal and Estuarine Processes, Vol.4, 2009.

[82] D. Bokov , A. Turki Jalil, S. Chupradit , W. Suksatan, M. Ansari, Iman Shewael, G. Valiev and E. Kianfar, "Nanomaterial by Sol-Gel Method: Synthesis and Application", Advances in Materials Science and Engineering, Vol.22, 2021.

[83] R. Aparna, V. Brahmajirao, V. Kartikeyan and M. Fernandes, "Synthesis and Structural, Morphological and FTIR Studies on Ferrite Powders $BaFe_{12-X}Ti_XO_{19}$, Using Sol-Gel Methods", Journal of Applied Physics, Vol. 8 , 2016.

[84] V. Lopez, A. Quesada, J. Guzman, L. Moreno, M. Lere, J. Spottorno, F. Giacomone , J. Fernandez, A. Hernando and M. Garcia, “A simple Vibrating Sample Magnetometer for Macroscopic Samples”, Review of Scientific Instruments, Vol. 89, 2018.

[85] A. Piel, “Plasma Physics an Introduction to Laboratory, Space and Fusion Plasmas”, Springer Heidelberg Dordrecht London New York, 2010.

[86] P. Chu and X. Lu, “Low Temperature Plasma Technology : Methods and Applications”, CRC Press, Taylor and Francis group, 2013 .

[87] A. Barkan, D. Angelo and Merlino, “Experiments on Ion Acoustic Waves in Dusty Plasmas”, Planetary and Space Science, Vol.44, 1996.

[88] F. Francis, “Introduction to Plasma Physics and Controlled Fusion Second Edition”, Springer Science Business Media, Vol. 1,1984.

[89] F. Francis Chen, “Introduction to Plasma Physics and Controlled Fusion”, Springer ,Plenum Press New York, 2016.

[90] V. Nehra, A. Kumar and H. Dwivedi, “Atmospheric Non-Thermal Plasma Sources”, International Journal of Engineering, Vol.2, 2008.

[91] K .Chaudhary, A. Imam, S. Rizvi and J .Ali, “Plasma Kinetic Theory in Kinetic Theory”, In Tech Rijeka Croatia, 2018.

[92] J. Freddy Hansen and M. Paul Bellan, “Experimental Demonstration of How Strapping Fields Can Inhibit Solar Prominence Eruptions”, The Astrophysical Journal, Vol. 563, 2001.

[93] T. Hikari , S. Masahiro and K.Hironori, "Quantification of lithium in LIB electrodes with glow discharge optical emission spectroscopy (GD-OES)", Journal of Power Sources, Vol. 244,2013.

[94] L. Quiros and E. dbertho, “Plasma Processing of Municipal Solid Waste”, Brazilian Journal of Physics,Vol.34, 2004.

[95] I. Hutchinson, “Principles of Plasma Diagnostics: Second Edition”, Plasma Physics and Controlled Fusion, IOPscience,Vol.44, 2002.

[96] W. Carthy, T. Golfinopoulos, K. Woller, C. Vincent, A. Kuang and B. Labombard, “First Application of a Digital Mirror Langmuir Probe for Real-Time Plasma Diagnosis”, AIP Publishing, USA,Vol.92, 2021.

[97] N. Zhang, F. Sun, L. Zhu, M. Planche, H. Liao, C. Dong and C. Coddet, “Electron Temperature and Density of the Plasma Measured by Optical Emission Spectroscopy VLPPS Conditions”, Journal of Thermal Spray Technology, Vol. 20, 2011.

[98] J. Adamek, J. Stockel, M. Hron, J. Ryszawy, M. Tichy, R. Schrittwieser, C. Ionita, P. Balan and E. Martines,“A Novel Approach to Direct Measurement of the Plasma Potential”, Czechoslovak Journal of Physics, Vol.54, 2004.

[99] W. Rehak, “Plasma Diagnostics in RF Discharges Using Nonlinear and Resonance Effects”, Journal of Applied Physics, Vol.36,1997.

[100] E. Everson, P. Pribyl, C. Constantin, A. Zylstra, D. Schaeffer, N. Kugland and C. Niemann, “Design, Construction, and Calibration of a Three-Axis, High-Frequency Magnetic Probe (B-Dot Probe) as a Diagnostic for Exploding Plasmas”, Review of Scientific Instruments, Vol. 80, 2009.

[101] A. Vimont, F.Thibault-Starzyka and M. Daturi, “Analysing and Understanding the Active Site by IR Spectroscopy”, Chemical Society Reviews,Vol.12, 2010.

[102] Z. Donko, P. Hartmann and K. Kutasi, “ On the Reliability of Low-Pressure Dc Glow Discharge Modelling”, Plasma Sources Science and Technology, IOPscience, Vol. 15, 2006.

[103] J. Chae, S. Moon, H. Sun, K. Kim, V. Vassiliev and E.Mikholap, “A Study of Volatile Organic Compounds Decomposition with the Use of Non-Thermal Plasma”, KSME International Journal, Vol. 13.1999.

[104] P. Glover and R. Bowtel,“ Measurement of Electric Fields Due to Time-Varying Magnetic Field Gradients Using Dipole Probes”, Physics in Medicine and Biology,Vol.52,2007.

[105] J .Roth, “Industrial Plasma Engineering”, Taylor and Francis Books, Vol. 56, 2019.

[106] P. Chabert and N. Braithwaite, “Physics of Radio-Frequency Plasmas”, United States of America by Cambridge University Press, New York, 2011.

[107] R. Behrisch and W. Eckstein, “Sputtering by Particle Bombardment: Experiments and Computer Calculations from Threshold to Mev Energies”, Springer Berlin, Heidelberg, 2007.

[108] E. Alfonso, J. Olaya and G. Cubillos, “Thin Film Growth Through Sputtering Technique and its Applications”, Crystallization-Science and Technology, 2012.

[109] G .Vinogradov, “Transmission Line Balanced Inductive Plasma Sources”, Plasma Sources Science and Technology ,Vol.9, 2000.

[110] H. Uno, N. Hikuma, T. Omata, N. Ueda, T. Hashimoto and H. Kawazoe, “Preparation of $MgIn_2O_{4-}X$ Thin Films on Glass Substrate by RF Sputtering”, Japanese Journal of Applied Physics, Vol.32,1993.

[111]V. Pierrard and N. Meyer-Vernet, “Electron Distributions in Space Plasmas”, Kappa Distributions, 2017.

[112]_E. Hnatiuc, D. Astanei, M. Ursach and B. Hnautiuc, “A Review Over Cold Plasma Reactors and Their Applications”, ICEPE, 2012.

[113] Yu. Lebedev, “Microwave Discharges: Fundamentals and Application”, Russian Academy of Sciences, 2000.

[114] J .Roth, “Industrial Plasma Engineering”, Institute of Physics Publishing London, Vol.1,2000.

[115] A. Shashurin, M. Keidar, S. Bronnikov, R. Jurjus and M. Stepp, “Living tissue under treatment of cold plasma atmospheric jet”, AIP Publishing, Vol.93, 2008.

[116] L. Rubin and J. Poate, “Ion Implantation in Silicon Technology”, Industrial Physicist, Vol. 9, 2003.

[117] L. Ozhigov, V. Belous, V. Savchenko, G. Nosov, V. Ovcharenko, G. Tolmachova, A. Kuprin and V. Goltvyanitsa,“ Role of Surface Layer Nanosrtucturing in Improving Mechanical and Corrosion Properties of Reactor Materials”, Physics of Radiotechnology and Ion-Plasma Technolo-gies, 2017.

[118] S. Rosanvallon, C. Grisolia, G. Counsell, S. Hong, Onofri, J. Worms, J. Winter, B. Annaratone, G. Maddaluno, and P. Gasior, “Dust Control in Tokamak Environment”, Fusion Engineering and Design,Vol.83, 2008.

[119] D. Blaj, R. Rotaru and C. Peptu, “16 - Protective Textiles from Natural Resources for Electromagnetic Shielding”, Protective Textiles from Natural Resources, The Textile Institute Book Series, 2022.

[120] S. Yener and O. Cerezci, “Material Analysis and Application for Radio Frequency Electromagnetic Wave Shielding”, Acta Physica Polonica, Vol. 129, 2016.

[121] M. Gupta, M. Gupta, R. Anu, K. Mudsainiyan and B. Randhawa, “Aqueous Ammonia as “CPCA” in Sol-gel Combustion Method for Nanofabrication of $CdFe_2O_4$”, Materials Today Proceeding, Vol. 3, 2016.

[122] C. Murugesan and G. Chandrasekaran, “Structural and Magnetic Properties of $Mn_{1-x}Zn_xFe_2O_4$ Ferrite Nanoparticles”, Journal of Superconductivity and Novel Magnetism., Vol. 29, 2016.

[123] J. Ma, B. Chen, B. Chen and S. Zhang, “Preparation of Superparamagnetic $ZnFe_2O_4$ Submicrospheres Via a Solvo thermal Method”, Advances in Nano Research, Vol. 5, 2017.

[124] S. Nie, H. Geng, J. Wang, L. Wang, Z. Wang, R. Xu, G. Yue, Y. Chen and D. Peng,” The Structure and Magnetic Properties of NiZn-Ferrite Films Deposited by Magnetron Sputtering at Room Temperature “,Advanced Materials Research, Vol. 690, 2013.

[125] X. Zuo, A. Yang, C. Vittoria and V. Harris, “Computational Study of Copper Ferrite ($CuFe_2O_4$)”, Journal of Applied Physics, Vol.99, 2006.

[126] S. Assar, H. Abosheiasha and A. El-Sayed, “Effect of Γ-Rays Irradiation on the Structural, Magnetic, and Electrical Properties of Mg–Cu–Zn and Ni–Cu–Zn Ferrites”, Journal of Magnetism and Magnetic Materials, Vol. 421, 2017.

[127] M. Desai, S. Prasada, N. Venkataramani, I. Samajdar and A. Nigam, “Annealing Induced Structural Change in Sputter Deposited Copper Ferrite Thin Films and its Impact on Magnetic Properties”, Journal of Applied Physics, Vol.91, 2002.

[128] A. Soufi, H. Hajjaoui, R. Elmoubarki, M. Abdennouri and N. Barka ,“Sol-gel auto-Combustion Synthesis of $Cu_{1-X}Mg_xFe_2O_4$ Nanoparticles and their Heterogenous Fenton-Like Activity Towards Tartrazine”, Inorganic Chemistry Communications, Vol.142, 2022,

[129] S. Singhala, T. Namgyala, N. Laxhmib and S. Bansal, “Doping Assisted Structural Transition in Copper Substituted $MgFe_2O_4$ Ferrite: Thermal, Electrical and Magnetic Properties”, Scientia Iranica , Vol.20, 2013.

[130] M. Desai, J. Dash, I. Samajdar, N. Venkataramani, S. Prasad, P. Kishan and N. Kumar, “A TEM Study on Lithium Zinc Ferrite Thin Films and the Microstructure Correlation with the Magnetic Properties”, Journal of Magnetism and Magnetic Materials, Vol. 231, 2001.

[131] J. Mohapatra, M. Xing, J. Elkins, J. Beatty and P. Liu, “ Size-Dependent Magnetic Hardening in $CoFe_2O_4$ Nanoparticles: Effects of Surface Spin Canting”, Journal of Physics D: Applied Physics, Vol. 53, 2020.